STUDIES ON PULSE SHAPE DISCRIMINATION AND EFFICIENCY OF GGAG:Ce SCINTILLATORS

Ph.D. THESIS

by

SHEETAL RAWAT

DEPARTMENT OF PHYSICS
INDIAN INSTITUTE OF TECHNOLOGY ROORKEE
ROORKEE – 247667 (INDIA)
JUNE, 2019

STUDIES ON PULSE SHAPE DISCRIMINATION AND EFFICIENCY OF GGAG:Ce SCINTILLATORS

A THESIS

Submitted in partial fulfilment of the requirements for the award of the degree

of

DOCTOR OF PHILOSOPHY

in

PHYSICS

by

SHEETAL RAWAT

DEPARTMENT OF PHYSICS
INDIAN INSTITUTE OF TECHNOLOGY ROORKEE
ROORKEE–247667 (INDIA)
JUNE, 2019

INDIAN INSTITUTE OF TECHNOLOGY ROORKEE
ROORKEE

CANDIDATE'S DECLARATION

I hereby certify that the work which is being presented in this thesis entitled, **"STUDIES ON PULSE SHAPE DISCRIMINATION AND EFFICIENCY OF GGAG:Ce SCINTILLATORS"** in partial fulfilment of the requirements for the award of the Degree of **Doctor of Philosophy** and submitted in the Department of Physics of the Indian Institute of Technology Roorkee, Roorkee is an authentic record of my own work carried out during a period from August, 2014 to June, 2019 under the supervision of Dr. Anil K. Gourishetty, Associate Professor, Department of Physics, Indian Institute of Technology Roorkee, Roorkee and Prof. S. C. Gadkari, Bhabha Atomic Research Center, Mumbai.

The matter presented in this thesis has not been submitted by me for the award of any other degree of this or any other Institute.

(SHEETAL RAWAT)
Signature of Candidate

This is to certify that the above statement made by the candidate is correct to the best of our knowledge.

(Anil K. Gourishetty)
Signature of Supervisor

(**S. C. Gadkari**)
Signature of Supervisor

The Ph.D. Viva-Voce Examination of Ms. Sheetal Rawat, Research Scholar, has been held on . . . . . at the Department of Physics, IIT Roorkee, Roorkee, INDIA.

Chairman, SRC

Signature of External Examiner

This is to certify that the student has made all the corrections in the thesis.

Signature of Supervisors
Dated: . . . . . .

Head of the Department

ABSTRACT

Among garnet based scintillators, Ce doped GGAG:Ce (Gadolinium Gallium Aluminium Garnet) scintillator proved to be a promising candidate for charged particle detection due to its high light yield and fast decay time combined with its non-hygroscopic nature. In the present thesis work, extensive studies were made on the pulse shape discrimination (PSD) properties of GGAG:Ce single crystals and on improving its PSD ability with co-doping and with phoswich combination. Owing to its high effective Z (55) and high density (6.7 g/cm^3), the present work also highlights GGAG:Ce as a strong contender for gamma spectroscopy where detection efficiency is of paramount importance.

The work starts with making a comparison of PSD abilities of GGAG:Ce,B and CsI:Tl scintillator coupled to PMT and SiPM. The studies were made employing digital charge integration and analog zero-crossing technique. The studies have shown that GGAG:Ce,B coupled to a PMT and CsI:Tl coupled to SiPM have shown better PSD abilities. For the first time, the opposite behavior of scintillation decay times corresponding to alpha and gamma radiations for GGAG:Ce and CsI:Tl scintillators has been reported.

The detailed realistic Monte Carlo simulations of absolute efficiencies (both total detection and photo-peak) for gamma rays up to energy of 5 MeV and for different values of source-to-detector separation have clearly suggested that the efficiency of GGAG:Ce scintillator is highest in comparison with $LaBr_3$:Ce, NaI:Tl, CsI:Tl, BaF_2 and SrI_2:Eu. The simulations have shown that the percentage difference in TDE of GGAG:Ce and NaI:Tl for 662 keV is 40%. Whereas, the percentage difference in PE of GGAG:Ce and NaI:Tl for 662 keV is 61%. The simulations wer4 validated by making experimental measurements. Simulated and measured efficiency values of GGAG:Ce scintillator having dimensions 18 mm × 18 mm × 10 mm and 25.4 mm ×10 mm for different values of source-to-detector separation are in good agreement.

A study on the effect of co-dopants on the scintillation properties of GGAG:Ce single crystals by investigating their PSD abilities is carried out. B co-doped crystals exhibited the highest PSD while those with Ca co-doping showed no discrimination in spite of having significant effect on the scintillation kinetics and a strong quenching of the light yield by alpha radiations that resulted in a minimum α/γ ratio. A new approach of optically stimulated luminescence (OSL) is used to correlate PSD

properties with the defect structure of GGAG:Ce single crystal. OSL studies with infrared, blue and green light provided an insight into the role of defect centers in the relaxation mechanism of the scintillation kinetics of GGAG:Ce crystals which subsequently affects their ability of discriminating different kinds of radiation.

A novel design of phoswich detector is proposed for the discrimination of various types of nuclear radiation such as protons, heavy ions, neutrons and gamma rays. Its novelty lies in the use of two non-hygroscopic scintillators having similar light yield, peak emission wavelength and refractive index. Due to their different scintillation decay times and opposite behavior for alpha and gamma radiations, an increment of 100% in FOM is found compared to that observed for any other individual crystal.

LIST OF PUBLICATIONS

Publications in Refereed Journal

1. Pulse shape discrimination properties of $Gd_3Ga_3Al_2O_{12}$:Ce single crystal in comparison with CsI:Tl, **S. Rawat,** Mohit Tyagi, P. K. Netrakanti, V. K. S. Kashyap, A. Mitra, A. K. Singh, D. G. Desai, G. Anil Kumar, S. C. Gadkari, *Nuclr. Instrum. Meth. Phys. Res. A* **840** (2016) 186-191.
2. Efficiency studies on $Gd_3Ga_3Al_2O_{12}$:Ce scintillators: Simulations and measurements, **S. Rawat,** M. Tyagi, G. Anil Kumar and S. C. Gadkari, *IEEE Trans. on Nucl. Sci.,* 65 (August 2018) 2109-2113.
3. Studies on effect of co-doping on PSD properties of, **S. Rawat,** M. Tyagi, G. Anil Kumar, S. C. Gadkari and Hong Joo Kim, *IEEE Trans. on Nucl. Sci.,* 2019 [Revised manuscript under review].
4. A novel versatile phoswich detector consisting of two single crystals to discriminate various kinds of radiation, M. Tyagi, **S. Rawat,** G. Anil Kumar and S. C. Gadkari, *Rev. Sci. Instrum.,* 2019 [Revised manuscript under review].

Apart from my thesis work

5. Intrinsic resolution of Compton electrons in $CeBr_3$ scintillator using compact CCT, V. Ranga, **S. Rawat,** Snigdha Sharma, Mukesh Prasad, S. Panwar, Kalyani, M. Dhibar, G. Anil Kumar, *IEEE Trans. on Nucl. Sci.,* 65 (January 2018) 616-620.

Papers presented in Conferences

1. Timing measurements with $LaCl_3$(0.9%Ce) detectors and their application in the measurement of speed of light, **S. Rawat,** A. Kamboj and G. Anil Kumar, *DAE Symposium on Nuclear Physics (Govt. of India)* **60** (2015) 1056-1057.
2. Activity Measurements of Co-60 Using Modified Sum-peak Method, **S. Rawat,** M. Dhibar and G. Anil Kumar, *20th National Seminar on Crystal Growth and Applications, BARC*, Mumbai, (2016) 274-275.
3. Pulse shape discrimination in Boron codoped $Gd_3Ga_3Al_2O_{12}$ (Ce) and CsI(Tl):A comparative study, **S. Rawat,** Mohit Tyagi, V. K. S. Kashyap, P. K. Netrakanti, A. K. Singh, D. G. Desai, A. Mitra**,** G. Anil Kumar**,** S. Sen, S. C. Gadkari, *DAE Symposium on Nuclear Physics (Govt. of India)* **61** (2016) 1064.

4. Intrinsic resolution of Compton electrons in $LaBr_3$:Ce and $LaCl_3$:Ce detectors using Compton Coincidence Technique, Snigdha Sharma,V. Ranga, M. Dhibar, **S. Rawat**, G. Anil Kumar, *Proceedings of DAE Symposium on Nuclear Physics (Govt. of India)* **61** (2016) 1020.
5. Efficiency studies on $Gd_3Ga_3Al_2O_{12}$(Ce) scintillators: Simulations and measurements, **S. Rawat,** M. Tyagi, G. Anil Kumar and S. C. Gadkari, *SCINT 2017 14th Int. Conference on Scintillating Materials and their Applications*.
6. Effect of codoping on pulse shape discrimination properties of $Gd_3Ga_3Al_2O_{12}$(Ce) scintillators, M. Tyagi, **S. Rawat,** G. Anil Kumar and S. C. Gadkari, *SCINT 2017 14th Int. Conference on Scintillating Materials and their Applications*.
7. A new phoswich design of CsI:Tl /GGAG:Ce,B scintillators for pulse shape discrimination, **S. Rawat,** M. Tyagi, G. Anil Kumar and S. C. Gadkari, *DAE Symposium on Nuclear Physics (Govt. of India)* **62** (2017) 1106.
8. Pulse shape discrimination properties of boron co-doped GGAG:Ce scintillator for charged particles and gamma rays, **S. Rawat,** Mohit Tyagi, Y. K. Gupta, D. C. Biswas, G. K. Prajapati, R. P. Vind, R. V. Jangale, B. V. John, G. Anil Kumar, S. C. Gadkari, *DAE Symposium on Nuclear Physics (Govt. of India)* **61** (2017) 1110.
9. Growth and Characterization of Large size $Gd_3Ga_3Al_2O_{12}$:Ce,B Single Crystal for High Energy Radiation Detection, Mohit Tyagi, D. G. Desai, **S. Rawat**, A. K. Singh, M. Sonawane, P. S. Sarkar and S. C. Gadkari, DAE SSPS, **H-123** (2017).
10. Growth and scintillation properties of Tl doped LiI single crystal: A fast thermal neutron scintillator, Kalyani, **S. Rawat,** Awadh K. Singh, G. Anil Kumar, Mohit Tyagi, *DAE International Symposium on Nuclear Physics (Govt. of India)* **63** (2018) 1132.
11. An improvement of the pulse shape discrimination properties of $Gd_3Ga_3Al_2O_{12}$:Ce single crystal scintillator, **S. Rawat,** Mohit Tyagi, G. Anil Kumar, *DAE International Symposium on Nuclear Physics (Govt. of India)* **63** (2018) 1130.

ACKNOWLEDGEMENTS

Feeling gratitude and not expressing it is like wrapping a present and not giving it.

- *William Arthur Ward*

Firstly, I would like to express my sincere gratitude to my supervisor Dr. Anil K. Gourishetty for the continuous support during my Ph.D, for his patience, motivation, encouragement, and immense knowledge. His guidance helped me in all the time of research and writing of this thesis. I could not have imagined having a better advisor and mentor for my Ph.D. I am also extremely thankful to my co-guide S. C. Gadkari for giving me an opportunity to experience, learn and work at BARC. I have spent almost two years at BARC and carried out most of my experiments there. This would not have been possible without the support, critical advice and encouragement of Dr. Mohit Tyagi. I owe all of my technical and research training knowledge along with the publications during my PhD to his brilliant supervising skills. He taught me how to analyse and work through a problem which is the best skill to learn during a PhD program according to me. I wish to thank everyone at CTL especially Dr. Seema Shinde, Dr. A. K. Singh, Dr. Sashwati Sen, Dr. G. D. Patra, Dr. S. G. Singh, D. G. Desai, Manoranjan sir, Shreyas sir, Sarkar sir and scientific assistants present in the lab or at BARC for teaching and helping me out in some or the other form.

Now coming to IIT Roorkee, I would like to acknowledge my thesis committee: Prof. R. Srivastava, Dr. R. K. Dutta, Dr. Ajay Y. Deo, Prof. D. Kaur for their positive and constructive advices. I thank Prof. K. L. Yadav, Department of Physics, IIT Roorkee for providing the infrastructure facilities. I would like to express my thanks to all the teaching and non-teaching staff of the Physics department. I gratefully acknowledge the financial support provided by MHRD and DST (Govt. of India) during my PhD.

My family has always been my biggest support with PhD being no exception. They are my silver linings and have kept me going even when the times were tough and things seemed uncertain. My love mumy, papa, Payal, mausi, nana and nani are my pillars of strength and I can't express my deep gratitude enough in words. I would also like to thank my in-laws and family for their warm love and support in this journey of mine. Nevertheless, I wish to express my love and appreciation for my husband Ashish, for being so supportive and understanding in everything especially towards my career.

Friends are the family which we choose. And I am thankful to the almighty to have been blessed with such friends who made these five years memorable and special. Archna mam has been my friend (but obvious), support, pillar and motivator all along. She made these five years at the hostel enduring. I am thankful for the beautiful memories and time spent with Nisha, Manju, Anushri, Kalyani, Viren, Shikha, Vidushi, Pragya and all my fellow lab mates whom I have missed out here.

In the end, I thank god for being the force which is keeps me going in life.

Date: --/--/----

Sheetal Rawat

DEDICATIONS

This thesis is dedicated to my parents.

CONTENTS

LIST OF FIGURES

CHAPTER 1

CHAPTER 2

CHAPTER 3

CHAPTER 4

CHAPTER 5

CHAPTER 6

LIST OF TABLES

CHAPTER 1

Introduction

This chapter discusses the need for carrying out the PSD ability and efficiency of GGAG:Ce scintillator.

1.1 Background

Through the years, radiation detectors have led to the important discoveries and inventions in the field of science [1-6]. They have either triggered the research development further or provided it a new direction. The Sidot's blende or crystalline zinc sulphide was the key element in the discovery of radioactivity by Nobel Prize awardee, Henri Becquerel [7]. The revolution in the medical industry was brought by the X-rays whose existence became known to W. Roentgen by a fluorescent screen painted with barium platinocyanide [8]. Sir William Crookes developed an apparatus named "spinthariscope" (see Figure 1.1), consisting of ZnS screen for counting light flashes [9,10]. Rutherford used the very same instrument in the historic alpha particle scattering experiment leading to the discovery of the atomic nucleus [11-13]. The phosphorescent barium platinocyanide and ZnS were the scintillation materials used to detect X-rays, gamma rays, alpha particles in the above mentioned discoveries. Scintillators fall under the category of radiation detectors. The advances made in the radiation detectors since 19th century has been so astounding that it can be compared with the advancement of the modern computer from the abacus.

Figure 1.1 The Spinthariscope.

A radiation detector consists of two components: the detector material and the electronics that provide us the signal, which is later interpreted and processed to extract information [14]. The photo sensors are the associated electronic instruments which has also undergone metamorphosis with the detector material. From bulky photomultiplier tubes to compact semiconductor diodes such as p-i-n diodes, avalanche photomultiplier diodes (APD) and the latest are silicon photomultipliers (SiPM)

[15]. There is more to the radiation detectors than just informing us about the presence of radiation. They provide information on the energy, amount, type and position of incident radiation. In today's world, radiation detectors have wide applications in scientific research areas and industries of high energy physics, radiochemistry, nuclear physics, astrophysics, geophysics, medical industry, national security, oil and well logging industry, food industry, space exploration and so on [16-22]. Radiation detectors are used in these applications because they utilize X-rays, electrons, protons, neutrons or ion beams for the characterization, analysis and diagnostic purposes. For example, in medical imaging high resolution measurement of spatial distribution and depth of interaction (DOI) is important. While in national security, efficient detection of gamma rays and neutrons from keV to MeV range of energies is of our primary concern [23].

1.2 Scintillators

There are different types of radiation detectors such as gas filled ionization detectors, scintillation detectors, semiconductor detectors, etc. Among these, scintillators are the most widely used class of radiation detectors owing to their capabilities and versatility in wide range of applications. Scintillator is an inorganic or organic material whereby the absorption of energy from nuclear radiation (e.g., α particles, β particles, heavy ions, X-rays or γ-rays) results in the emission of visible light [24,25]. An ideal scintillator material should possess the following properties [19,21]:

- high detection efficiency
- proportional light response
- low cost
- chemical stability
- resistance to thermal and mechanical shock
- high-count rate capability
- good timing resolution
- good energy resolution
- emission wavelength suitable to photo sensor
- radiation hardness
- good light transmission from scintillator to photodetector

No material meets all criteria, and the choice of a particular scintillator is always a compromise among these factors [26].

The most widely used scintillators are the inorganic crystals due to their greater stopping power owing to high density and effective atomic number i.e. greater ability to absorb energy of impinging radiation [27]. The development of PMT in 1940s and the discovery of thallium activated NaI scintillator in 1950s by Hofstadter began the period of inorganic single crystals reign in radiation detectors [28]. In next few years, scintillation properties of different alkali halides with various activator combinations were investigated [29]. Ceramics and glass scintillators have also emerged capable of radiation detection [30]. However, scintillators in single crystal form offer numerous advantages compared to gas, liquid and semiconductors based detectors [31]. The brief introduction of single crystals has been discussed as follows.

1.3 Single crystals

A single crystal or monocrystalline solid is a material in which the crystal lattice of the entire sample is continuous and unbroken to the edges of the sample, with no grain boundaries [32]. They are compact in size, have high detection efficiencies and are transparent to the emitted light for maximum light collection. They have no grain boundary and their ordered formation state reduces scattering of light inside the crystal. They can be doped with apt activators for various applications [33]. Radiation hardness, reproducibility and reliability of results make them the most sought after form of scintillator materials. They are the most significant field of material science engineering which involves the controlled phase transformation from fluid to solid crystalline phase. The processing of the grown single crystal is done as per the requirement by optimizing various parameters during the single crystal growth. The new single crystals evolution started back with the invention of the solid state transistor in 1948. In order to assess the device properties, many new crystals have been grown and fabricated since 1948. The application of semiconductors based electronics have created an enormous demand for single crystals of high quality and purity for semiconductor, ferroelectric, piezoelectric, oxide etc. The growth of single crystal needs multi-disciplinary research and requires material scientists, engineers, chemists and physicists to work hand in hand to develop the technology [34]. Since 18^{th} century, we were aware of the experimental fundamental aspects of the crystal growth; however the actual advancement in this field started after the development of thermodynamics by the end of 19^{th} century and with the progress in nucleation and crystal growth theories [35]. The methods for growing crystals are mainly governed by the properties such as expansion, conductivity, viscosity, chemical stability and requirement of composition, size and quality [32,35].

The single crystals can be grown from solution, melt or vapours [36]. The various methods used for the growth of single crystals according to their percentage use have been shown in the Figure 1.2 [37,38].

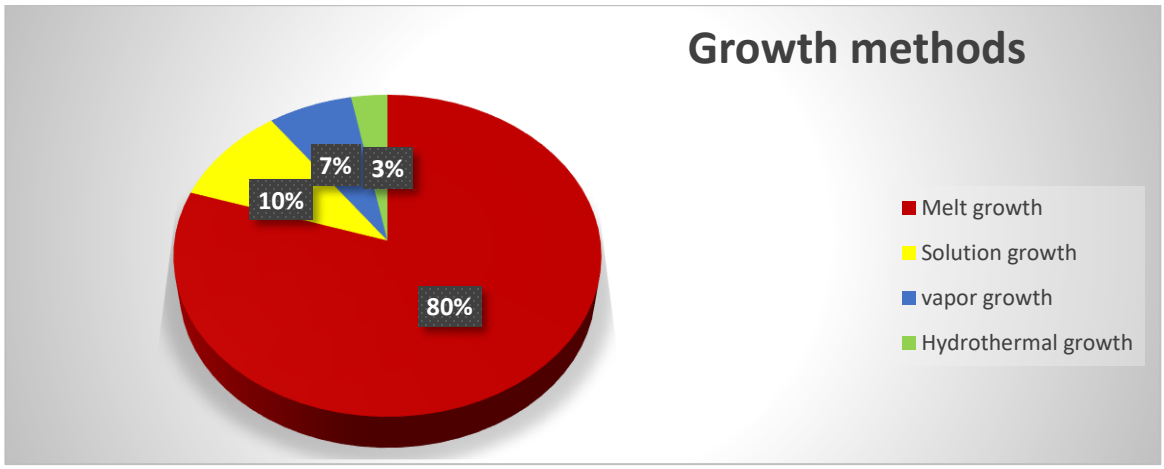

Figure 1.2 A pie chart showing percentage of crystals grown using various methods [37,38].

The growth of single crystals from melts is the most popular method to grow large size single crystals. Melt growth techniques accounts for about 80% of the single crystal growth taking place commercially and industrially worldwide [39]. Melt techniques offer control over parameters such as ambient, convection, temperature gradient and orientation during growth. Ideally all the crystals can be grown from their melts if they can melt congruently and do not undergo phase transition during melting. The majority of single crystal scintillators are grown from melt using the Czochralski or Bridgman techniques because of the fast growth rate, control over nucleation and cost-effectiveness. These techniques were employed to grow crystals used in the thesis work, therefore, they have been discussed in detail in the next chapter [32-35]. A steady growth has appeared in the discovery of new scintillator materials with the advancement in technology and material science engineering. Concurrently, the use of synchrotron radiation and laser technology has further helped us to understand the complexities of defect formations, excitons, electron-phonon relaxation and various processes involved in scintillation [40].

1.4 Scintillation mechanism

The scintillation mechanism can be summed up in three steps: conversion, transport and luminescence [40]. Figure 1.3 shows the schematic diagram presenting scintillation mechanism in three steps.

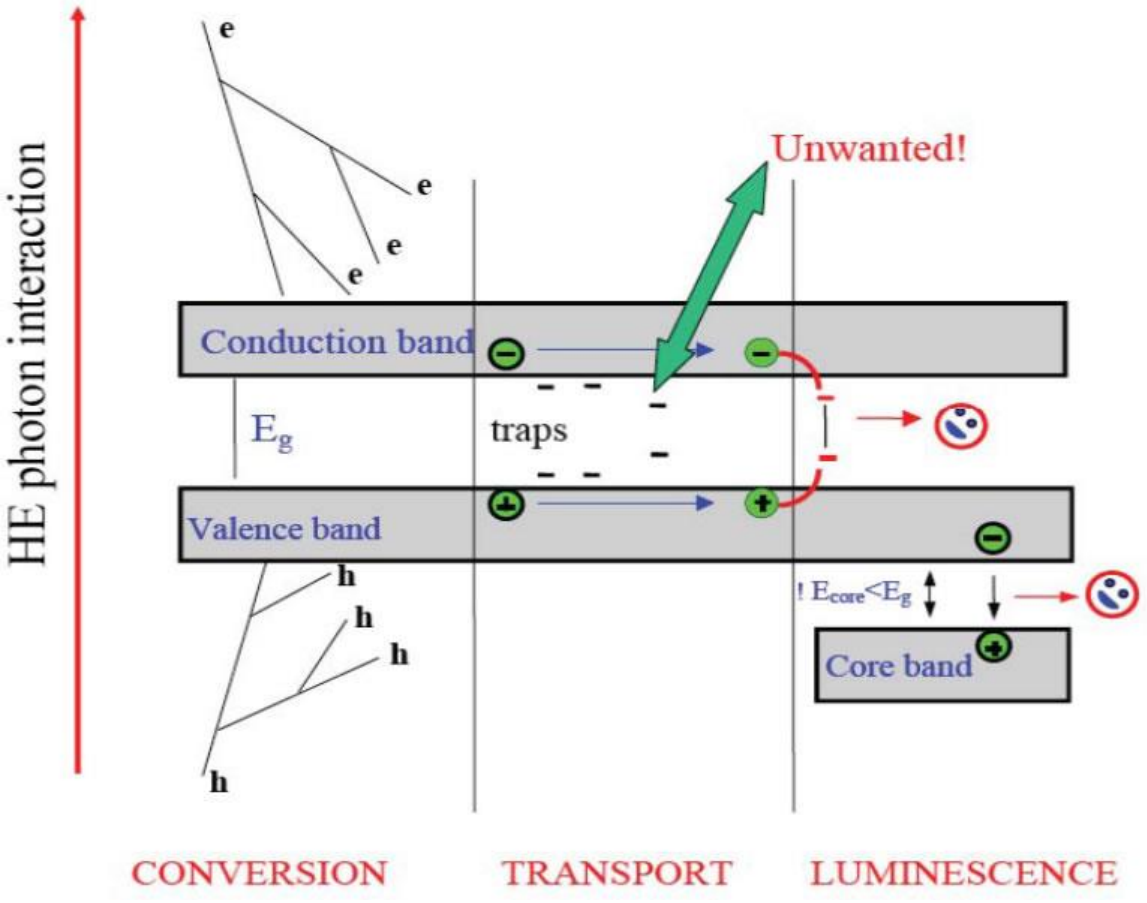

Figure 1.3 The three stages of scintillation [41].

Step - 1: The incident radiation interacts with scintillating material and produces an ionization event. The event results in inner shell hole and an energetic electron creation followed by radiative, non-radiative decay and inelastic scattering of electrons. The time taken to complete conversion process is 10^{-15} to 10^{-13} seconds.

Step - 2: When ionization energy threshold is reached then hot electrons and holes thermalize by intraband transitions and relaxation. The relaxation mechanism is different for electrons and holes due to the different transportation mechanism owing to their masses. Excited electron either relax radiatively by emitting a visible photon or non-radiatively by releasing a secondary electron called Auger electron. This cascade of events leads to the loss of energy of the electron in the form of electron-phonon relaxation. At the end of thermalization process, the number of e-h pairs generated is thus proportional to the energy of incident radiation. Luminescent sites are excited by hot electrons, e-h or h-e capture and sensitizer-activator transfer of energy in the time domain 10^{-12} to 10^{-8} seconds [21].

Step - 3: The activator ions act as luminescent sites for e-h traps. The recombination of e-h pair at the luminescent site of dopant ions results in non-radiative quenching or emission of a visible photon. The e-h recombination can take as short as 10^{-9} seconds or last up to several minutes in case of forbidden processes. Luminescence can be intrinsic and extrinsic. In intrinsic luminescence, the self-trapped excitons are the energy carriers to the luminescence centres and in extrinsic luminescence, the dopant ion itself is the luminescent species [21].

Thus, material science and engineering can play a crucial role in the development of existing and new scintillator materials. Different aspects of material science i.e. crystallography, solid state physics, luminescence, photonics, defects in solids can cumulatively lead to the advancement of a near ideal scintillator material [23]. Research in scintillator materials includes (a) better understanding and mechanism models of radiation detector physics; (b) improving characterization and response of specific material properties; (c) advancement in synthesis and screening approach for materials processing; (d) use of simulation, informatics and modelling for single crystal synthesis and (e) rigorous development of novel scintillators.

1.5 Cerium doped Gadolinium gallium aluminium garnet (GGAG:Ce)

Until the discovery of SrI_2:Eu and KSr_2I_5:Eu scintillators in 2008 and 2015 respectively, the best performing scintillator has been $LaBr_3$:Ce with an excellent resolution of 2.6% and light yield of about 60,000 ph/MeV [42-44]. The relatively weak (1 0 0) cleavage plane, hexagonal crystal structure with considerable anisotropy in properties like thermal expansion, make the growth of large volume $LaBr_3$:Ce crystals very difficult. Moreover, it exhibits intrinsic radioactive background due to naturally occurring ^{138}La and actinium contamination. Actinium's chemically similarity to lanthanum makes their separation difficult. Actinium contamination is found at ~1.6–3.0 MeVee, resulting in large background for gamma spectroscopy [45-48]. Although no detector can surpass HPGe detectors in terms of energy resolution, it has poor gamma detection efficiency [49].

The total energy resolution of a scintillation detector depends on the intrinsic resolution of the crystal, transfer resolution, statistical contribution of PMT or the photo-diode and the dark noise contribution connected with the detector's current and the noise of the electronics. In general, the major contribution to total energy resolution of a detector is the intrinsic resolution, which arises due to the non-proportionality of light output of the crystal by means of scattering of electrons (δ - rays) and Landau fluctuations. The contribution dye to electronics noise is negligible in the case of the PMT readout [29].

With the advancement in technology, it is now possible to design a scintillator for specific purpose. There is a choice for bandgap adjustment and introduction of activator energy levels. Properties of some of the recently developed good scintillators have been tabulated in the Table 1.1.

Table 1.1 Properties of some scintillation detectors.

Property	**GGAG:Ce** [50]	**CsI:Tl** [51],[52]	**$LaBr_3$:Ce** [53]	**$LaCl_3$:Ce** [42],[54]	**SrI_2:Eu** [43]
Density (g/cm^3)	6.70	4.51	5.10	3.86	4.59
Z_{eff}	55	54	46.9	59.5	49.4
Maximum emission wavelength (nm)	550	550	380	352	435
Decay time(ns)	55	1000	16	26	1000
Light yield (ph/MeV)	~55,000	~54,000	~70,000	~46,000	~115,000
Energy resolution at 662 keV	~6%	~7%	~2.6%	~3.3%	~3.0%
Timing resolution (ns)	0.9	13	0.1	0.256	-
Internal radioactivity	-	-	0.2-0.8 Bq/cm^3 [45]	0.04-0.8 Bq/cm^3 [46]	-

Currently available scintillators which exhibit near optimum values for some of the mentioned ideal properties are listed in Table 1.2 [55]. Among oxide scintillators, YAG and LuAG garnets have been extensively studied and are being widely used in laser physics applications. A new multicomponent cerium doped gadolinium gallium aluminium garnet (GGAG:Ce) single crystal scintillator is a consequence of bandgap engineering resulting from the optimized substitution of Gd or Ga ions in YAG:Ce, LuAG:Ce single crystals [56-59]. The optimized ratio of Ga/Al of 3/2 has been reported for the best combination of high light output and fast decay time [50].

Table 1.2 Examples of currently available scintillators [55].

Scintillator Property	Scintillators	Yield (ph/MeV)	Factors affecting the theoretical limit	Possible future materials
Light output	$LaBr_3$:Ce+Sr, SrI_2:Eu, KSr_2I_5:Eu	88,000, 110,000, 95,000	Energy to create an e—h pair, energy transfer efficiency to luminescence centre, high quantum efficiency	$LnPO_4$:Ln, $K_3Ln(PO_4)_2$:Ln, CuI (near band edge semiconductors)
Energy resolution	$LaBr_3$:Ce, SrI_2:Eu, KSr_2I_5:Eu	2.6%, 2.7%, 2.4%	High photon statistics, proportional energy response	Mixed rare earth halides
Decay time	BaF_2 (core-valence luminescence) LaF_3:Nd (electric dipole emission)	0.6 ns 6 ns	Oscillator strength, refractive index, wavelength	Pr^{3+}, Nd^{3+} and Yb^{3+} -doped compounds; near band edge semiconductors (CuI, ZnO:Ga)
Density	Lu_2O_3:Eu (ceramic)	9.4 g/cm^3	Crystal lattice and structure	Pb, Ln, Tl, Bi compounds
Effective atomic number	$PbWO_4$ $Bi_4Ge_3O_{12}$	76 75	Atomic number	Pb, Ln, Tl, Bi compounds
Cost	$PbWO_4$	Approx. \$2/cm^3	Raw materials, growth method and equipments installed	Ceramics

It exhibits high density (6.7 g/cm^3), high effective atomic number (55), high light yield (about 60,000 ph/MeV) and fast decay time (55 ns) [60]. The crystal structure of $Gd_3Ga_3Al_2O_{12}$ is shown

in Figure 1.4. GGAG like other garnets has cubic structure of $A_3B_2C_3O_{12}$, where *A*, *B* and *C* cations have three sites. Gd (*A* site) is a dodecahedral site, Ga/Al (*B* site) and Ga/Al (C site) are octahedral and tetrahedral sites, all coordinated with oxygen. When GGAG is doped with Ce^{3+} ions, replacement of Gd^{3+} ions at *A* site occur. This leads to dodecahedral coordination of Gd^{3+} ions with oxygen having D2 point group symmetry [61].

These lucrative scintillation characteristics are due to a strong decrease of the trap centre concentration at bottom of the conduction band, thereby, preventing the ionization induced quenching of the excited 5d level of the Ce^{3+} activator ion [61]. They have garnered huge interest in medical imaging field for PET, SPECT applications due to their fast timing and high density characteristics. Moreover, the synthesis and mechanical processing of GGAG crystals is relatively easy, optimized and their non-hygroscopic nature makes them easy to handle [50, 62-63]. As a consequence the cost gets highly reduced. The GGAG:Ce single crystal scintillator's optical, scintillation and electronic properties have been finely tuned by doping and co-doping concentrations [50, 61].

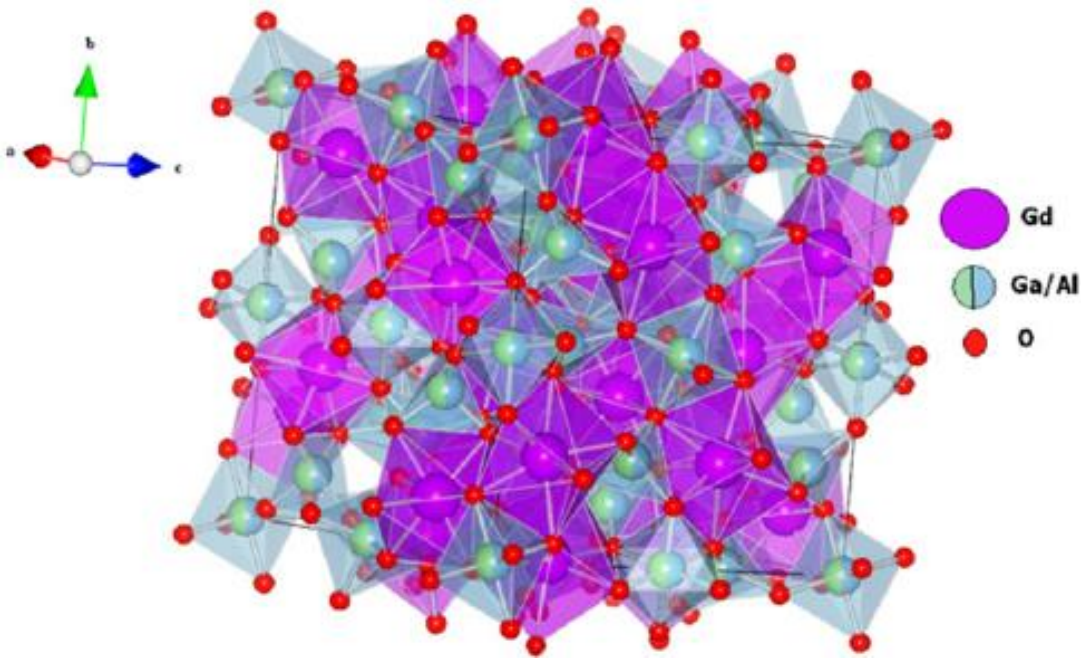

Figure 1.4 Crystal structure of $Gd_3Ga_3Al_2O_{12}$ [61].

1.6 Literature survey on GGAG:Ce scintillator

Efforts to improve the light output, energy resolution, scintillation decay time and coincidence timing resolution of GGAG:Ce scintillator are going on [64]. Several groups around the world have

studied the properties of GGAG:Ce [65-67]. However, some of its properties and applications, as listed below, have not been explored so far:

1. Detection of charged particles, gamma rays and neutrons together based on Pulse-shape discrimination (PSD) technique
2. Effect of co-doping on its PSD property
3. Dependence of gamma energy and source-to-detector separation on detection efficiency
4. Scintillation decay kinetics of heavy ions having high ionization density
5. Radiation hardness
6. Intrinsic resolution of Compton electrons to study the non-proprtionality
7. Growth of large volume single crystals

Different types of nuclear radiation interact with matter by means of different mechanisms. In the case of interaction of nuclear radiation with scintillator, there will be production of visible photons. When a gamma ray interacts with a single crystal scintillator, its primary loss of energy is through photoelectric effect, Compton scattering and pair production depending on its incident energy and the effective atomic number of the scintillator material [26]. The probability of photoelectric absorption (τ) is proportional to Z^n where "n" is in between 4 and 5. Compton scattering probability (σ) is proportional to the Z and the pair production probability (κ) is proportional to Z^2. However, charged particles interact through ionization and scattering resulting in the production of visible photons. The difference in pulse shapes due to different types of interacting nuclear radiation can be used to determine the type of interacting radiation by using a process called pulse shape discrimination (PSD). Some of the PSD techniques developed till now are: zero crossing, charge integration, pulse gradient analysis, neural network, fuzzy algorithm, cross correlation with a template pulse, principal component analysis [68-72]. The performance of the PSD methods highly depends on the radiation detector and the energy range being investigated. Out of all PSD methods, zero crossing and charge integration PSD techniques have been applied for decades. However, with the advancement in the solid state semiconductor technology such as field programmable gate array and analog-to-digital converter, digital methodologies of PSD have started replacing the analog ones. They have been implemented in digital domain using recursive algorithm. Digital techniques of PSD allow users to carry out real time analysis without the hassle of electronic hardware [73].

Trans-stilbene was the first scintillator with which PSD technique has been applied for the discrimination of neutrons and gamma rays [74-76]. Since then PSD has been applied in radiation

detection mechanism employing scintillation and semiconductor detectors [77, 78]. For charged particle detection, radiation detectors such as ionization chambers, proportional counters and scintillation counters were being used. However, gamma rays in the form of background radiation restricts the accurate detection and measurement of charged particles using scintillation detectors. This problem has been resolved by employing PSD techniques for the detection of a particular radiation in a mixed field.

Thallium doped CsI is a benchmark inorganic single crystal scintillator for the detection of charged particles with energies ranging from E/A = 30-200 MeV [79]. It is less hygroscopic than commercially used NaI:Tl scintillator, affordable unlike solid state detectors and can be grown in large sizes of any shapes. CsI:Tl is most often used as alpha particle detector because of its high light output (60,000 ph/MeV) [80]. However, CsI:Tl is a slow scintillator whose scintillation decay time is of the order of microseconds. Apart from having similar light output (60,000 ph/MeV) and emission wavelength at 550 nm, GGAG:Ce scintillator offers fast decay time (55 ns) and high density (6.27 g/cm^3) compared with that of CsI:Tl scintillator (0.6 μs and 4.51 g/cm^3) [60, 80]. These characteristics have led to the extensive research of GGAG:Ce scintillator for the charged particle detection. Decay time of CsI:Tl consists of two components: fast and slow. GGAG:Ce scintillator also exhibits two decay components for alpha particles and gamma rays and its PSD ability has been studied by Tamagawa *et al* [81]. The ratio between these two components and the average decay time depends on the nature of incident radiation, thus, exhibiting the PSD ability. The effect of co-dopants such as boron, calcium, barium, magnesium in GGAG:Ce single crystal has been widely studied in terms of its scintillation and optical characteristics [59]. Boron co-doping has resulted in the light yield improvement while Ca^{2+} and Mg^{2+} co-doping have led to the efficient reduction in the decay time of the GGAG:Ce scintillator. However, the PSD in boron co-doped GGAG:Ce has not been studied so far.

PSD depends on the decay time which in turn relies on the scintillation kinetics of the crystal. Therefore, it becomes mandatory to decipher the complex scintillation kinetics of alpha particles and gamma rays in GGAG:Ce single crystals for the improvement and understanding of PSD ability. PSD technique improves background rejection capability in double beta decay experiments, suppresses high gamma background in mixed field radiation, background rejection to achieve sensitivity to the solar neutrino signals [77,78].

PSD technique is also extensively used by phoswich detector to identify different types of nuclear radiation. Phoswich is a detector which is a sandwich of two or more scintillators coupled

to a same PMT. White and Miller [82] developed a phoswich detector consisting of three single crystals for simultaneous detection of alpha, beta and gamma radiation. When the phoswich detector is operated in anti-coincidence mode, event signal pulses from the primary front detector are accepted only when there is no coincidence signal from the back guard detector. This configuration results in efficiently shielding and lowering of the background when compared to the available conventional detectors. Choice of the scintillators for the phoswich detector is done on the basis of the properties such as decay time, light output, efficiency for charged particles, gamma rays, X-rays or neutrons, radiation hardness, etc [83-84].

Many applications such as gamma spectroscopy, high energy physics and national security require detectors with high Z_{eff} and high density [85-90]. For activity measurements also, the knowledge of absolute efficiency of the detector is important. Therefore, high detection efficiency (both total detection and photo-peak) instigate researchers to look for scintillators with high density and large atomic number. The detection efficiency is a measure of the percentage of radiation that a given detector detects from the overall yield emitted by the radioactive source [91, 92]. The measured efficiency depends on source-detector geometry, energy of incident radiation, absorption cross-section in the material and attenuation layers in front of the detector [93]. GGAG being a high density crystal can accomplish the high detection efficiency characteristic which has not been studied till now.

1.7 Thesis overview

In the thesis work, we have made extensive studies on PSD and detection efficiency of GGAG:Ce scintillators. The work has been carried out in Radiation Detectors and Spectroscopy laboratory, Indian Institute of Technology Roorkee and Crystal Technology Laboratory, Technical Physics Division, Bhabha Atomic Research Centre, Mumbai. The thesis has been presented in seven chapters as explained below:

The chapter-2 presents various methods used to grow single crystals. The single crystals studied in this work have been grown by the Czochralski technique and Bridgman method. A description of characterization techniques used in this work has been given. Compositional and structural characterization has been carried out using powder X-ray diffraction (XRD) and Laue reflection patterns. Optical properties were studied using UV-VIS spectrophotometer, photoluminescence spectrometer and X-ray stimulated luminescence techniques. The working principles of photo sensors such as photomultiplier tube and silicon photomultiplier (SiPM) were described. The scintillation characterization of decay time measurement using oscilloscope, PSD using charge

integration and zero crossing method and fabrication of gamma detectors from as-grown single crystals have been described in this chapter.

Chapter-3 demonstrates the comparison between PSD abilities of boron co-doped GGAG:Ce and CsI:Tl scintillators coupled to PMT and SiPM. Studies on PSD characteristics for gamma rays and alpha particles were done by employing a digitizer and zero crossover setup. The comparison of the PSD ability of crystals coupled to PMT as well as with SiPM for alpha radiations and gamma rays has been illustrated in detail. The figure of merit and zero-crossing time for GGAG:Ce,B and CsI:Tl single crystals have been measured and reported. We have observed, for the first time, that the behaviour of scintillation decay times of GGAG:Ce,B scintillator is opposite to that of CsI:Tl single crystal [61]. The average scintillation decay times for GGAG:Ce,B crystals has been found to be fast for alpha excitations compared to that for gamma rays. These values were found to slightly degrade in the case of SiPM coupled crystals [61].

Besides PSD studies, gamma detection efficiency of GGAG:Ce scintillator was studied and discussed in chapter-4. As in gamma spectroscopy, apart from having high light output, good energy resolution and timing resolution, it is the high efficiency (both total detection (TDE) and photo-peak (PE)) of the detector which is of paramount importance. The high density (6.7 g/cm^3) and atomic number (55) of GGAG:Ce scintillator make it a suitable detector for many applications. In this chapter, we have discussed detailed realistic Monte Carlo simulations of absolute efficiencies (both total detection and photo-peak) of GGAG:Ce scintillator for gamma rays up to energy of 5 MeV and for different values of source-to-detector separation. Simulations were also made with different scintillators ($LaBr_3$:Ce, NaI:Tl, CsI:Tl, BaF_2 and SrI_2:Eu) for comparison. In order to validate these simulations, we have made experimental measurements with GGAG:Ce, CsI:Tl and BaF_2 detectors having dimensions of 18 mm × 18 mm × 10 mm, 25.4 mm × 10 mm and 30 mm × 30 mm respectively and for different values of source-to-detector separation considering ^{137}Cs source. A good agreement between simulated and measured results has been found [91].

In chapter-5, we have discussed a novel approach to explain PSD property and scintillation kinetics of GGAG:Ce scintillators using optically stimulated luminescence (OSL). The GGAG:Ce crystals were also grown with boron and calcium co-dopants using the Czochralski technique. The co-doping was found to have substantial effects on the PSD ability of these scintillators [95]. A significant difference in the pulse-shapes for alpha and gamma radiations was observed in B co-doped GGAG:Ce scintillators while the difference observed in Ca co-doped crystals was quite insignificant. Consequently, B co-doped crystals exhibited the highest PSD while those with Ca co-

doping showed no discrimination in spite of having strong quenching of the light yield by alpha radiations that resulted in a minimum α/γ ratio. Thermolumeniscence (TL) and OSL studies with infrared, blue and green light provided an insight into the role of defect centres in the relaxation mechanism of the scintillation kinetics of GGAG:Ce crystals which subsequently affects their ability of discriminating different kinds of radiation [94].

Chapter-6 is an extension of the PSD work presented in chapter-3. We have developed a novel phoswich detector consisting of two different single crystal scintillators to discriminate various types of nuclear radiation with an excellent figure of merit. The high pulse-shape discrimination (PSD) for various types of nuclear radiation has been achieved by a novel combination of Boron co-doped $Gd_3Ga_3Al_2O_{12}$:Ce (GGAG) crystal coupled to a CsI:Tl (CsI) single crystal. This combination was optically coupled to a single photomultiplier tube and desktop digitizer to build a compact detector setup. The figure of merit of phoswich detector for discriminating alpha and gamma radiations was found to be twice that of the individual crystals. In addition, the gamma ray interacting in the front GGAG crystal and back CsI crystal could also be discriminated with a high figure of merit making it suitable for the medical imaging applications. The presence of Gd in GGAG further imparts the capability to detect thermal neutrons in mixed fields. The observed exceptional improvement of the discrimination ability along with the versatility opens a large scope for the use of this combination in various applications [95].

Chapter-7 presents the summary of the thesis work along with the future scope.

References of chapter 1

[1] Sritharan, K., Manikandan V., Srinivasan K., Linear and non-linear optical characterization of methyl-p-hydoxybenzoate (p-MHB) single crystal grown by TSSG method, *Optics and Laser Technology* **91**, 51-54 (2017).

[2] Jang, J., Kim, H. J., Rooh, G., Kim, S., Development and measurement of luminescence properties of Ce-doped $Cs_2LiGdBr_6$ crystals irradiated with X-ray, γ-ray and proton beam, *Journal- Korean Physical Society* **71**, 796-801 (2017).

[3] Hofstadter, R., Alkali halide scintillation counters, *Phy. Rev.* 74, 100-101 (1950).

[4] Korxhik, M., Lecoq, P., Search of new scintillation materials for nuclear medicine applications. *IEEE Trans. Nucl. Sci.* **48**, 628-631 (2001).

[5] Maj, A.,....Zieblinski, M., *The PARIS project Acta Physica Polonica B*, **40**, 565-575 (2009).

[6] CMS Collaboration, Chatrchyan, S., Khachatryan, V., Sirunyan, A. M., Tumasyan, A., Adam, W., Aguilo. E.,.… Wenman, D., Observation of a new boson at a mass of 125 GeV with the CMS experiment at the LHC. *Physics Letters B* **716**, 30-61 (2012).

[7] Becquerel, H., 1903. On radioactivity, a new property of matter. In: Nobel Lectures, Physics 1901-1921, Elsevier Publishing Company, Amsterdam, 1967.

[8] Arthur, C. Google doodle celebrates 115 years of X-rays, The Guardian. Guardian US. Retrieved 5 February 2019.

[9] Crookes, W., The emanation of radium. *Proc Royal Soc. (London) A* **71**, 405-408, 1903a.

[10] Crookes, W., Certain properties of the emanation of Radium. *Chem. News* **87**, 241, 1903b.

[11] Rutherford, E., Chadwich, J., Ellis, C. D., Radiations from Radiaoactive Substances, Cambridge University Press, Cambridge (1930).

[12] Kolar, Z. I., den Hollander, W., 2003: A centennial of spinthariscope and scintillation counting. *Appl. Radiat. Isot.* **61**, 261-266 (2004).

[13] Rutherford, E., Collison of α-particles with light atoms. *Nature (London)* **103**, 415-418 (1919).

[14] Kallman, H., Scintillation counting with solutions. *Phts. Rev.* **78**, 621-622 (1950).

[15] Renker, D., Photosensors. *Nucl. Instrum. Methods Phys. Res. Sect. A* **527**, 15-20 (2004).

[16] Ciemala, M.,....Maj, A., Measurements of high-energy -rays with $LaBr_3$:Ce detectors, *Nucl. Instrum. Methods Phys. Res. Sect A* **608**, 76-79 (2009).

[17] Nikl, M., Yoshikawa, A., Vedda, A., Fukuda, T., Development of novel scintillator crystals, *J. Cryst. Growth* **292**, 416-421 (2006).

[18] Melcher, C. L., Perspective on the future development of new scintillators. *Nucl. Instrum. Methods Phys. Res. Sect. A* **537**, 6-14 (2005).

[19] Novotny, R., Inorganic scintillators—a basic material for instrumentation in physics. *Nucl. Instrum. Methods Phys. Res. Sect. A* **537**, 1-5 (2005).

[20] Moses, W. W., Current trends in scintillator detectors and materials, *Nucl. Instrum. Methods Phys. Res. Sect. A* **487**, 123-128 (2002).

[21] Derenzo, S. E., Weber, M. J., Bourret-Courchesne, E., Klintenberg, M. K., The quest for the ideal inorganic scintillator, *Nucl. Instrum. Methods Phys. Res. Sect A* **505**, 111-117 (2003).

[22] Vedda, A. et al., Thermoluminescence of Zr-codoped $Lu_3Al_5O_{12}$:Ce crystals, *Phys. Status Solidi A* **195**, R1-3 (2003).

[23] Milbrath, B. D., Perrrung, A. J., Bliss, M. and Weber, W. J., Radiation detector materials: An overview, *J. Mater. Res.* **23**, 2561 (2008).

[24] Van Eijk, C. W. E., Inorganic-scintillator development, *Nucl. Instrum. Methods Phys. Res. Sect. A* **460**, 1-14 (2001).

[25] Farsoni, A. T., and Hamby, D. M., A system for simultaneous beta and gamma spectroscopy, *Nucl. Instrum. Methods Phys. Res. Sect. A* **578**, 528-536 (2007).

[26] Knoll, G. F., Radiation Detection and Measurement, 4th edn. New York: John Wiley & Sons, 2010.

[27] Higgins, W. M., Glodo, J., van Loef, E., Klugerman, M., Gupta, T., Cirignano, L., Wong, P., Shah, K. S., 2006. Bridgman growth of $LaBr_3$:Ce and $LaCl_3$:Ce crystals for high-resolution gamma-ray spectrometers, *J. Cryst. Growth* **287**, 239-242.

[28] Hofstadter, R., 1950. Properties of scintillation materials, *Nucleonics* **6**, 70-72.

[29] Moszynski, M., 2003. Inorganic scintillation detectors in γ-spectroscopy, *Nucl. Instrum. Methods Phys. Res. Sect. A* **505**, 101-110.

[30] de Faoite, D., Hanlon, L., Roberts, O., Ulyanov, A., McBreen, S., Tobin, I., and Stanton, K. T., 2015. Development of glass-ceramic scintillators for gamma-ray astronomy, *J. Phys.*: *Conf. Ser.* **620**, 012002.

[31] Senguttuvan, N., Mohan, P., Moorthy Babu, S., and Subramanian, C., 1998. Czochralski growth of lead tungstate single crystals and their characterization, *J. Cryst. Growth* **183**, 391-397.

[32] Brice, J. C., Crystal growth processes 1986, Blackie Academic & Professional (an Imprint of Chapman & Hall).

[33] Benz, K. W., Neumann, W., and Mogilatenko, A., 2014. Introduction to Crystal Growth and Characterization, Wiley.

[34] Single crystals, Wikipedia.

[35] Toschev, S., 1973. Crystal Growth: An Introduction, ed. P. Hartman, North Holland, Amsterdam.

[36] Scheel, H. J., 2000. J. *Cryst. Growth* **211**, 1-517.

[37] Singh, S. G., October 2014. PhD Thesis, Effect of growth processes on characteristics of some technologically important oxide and halide crystals.

[38] Patra, G. D., January 2017. PhD Thesis, Single Crystal Growth of Lithium Tetra Borate and its Characterization as a Multi-functional Material for Personal Dosimetry.

[39] Singh, A. K., August 2018. PhD Thesis, Growth and Characterization of $Li_6R(BO_3)_3$:R (R:Rare Earth ions): Promising neutron detector.

[40] Rodnyi, P. A., 1997. Physical processes in inorganic crystals, CRC Press.

[41] Nikl, M., 2006. Scintillation detectors for x-rays, *Meas. Sci. Technol.* **17**, R37–R54.

[42] van Loef, E. V. D., Dorenbos, P., van Eijk, C. W. E., Kramer, K., Gudel, H. U., 2001. High energy resolution scintillator: Ce^{3+} activated $LaBr_3$, *App. Phys. Letters* **79**, 1573.

[43] Pankratov, V., Popov, A. I., Shirmane, L., Kotlov, A., Bizarri, G. A., Burger, A., Bhattacharya, P., Tupitsyn, E., Rowe, E., Buliga, V. M., Williams, R. T., 2013. Luminescence and ultraviolet excitation spectroscopy of SrI_2 and SrI_2:Eu^{2+}, *Rad. Meas.* **56**, 13.

[44] Stand, L., Zhuravleva, M., Lindsey, A., Melcher, C. L., 2015. Growth and characterization of potassium strontium iodide: A new high light yield scintillator with 2.4% energy resolution, *Nucl. Instrum. Methods Phys. Res. Sect. A* **780**, 40.

[45] Hartwell, J., and Gehrke, R., 2005. Observations on the background spectra of four $LaCl_3$(Ce) scintillator detectors, *Appl. Radiat. Isot.* **63**, 223-228.

[46] Milbrath, B., Runkle, R. C., Hossbach, T. W., Kaye, W. R., Lapel, E. A., McDonald, M. C., and Smith, L. E., 2005. Characterization of alpha contamination in lanthanum trichloride scintillators using coincidence measurements, *Nucl. Instrum. Methods Phys. Res. Sect. A* **547**, 504-510.

[47] Kernan, W., 2006. Self-activity of lanthanum halides, *IEEE Trans. Nucl. Sci*. **53**, 395-400.

[48] Negm, H., Omer, M., Zen, H., Daito, I., Kii, T., Masuda, K., Hori, T., Ohgaki, H., Hajima, R., Hayakawa, T., Shizuma, T., Kikuzawa, N., and Toyokawa, H., 2013. Monte Carlo simulation of response function for $LaBr_3$(Ce) detector and its internal-activity, *3rd International*

Conference on Advancements in Nuclear Instrumentation Measurement Methods and their Applications Conference Proceedings.

[49] Zhou, X. W., Doty, F. P., Yang, P., 2009. Dislocations in $LaBr_3$ crystals, *Proc. of SPIE* **7450**, 745005.

[50] Kamada, K., Yanagida, T., and Pejchal, J., 2011. Scintillator-oriented combinatorial search in Ce-doped $(Y,Gd)_3(Ga,Al)_5O_{12}$ multicomponent garnet compounds, *J. Phys. D: App. Phys.* **44**, 505104.

[51] Jiang, H., Hoffman, D. M., and Vartuli, J. S., 2004. CT Detector Array having Non-Pixilated Scintillator Array, *United States Patent Application*, 20040218712 A1.

[52] Brinckmann, P., 1965. Csl(Na) scintillation crystals, *Phys. Letters* **15**, 305.

[53] Chewpraditkul, W., Wanarak, C., Moszynski, M., and Swiderski, L., 2012. Comparison of $Lu_3Al_5O_{12}$:Ce and $LaBr_3$:Ce scintillators in gamma-ray spectrometry. *Adv. Mater. Res.* **418**, 922.

[54] Dorenbos, P., 2000. The 5d level positions of the trivalent lanthanides in inorganic compounds, *J. Luminescence*, **91**, 155–176.

[55] Melcher, C. L., 2005. Perspectives on the future development of new scintillators, *Nucl. Instrum. Methods Phys. Res. A* **537**, 6-14.

[56] Cherepy, N. J., Payne, S. A., Asztalos, S. J., Hull, G., Kuntz, J. D., Niedermayr, T., Pimputkar, S., Roberts, J. J., Sanner, R. D., Tillotson, T. M., et al., 2009. Scintillators with potential to supersede lanthanum bromide, *IEEE Trans. Nucl. Sci*. **56,** 3.

[57] Kucera, M., Onderisinova, Z., Bok, J., Hanus, M., Schauer, P., and Nikl, M., 2016. Scintillation response of Ce^{3+} doped GdGa-LuAG multicomponent garnet films under e-beam excitation, *J. Lumines.* **169**, 674-677.

[58] Bohacek, P., Krasnikov, A., Kucera, M., Nikl, M., Zazubovich, S., 2019. Defects creation in the undoped $Gd_3(Ga,Al)_5O_{12}$ single crystals and Ce^{3+} doped $Gd_3(Ga,Al)_5O_{12}$ single crystals and epitaxial films under irradiation in the Gd^{3+} - related absorption bands, *Opticals Mater*. **88**, 601-605.

[59] Meng, F., Koschan, M., Melcher, C. L., and Cohen, P., 2015. Sintered pellets: a simple and cost effective method to predict the performance of GGAG:Ce single crystals, *Mat. Science Eng. B* **193**, 2026.

[60] Rawat, S., Tyagi, M., Netrakanti, P. K., Kashyap, V. K. S., A. Mitra, Singh, A. K., Desai, D. G., Kumar, G. A., and Gadkari, S. C., 2016. Pulse shape discrimination properties of

$Gd_3Ga_3Al_2O_{12}$:Ce single crystal in comparison with CsI:Tl, *Nucl. Instrum. Methods Phys. Res. Sect. A* **840**, 186-191.

[61] Tyagi, M., Meng, F., Koschan, M., Donnald, S. B., Rothfuss, H., Melcher, and C. L., 2013. Effect of cooping on scintillation and optical properties of a Ce-doped $Gd_3Ga_3Al_2O_{12}$ scintillator. *J. Phys. D: Appl. Phys.* **46**, 475302.

[62] Kamada, K., Yanagida, T., Endo, T., Tsutumi, K., Usuki, Y., Nikl, M., Fujimoto, Y., Fukabori, A., and Yoshikawa, A., 2012. 2 inch diameter single crystal growth and scintillation properties of Ce:$Gd_3Al_2Ga_3O_{12}$, *J. Cryst. Growth* **352**, 88–90.

[63] Kamada, K., Nikl, M., Kurosawa, S., Beitlerova, A., Nagura, A., Shoji, Y., Pejchal, J., Ohashi, Y., Yokota, Y., and Yoshikawa, A., 2014. Alkali earth co-doping effects on luminescence and scintillation properties of Ce doped $Gd_3Al_2Ga_3O_{12}$ scintillator, *Optical Materials* 36, 1942.

[64] Donnald, S. B., Tyagi, M., Rothfuss, H., Meng, F., Hayward, J. P., Koschan, M., and Melcher, C. L., 2013. The effect of B^{3+} and Ca^{2+} co-doping on factors which affect the energy resolution of $Gd_3Ga_3Al_2O_{12}$:Ce, *IEEE Trans. Nucl. Sci.* **60**, 4002.

[65] Bohacek, P., Krasnikov, A., Kucera, M., Nikl, M., Zazubovich, S., 2019. Defects creation in the undoped $Gd_3(Ga,Al)_5O_{12}$ single crystals and Ce^{3+} - doped $Gd_3(Ga,Al)_5O_{12}$ single crystals and epitaxial films under irradiation in the Gd^{3+} - related absorption bands, *Opticals Mater.* **88**, 601-605.

[66] Stanek, C. et al., 2007. The effect of intrinsic defects on $Re_3Al_5O_{12}$ garnet scintillator performance. *Nucl. Instrum. Methods Phys. Res. Sect. A* **579**, 27–30.

[67] Ovechkina, L., Riley, K., Miller, S., Bell, Z., and Nagarkar, V., 2009. Gadolinium loaded plastic scintillators for high efficiency neutron detection, *Phys. Proc.* **2**, 161.

[68] Nakhostin, M., 2012. Recursive algorithms for digital implementation of neutron/gamma discrimination in liquid scintillation detectors, *Nucl. Instrum. Methods Phys. Res. Sect. A* **672**, 1-5, 10.1016/j.nima.2011.12.113

[69] Aspinall, M. D., D'Mellow, B., Mackin, R. O., Joyce, M. J., Hawkes, N. P., Thomas, D. J., Jarrah, Z., Peyton, A. J., Nolan, P. J., and Boston, A. J., 2007. Verification of the digital discrimination of neutrons and γ rays using pulse gradient analysis by digital measurement of time of flight, *Nucl. Instrum. Methods Phys. Res. Sect. A* **583**, 432-438.

[70] Ronchi, E., Soderstorm, P., Nyberg, J., Snden, S. A., Conroy, S., Ericsson, G., Hellesen, C., GatuJohnson, M., and Weiszflog, M., 2009. An investigation of the digital discrimination of

neutrons and γ rays with organic scintillation detectors using an artificial neural network, *Nucl. Instrum. Methods Phys. Res. Sect. A* **607**, 620-628.

[71] Chandhran, P., Holbert, K. E., Johnson, E. B., Whitney, C., Vogel, S. M., 2016. Neutron and gamma ray discrimination for CLYC using normalized cross correlation analysis. In: 2014 IEEE Nucl. Sci. Symp. Med. Imaging Conf. NSS/MIC 2014.

[72] Alharbi, T., 2016. Principal Component Analysis for pulse-shape discrimination of scintillation radiation detectors, *Nucl. Instrum. Methods Phys. Res. Sect. A* **806**, 240-243.

[73] Fu, C., Di Fulvio, A., Clarke, S. D., Wentzloff, D., Pozzi, S. A., and Kim, H. S., 2018. Artificial neural network algorithms for pulse shape discrimination and recovery of piled-up pulses in organic scintillators, *Annals of Nuclear Energy* **120**, 410–421.

[74] Zaitsevaa, N., Glenna, A., Carmana, L., Martineza, H. P., Hatarika, R., Klapperb, H., and Paynea, S., 2015. Scintillation properties of solution-grown trans-stilbene single crystals, *Nucl. Instrum. Methods Phys. Res. Sect. A* **789**, 8-15.

[75] Wright, G. T., 1956. *Proceedings of the Physical Society: Section B* **69**, 358.

[76] Owen, R. B., 1958. *IRE Transactions on Nuclear Science* **NS5**, 198.

[77] Winyard, R. A., Lutkin, J., and McBeth, G. W., 1971. Pulse shape discrimination in inorganic and organic scintillators, *Nucl. Instrum. Methods* **95**, 141-153.

[78] Yanagida, T., Watanabe, K., Okada, G., and Kawaguch, N., 2019. Neutron and gamma-ray pulse shape discrimination of $LiAlO_2$ and $LiGaO_2$ crystals, *Nucl. Instrum. Methods Phys. Res. Sect. A* **919**, 64-67.

[79] Kudin, A. M., Sysoeva, E. P., Sysoeva, E. V., Trefilova, L. N., and Zosim, D. I., 2005. Factors which define the α/γ ratio in CsI:Tl, *Nucl. Instrum. Methods Phys. Res. Sect. A* **537**, 105.

[80] Langenbrunner, J. L., Morris, C. L., and Whitton, R. M., 1992. CsI-phoswich detector for charged-particle identification, *Nucl. Instrum. Methods Phys. Res. Sect. A* **316**, 450-451.

[81] Tamagawa, Y., Inukai, Y., Ogawa, I., and Kobayashi, M., 2015. Alpha–gamma pulse-shape discrimination in $Gd_3Al_2Ga_3O_{12}$ (GAGG):Ce^{3+} crystal scintillator using shape indicator, *Nucl. Instrum. Methods Phys. Res. Sect. A* **795**, 192.

[82] White, T. L., and Miller, W. H., 1999. A triple-crystal phoswich detector with digital pulse shape discrimination for alpha/beta/gamma spectroscopy, *Nucl. Instrum. Meth. Phys. Res. A* **422**, 144.

[83] Costa, E., Massaro, E., and Piro, L., 1986. A BGO-CsI(Tl) phoswich: A new detector for X- and γ-ray astronomy, *Nucl. Instrum. Methods Phys. Res., Sect. A* **243**, 572–577.

[84] Preziosi, E., Pani, R., Trigila, C., Polito, C., Bettiol, M., Borrazzo, C., Cinti, M. N., Fabbri, A., Pellegrinie, R., and Panig, R., 2016. A crystal identification method for monolithic phoswich detectors based on scintillation light distribution, *J. Inst.* **11**, P12009.

[85] Pradhan, M. K., Mukherjee, A., Basu, P., Goswami, A., Kshetri, R., Roy, S., Chowdhury, P. R., Sarkar, M. S., Palit, R., Parkar, V. V., Santra, S., and Ray, M., 2011. Fusion of ^{6}Li with ^{159}Tb at near-barrier energies, *Physical Review C* **83**, 064606.

[86] Selvakumar K., Singh A. K., Das S., Singh, P., Naq, S., Gowsami, A., Raut, R., Mukherjee, A., Pramanik, U. D., Dutta, P., Roy, S., Gangopadhyay, P.,…., Reddy T., 2013, Shape evolution in ^{123}Cs and ^{124}Ba nuclei, *Physical Review C* **84**, 024213.

[87] Sinha M., Majumdar, H., Bhattacharya, R., Basu, P., Roy, S., Biswas, M., Palit, R., Mazumdar, I., Joshi, P. K., Jain, H. C., and Kailas, S., 2007. Experimental investigation of fusion of ^{7}Li + ^{28}Si above the Coulomb barrier, *Physical Review C* **76**, 027603.

[88] Kim, S., Kim, H. J., Park, H., Kang, H., Lee, S. H., and Doh, S., 2014. Thermoluminescence Properties of a $CeBr_3$ Single Crystal, *J. Nucl. Science Tech.* **55**, 1228-1231.

[89] Joshi D. A., Nigam A. K., Dhar S. K., and Thamizhavel A., 2010. Magnetocrystalline anisotropy in RAu_2Ge_2 (R = La, Ce and Pr) single crystals, *Journal of Magnetism and Magnetic Materials* **322**, 3363-3371.

[90] Moorthy Babu S., Kitamura K., Takekawa S., 2005. Stoichiometry and doping induced modifications in the properties of $Bi_{12}SiO_{20}$ single crystals, *J. Cryst. Growth* **275**, 681-686.

[91] Rawat, S., Tyagi, M., G. Anil Kumar, Gadkari, S. C., 2018. Efficiency studies on $Gd_3Ga_3Al_2O_{12}$:Ce scintillators: Simulations and measurements, *IEEE Trans. Nucl. Sci.*, **65**, 2109-2113.

[92] Debertin, K., and Helmer, R. G., 1988. Gamma and X-ray spectrometry with semiconductor detectors, Elsevier Science, North Holland, Amsterdam.

[93] Abbas, M. I., 2001. Analytical formulae for well-type NaI(Tl) and HPGe detectors efficiency computation, *Applied Radiation and Isotopes* **55**, 245–252.

[94] Rawat, S., Tyagi, M., G. Anil Kumar, Gadkari, S. C. and Kim, H. J., 2019. Studies on effect of co-doping on PSD properties of GGAG:Ce scintillators, *IEEE Trans. on Nucl. Sci.*, 2019 [Revised manuscript under review].

[95] Rawat, S., Tyagi, M., G. Anil Kumar, Gadkari, S. C., 2019. A novel versatile phoswich detector consisting of two single crystals to discriminate various kinds of radiation, *Rev. Sci. Instrum.*, 2019 [Revised manuscript under review].

CHAPTER 2

Experimental techniques

The experimental techniques used in the thesis work have been introduced in this chapter. Description of Bridgeman and Czochralski techniques along with the structural and optical characterization techniques has been given. The growth and characterization of a large size GGAG:Ce,B single crystal is also discussed. The schematic setups for performing PSD studies using digitizer and zero crossover have been shown. The corresponding equations used for fitting and calculating average decay time, relative ratio, FOM and PSD are also given.

2.1 Single crystal growth techniques

The single crystals have advantage due to their linear behaviour of the emission with the deposited energy which leads them to be used in spectrometry mode as well as for identification of the radionuclide. Single crystals can be grown from melt, solution or vapour. Growth from the melt is most effective and widely used technique for device grade single crystals such as Si and Ge.
The growth from melt can be carried out by the following techniques [1]:

- Czochralski ("pulling")
- Bridgman ("directional solidification")
- Kyropoulos ("top seeding")
- Laser-heated pedestal growth
- Verneuil ("flame fusion")
- Micro pulling
- Floating Zone (including image furnace)

Out of all the above mentioned techniques, the Bridgman and Czochralski are the dominant techniques for bulk size single crystal growth and has been discussed in the following sections.

2.1.1 Bridgman technique

This technique of single crystal growth from melt was developed in 1925 by Percy Williams Bridgman [2]. This technique produces crystals with high dimensional tolerance, technology employed is simple and crystal growth is fast. The materials which melt congruently, do not decompose before melting and do not transform phase from melting point to room temperature are grown as single crystals through this technique. The material whose single crystal is to be grown is loaded in a quartz tube and encapsulated. The quartz tube is suspended in the Bridgman furnace (see Figure 2.1) having a known growth gradient. The tip of the quartz ampoule is shaped conical to enhance the nucleation process of a single crystal. When full melting of the materials is achieved, the ampule is made to pass through a cold zone gradually.

The capillary tip in the lower conical part of ampoule is filled with melt where seed growth initiates with gradual lowering. The seed grows up to an entire crystal from the melt. The rate of lowering of the ampule regulates the quality of the crystal and it varies with different materials.

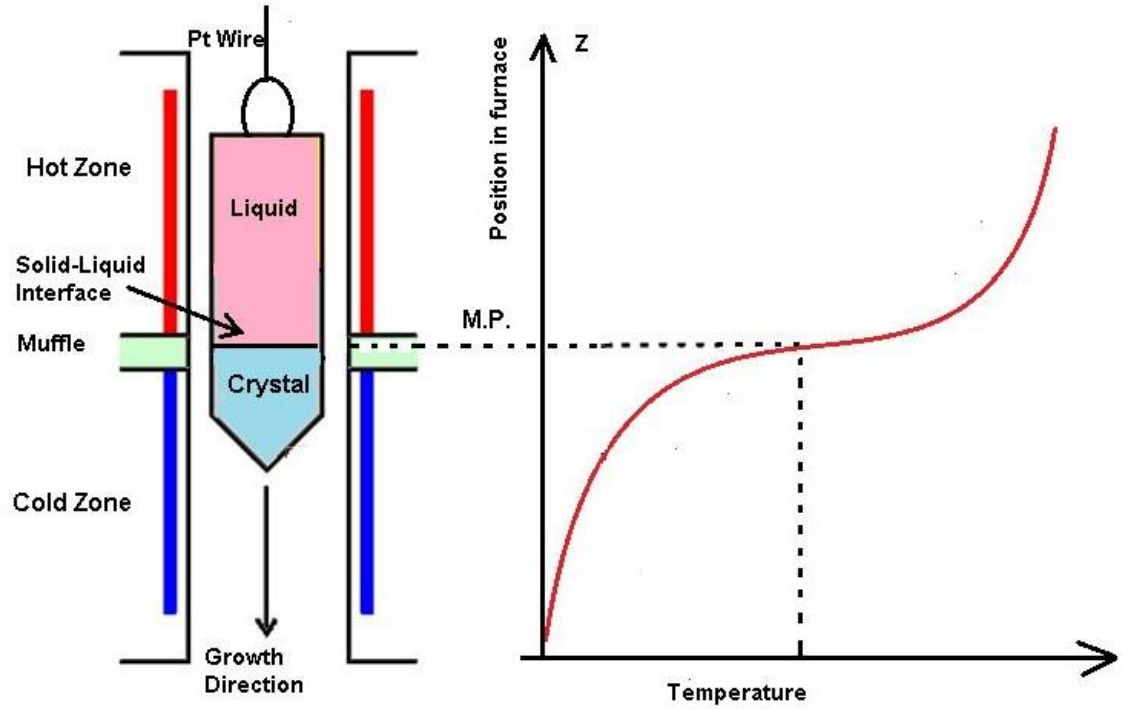

Figure 2.1 Schematic of Bridgman technique [3].

2.1.2 Czochralski technique

The Czochralski technique derives its name from Jan Czochralski, a Polish scientist, who first utilized this technique to grow metal single crystals [4]. The whole semiconductor industry has evolved due to the high quality silicon grown using this technique. Like Bridgman technique, this method also has congruent melting point as a prerequisite. The advantage of this technique is the growth of high quality large size crystals with better control over many parameters such as nucleation, dimension and growth rate [1]. The disadvantages of this growth technique includes strain in the grown crystals, evaporation of the constituting materials and contamination due to crucible material in the crystal. The crucible containing material charge is placed between the heating coils in the growth station. The heat losses due to conduction and convection are taken care by properly insulating the crucible with wool, ceramic plates and cylindrical tube. The melting of the charge is done by RF heating coils. After achieving the melting and thermalization, the seed attached to a lowering rod made of alumina is made to touch the top of the melt in the crucible. The seed is maintained in contact with the melt for thermalization. Once the dynamic equilibrium is achieved, melt starts growing and crystalizing around the seed. The single nucleation is important for perfect crystallinity which is controlled by adjusting the power of the heater. Depending on the thermal conductivity, the seed rod is pulled upward at a very slow rate. Continuous rotation of the

growing crystal is maintained throughout the whole process which in turn ensures proper heat flow for maintaining solid-melt interface. The schematic of a Czochralski technique is shown in Figure 2.2.

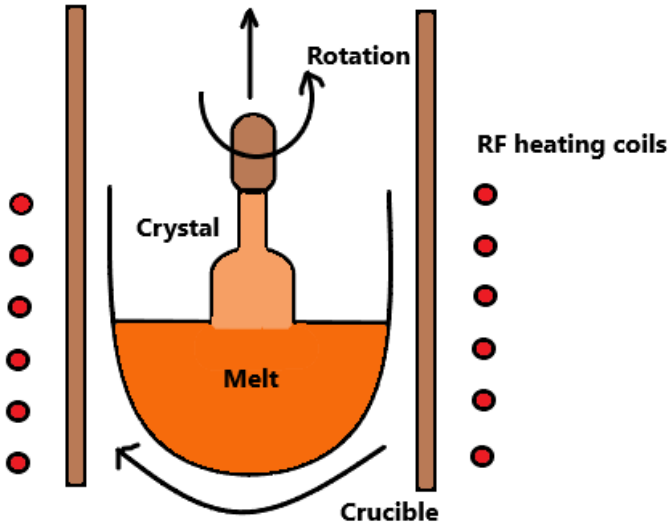

Figure 2.2 Schematic of a Czochralski furnace.

Ce doped GGAG has been proven to be a promising scintillating material due to many properties as discussed in Chapter 1. The growth of this material in single crystalline form has improved scintillation properties with the proper selection of co-dopant, growth ambience and after growth treatments [5]. Various devices for different applications have also been developed using these crystals. However, the application of this crystal in high energy physics experiments requires the scaling up the size of grown crystals without deteriorating its scintillation performance characteristics. The growth of single crystals having large diameters face numerous growth challenges like optimization of radial and axial temperature gradient, core formation, segregation of dopant, cracking etc. We have performed and discussed in detail the successful growth of large size GGAG:Ce,B single crystals using the Czochralski technique [7].

Experimental details

The experimental work has been carried out in Bhabha Atomic Research Centre, Mumbai. The initial material for the growth was synthesized by mixing the constituent oxides Gd_2O_3, Ga_2O_3, Al_2O_3, CeO_2 and H_3BO_3 in their respective molar ratio. The total material weighing 1500 gm was mixed well and cold pressed uniaxially to make pellets of 50 mm diameter. These pellets were loaded in an Iridium crucible having dimensions of 80 mm diameter and 60 mm length. The material

was melted at 2000^{o}C and topped up again with the rest of pellets. The crystal growth experiments were carried out in a Cyberstar crystal puller (see Figure 2.3) based on the Czchrolaski technique. The diameter was controlled automatically based on the feedback signal from the difference of desired weight grown per hour and the measured growth rate. The growth parameters were optimized based on the previous growth of smaller size crystals. The grown crystal was cut to make a cylinder having dimension of 45 mm diameter and 50 mm length.

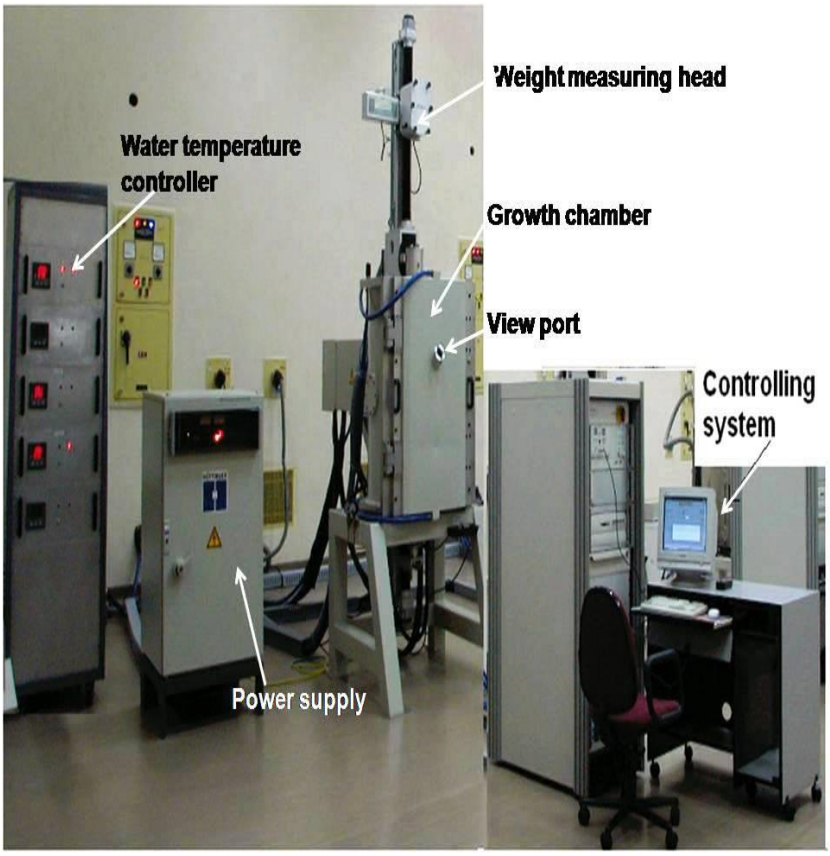

Figure 2.3 Crystal puller system [Cyberstar make Oxypuller] [6].

Results and discussion

Table 2.1 shows the optimized parameters used for the crystal growth after some failure attempts [7]. Initially, due to higher density (~ 6.7 gm^{3}), the loaded material was not sufficient to provide the appropriate melt height for the required thermal gradient. Therefore, large quantity of initial material was used in the form of pressed pellets. The polycrystalline material was melted and reloaded again after the cooling. The process was repeated and total 1.5 kg material was loaded. However, to avoid any stoichiometric deviation, the initial material was also prepared in multiple batches accordingly. A non-oriented GGAG seed with Iridium seed holder was used to grow the

single crystal. In initial growth attempts, seed got melted during the optimization of power and the crystal could be grown from the seed holder.

Table 2.1 The optimized growth parameters used for the single crystal growth of GGAG:Ce,B.

Parameters	Optimized Values
Melting Temperature	1850°C
Pull Rate (Seed)	2 mm/hr
Pull Rate (Cylinder)	2 mm/hr
Rotation rate	15 rpm
Initial chamber pressure	1×10^{-5} mbar
Ar gas pressure	1100 mbar
Temperature gradient	40°C/cm
Cooling rate	70°C/cm

The grown crystal as shown in Figure 2.4 (a) was found to have multiple cracks with poorly controlled diameter. A seed was cut perpendicular to the growth axis and used in next growth run. A good quality single crystal having only couple of cracks in the lower region was grown in the next attempt as shown in Figure 2.4 (b). The poor quality in the lower region can be assigned to the deviation from stoichiometry due to different evaporative losses of constitute oxides [7]. The diameter control was found to be improved significantly after the optimization of growth parameters. The solid melt interface was found to be nearly flat. The total weight of the grown crystal was found to be 550 gm [7]. More crystal growth experiments are in progress to improve the quality of crystal.

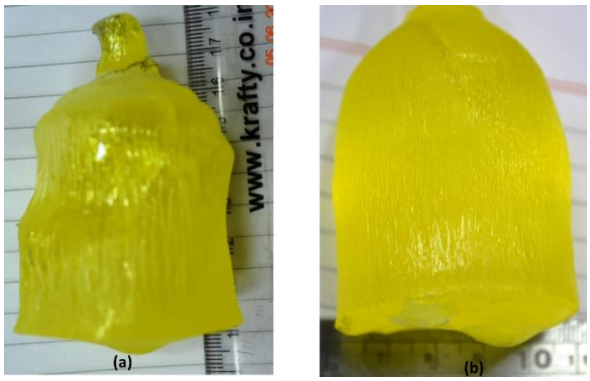

Figure 2.4 Photographs of the grown crystals **(a)** Initial attempt **(b)** After optimizing the growth parameters [7].

2.2 X-ray diffraction

X-ray diffraction is a powerful, convenient and non-destructive analytical technique for investigating the structure of the materials. It primarily gives information about the crystallinity, phase, orientation, lattice parameters, strain, defects and other structural characteristics of the crystal [8]. With the advancement of the technique, all the branches of science and technology are now making use of this technique. The fundamental research ranges from the structure of matter to the quality control of commercial products. X-rays are produced when high-energy radiation interact with the matter. In this process, electrons are ejected from the inner core shell surrounding the nucleus and the vacancy is filled with another electron of higher energy from the outer shells. These electrons give up their excess energy in the form of characteristic X-rays. If the vacancies are filled by L-shell electrons then the emitted photons are referred to as K_α radiation. These X-ray photons have wavelengths in angstrom which is similar to the inter planar spacing in atoms. The planes in a crystal can be considered as reflecting. When a beam of X-ray is incident on a single crystal which is a periodic arrangement of atoms, it undergoes constructive interference with the lattice planes (see Figure 2.5).

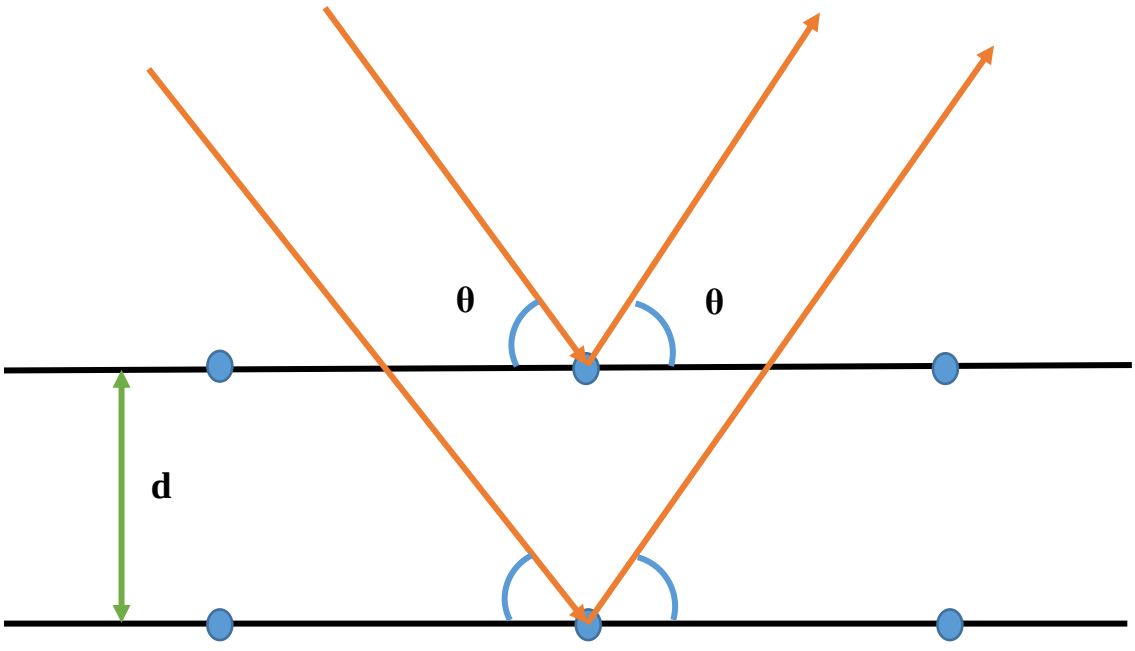

Figure 2.5 Bragg's X-ray diffraction law.

Following equation is known as the Bragg's equation:

$$2d \sin\theta = n\lambda \quad (2.1)$$

where, d is the inter planar spacing, λ is the wavelength of incident X-rays and θ is the angle of diffraction.

The diffracted beam intensity depends on the arrangement and distribution of atoms in a crystal lattice [9]. Thus, X-ray pattern is a fingerprint of the material to a given phase. The database containing XRD patterns of all the materials is maintained which can be used to match with the XRD of the sample in order to know its phase and structure.

2.2.1 Powder X-ray diffraction

The powder X-ray diffraction technique is based on the principle that in a polycrystalline there are sufficient crystallites with nearly all possible orientations and the X-ray reflections corresponding to all these possible crystal lattice planes can be plotted [10]. The recorded XRD pattern has enough reflections which are utilized to accurately determine the phase of the sample. The schematic of powder X-ray diffraction is shown in Figure 2.6.

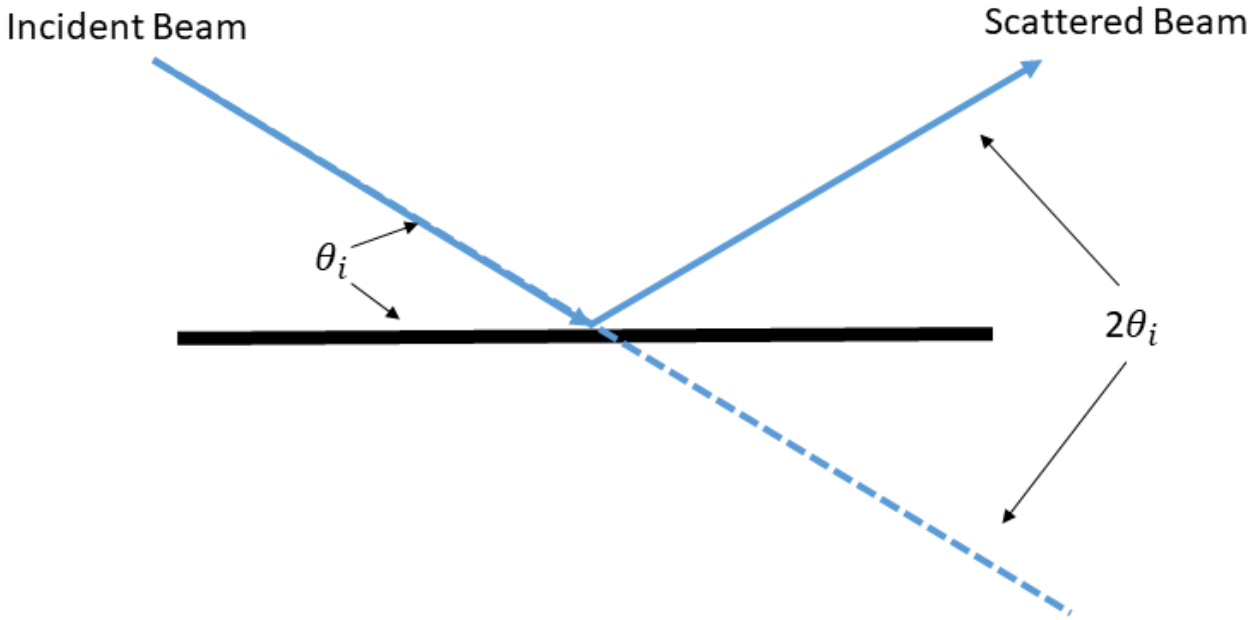

Figure 2.6 Schematic of powder X-ray diffractometer [6].

2.2.2 Laue reflection

Laue's reflection (see Figure 2.7) is a single crystal X-ray diffraction technique which can determine the whole crystal structure, space group, location of atoms, atom bonds and their location, bond angles, chemical composition of crystal without any data base.

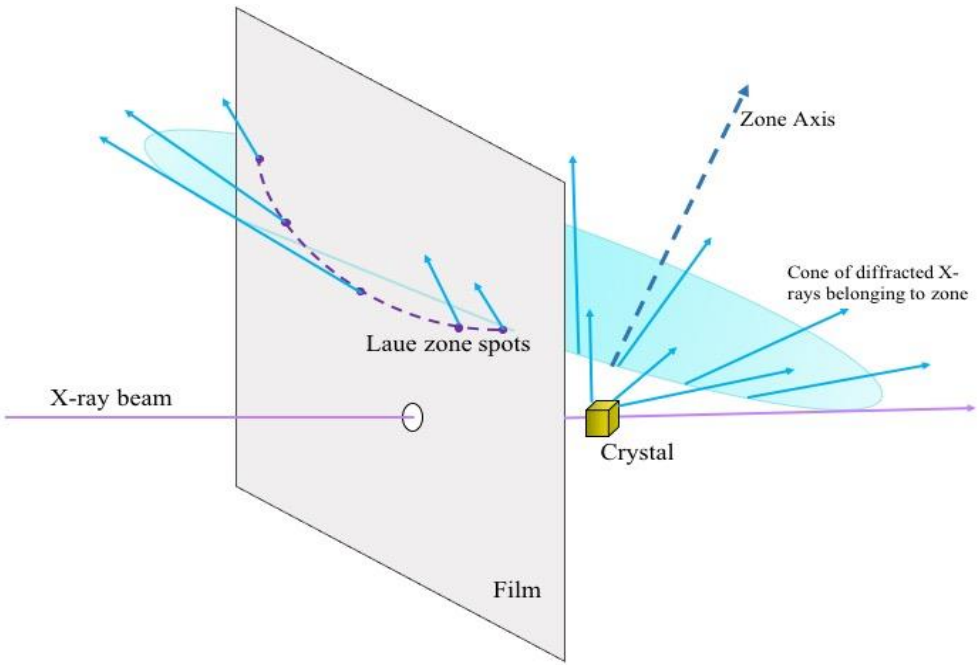

Figure 2.7 Schematic of a Lau reflection setup [6].

In this method, for every set of planes Bragg angle is fixed and each set of planes diffracts a characteristic wavelength of light which satisfies Bragg's law for fixed values of d and θ. Every point corresponds to a particular set of planes. The reflections produce a unique pattern for a fixed orientation which is used to identify the crystal structure [11].

The Laue reflection pattern of the above mentioned large size GGAG:Ce, B grown crystal having dimensions of 45 mm diameter and 50 mm length was recorded to characterize the crystalline quality [7]. The pattern was found to be identical at different position along a plane as shown in Figure 2.8. It confirms the crystallinity and a single phase of the grown crystal.

2.3 UV-VIS spectrophotometer

Transmission/absorption measurements are carried out using a UV-VIS spectrophotometer which measures the intensity of transmitted/absorbed light through a sample w.r.t a reference sample, usually air or vacuum. Transmission/absorption spectrometry gives information about the absorption levels created by dopants and impurities in the sample [12]. The transmittance is usually

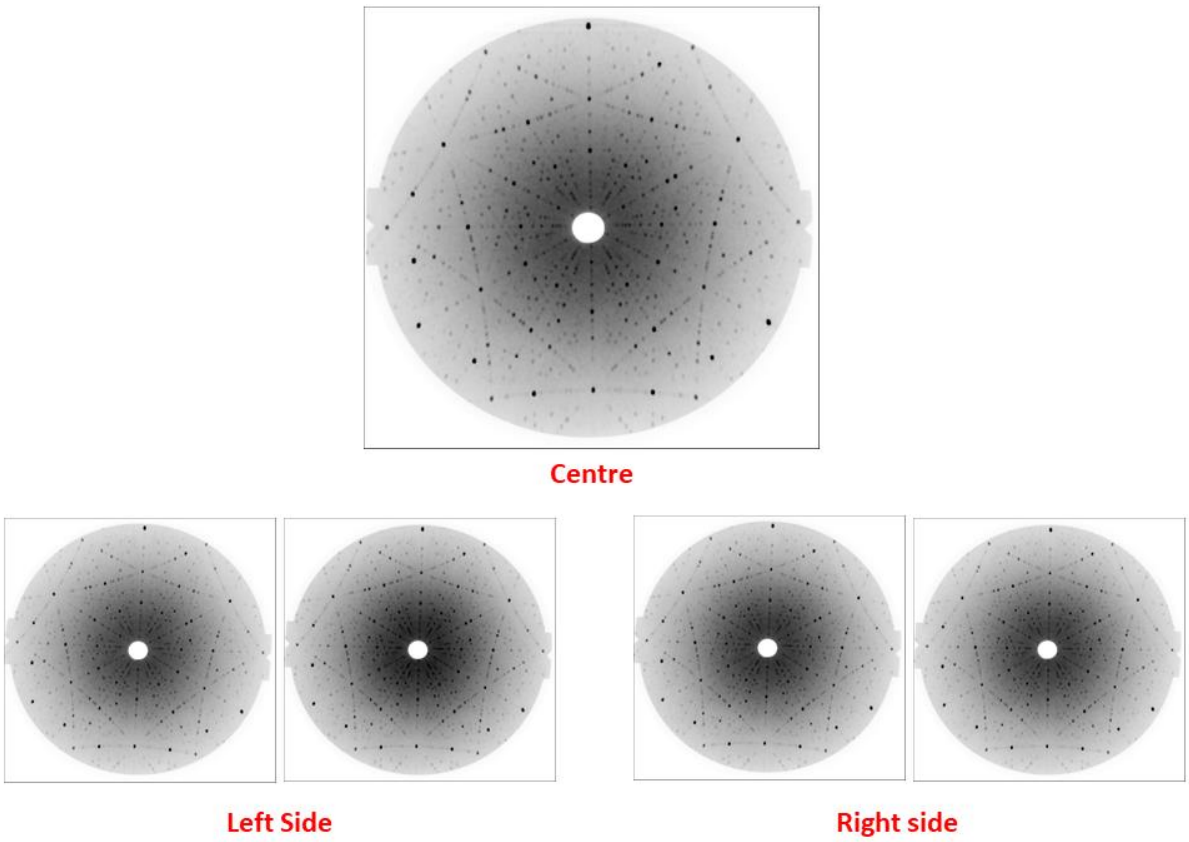

Figure 2.8 Laue reflection pattern from all sides measured with GGAG single crystal [7].

expressed in percentage (%T) and is defined as the ratio of the intensity of light transmitting through a sample (I) to the intensity of light before passing the sample (I_o). The absorbance is the related to the transmittance in the following way:

$$A = -\log\left(\%T/_{100}\right) \tag{2.2}$$

In double beam UV-VIS spectrophotometer (see Figure 2.9), the light is split into 2 beams before it reaches the sample. One acts as a reference beam and other passes through the sample.

2.4 Photoluminescence spectrometer

Luminescence can be classified as photoluminescence, radio-luminescence thermoluminescence and so on, depending on the excitation mechanism [13]. They help in understanding the scintillation mechanism by probing the emissions from the luminescent sites via de-excitation [14]. PL spectrophotometer comprises of a monochromator, sample containing chamber, emission monochromator, detectors and excitation source (Xe or H_2 filled lamps) for recording life times in μs and ns range respectively.

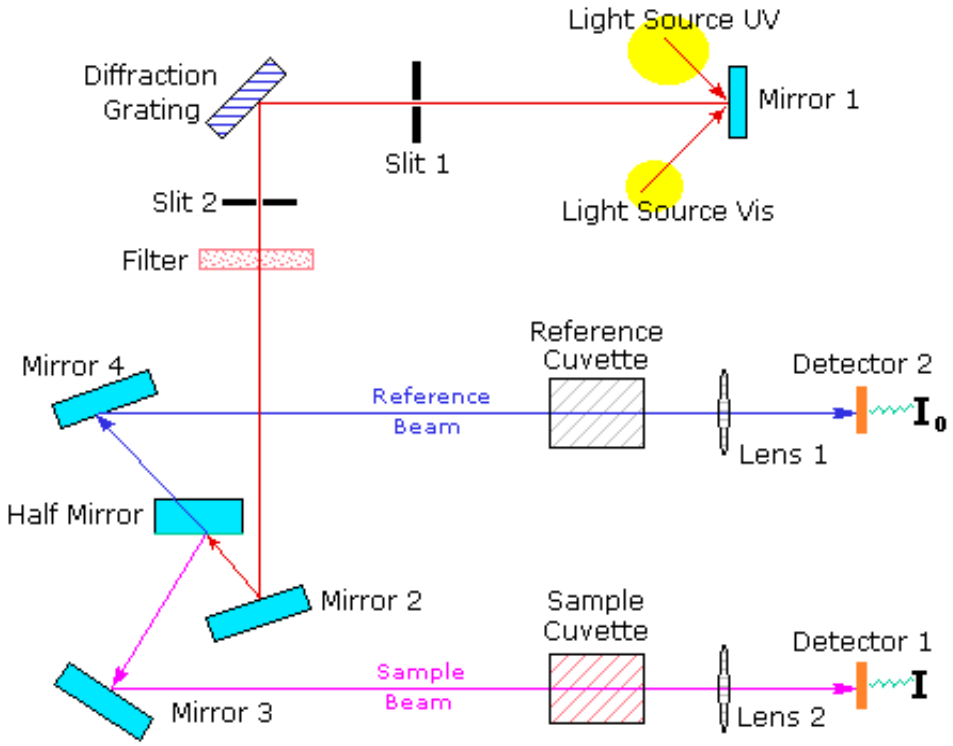

Figure 2.9 Schematic diagram of a UV-VIS-NIR spectrophotometer [6].

The broad spectrum produced by the lamp is imaged on the entrance of the excitation monochromator. Excitation wavelength of a particular bandwidth is selected by the monochromator and after passing through an iris is focused on the sample. Luminescence from the sample is collected through a lens system and then focused on the emission monochromator. The selected emission wavelength light by the emission monochromator is passed into a PMT or an InGaAs detector.

A small piece of the grown large size GGAG:Ce,B crystal was cut and used for the measurement of the emission and transmission properties using Edinburgh fluorescence [15] spectrometer model FLP 920 is shown in Figure 2.10. The photo-luminescence spectrum shown in Figure 2.11 depicts the characteristics transition of Ce^{3+} ions. The emission band around 550 nm lies in the transmission region of the crystal and therefore indicates the possibility of using larger size crystal for high energy radiation detection.

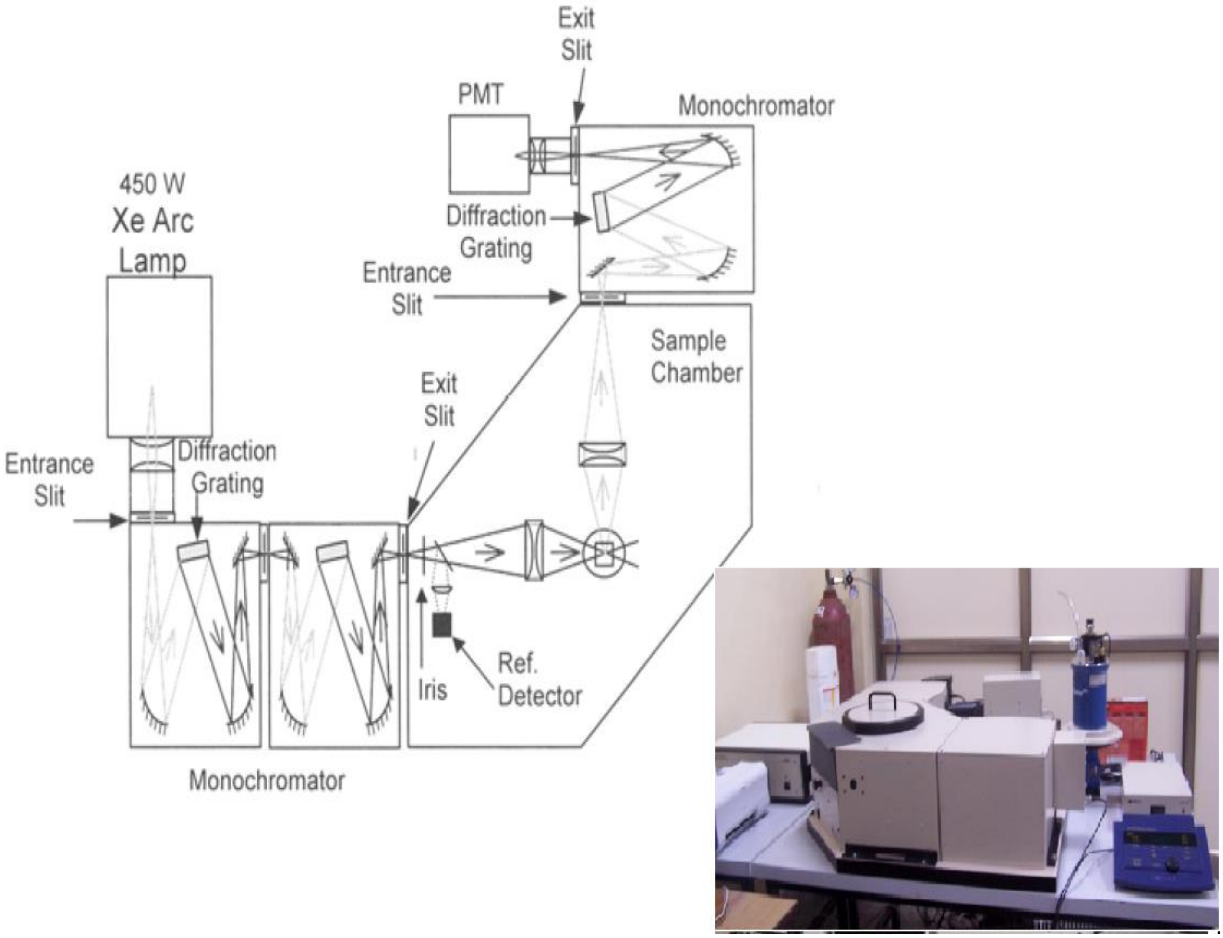

Figure 2.10 The schematic diagram of a fluorescence spectrometer FLP920 [6].

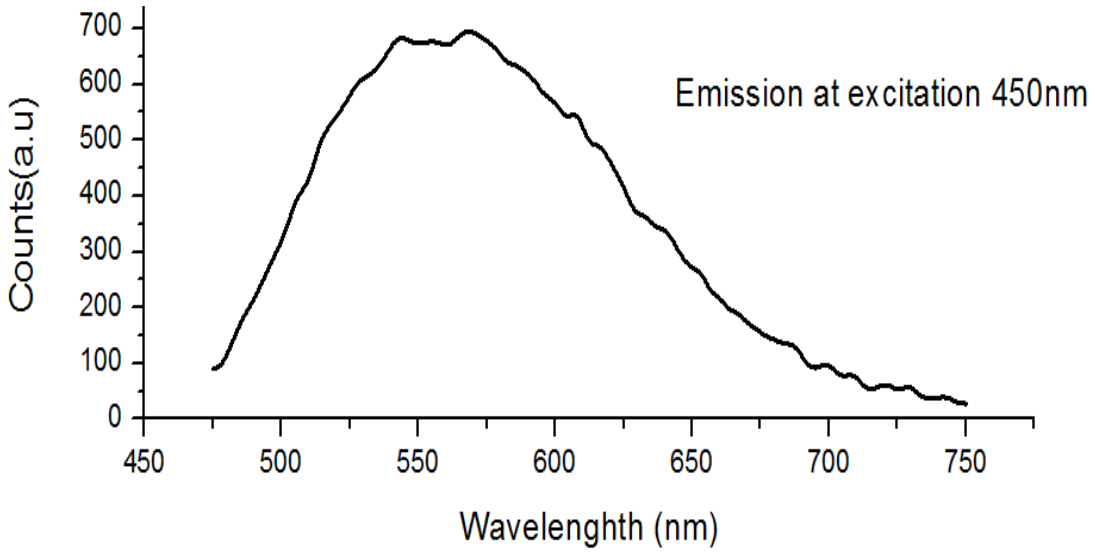

Figure 2.11 The photoluminescence spectrum of large size GGAG:Ce, B single crystal measured at 450 nm excitation [7].

2.5 X-ray stimulated luminescence (or) Radio luminescence

When luminescence is caused by exciting the sample with high energy radiation of X-rays, it is known as X-ray stimulated luminescence or radio-luminescence (RL). The high energy radiation leads to creation of charge carrier followed by their relaxation at the luminescent sites [16]. In RL, the electrons are excited deeply in conduction band due to high energy of X-rays compared to the visible light in PL. Also, the relaxation process is quite complex compared to PL where just band transitions take place. The RL instrument consists of a monochromator, and a white X-ray source.

2.6 Photo sensor

Photo sensor is used to measure visible photons from the scintillator crystal by converting these photons into photocurrent when they strike the light-sensitive surface. The magnitude of the photocurrent produced by the PMT is directly proportional to the intensity of photons striking the PMT surface [17]. With advancement in PMT technology, many photo sensors such as PMT, p-i-n photodiodes, avalanche photodiodes and SiPM have been developed. The studies concerning this thesis were performed using PMT and SiPM only, thus their working principles have been discussed in detail.

2.6.1 Photomultiplier tube (PMT)

The working principle of PMT is to convert scintillations of scintillator detector into an electric pulse to the order which can be processed by the counters and pulse height analysis related electronics. A PMT consists of two major parts: a photocathode and an electron multiplier unit (see Figure 2.12).

Photocathode converts incident scintillation photons into low energy photoelectrons depending on its quantum efficiency. If the scintillation photons from the scintillator are in the form of a pulse then the pulse from the produced photo electrons is also of same duration. The photoelectrons emitted from the photo cathode at this point are not sufficient to produce a measurable electric pulse. The coupled electron multiplier unit provides an efficient geometry for the collection of photoelectrons at the anode and at the same time multiplying their numbers. After the amplification of photoelectrons with the help of dynodes and with a gain of the order of 10^9 the current is sufficient for further processing [17].

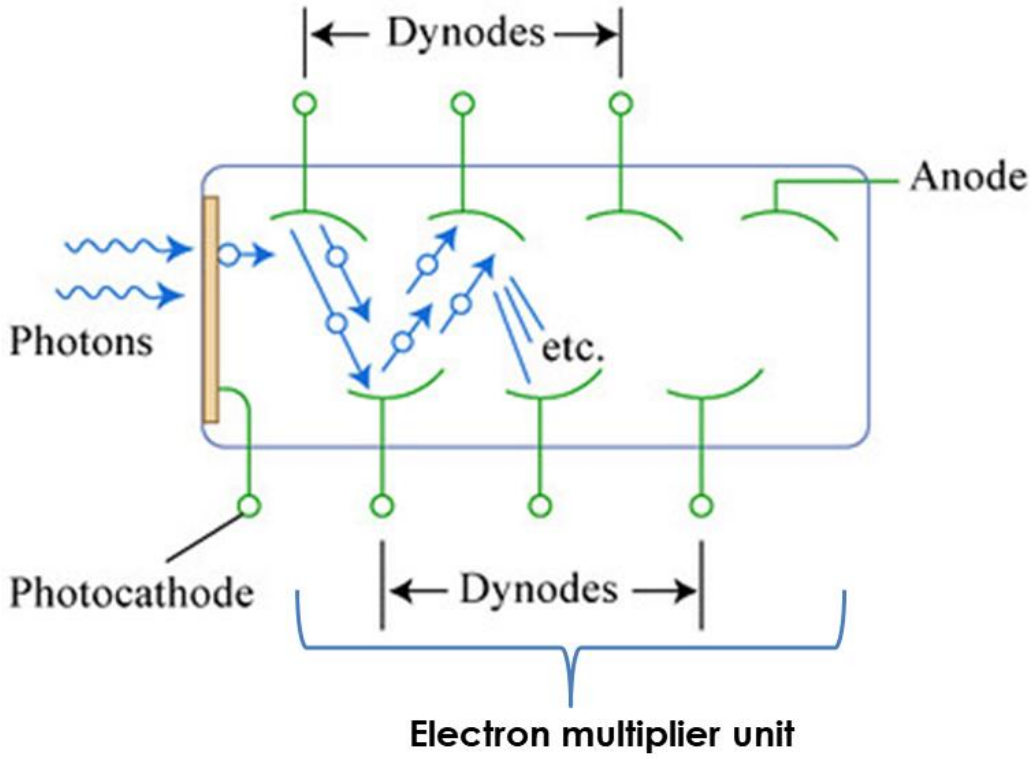

Figure 2.12 Schematic diagram of a PMT [18].

2.6.2 SiPM

It consists of an array of Geiger-mode avalanche photodiodes (GM-APD) as shown given in Figure 2.13. GM-APD operates in the Geiger mode when bias voltage is applied above the avalanche breakdown voltage and the avalanche process is stopped by decreasing the electric field by means of a quench resistor [19]. Its main purpose was to measure a single photon. However, dark currents, dead and recovery times permit only photodiode areas of ~100 μm [20]. Thus, SiPM is very small where photodiodes are divided into cells with an individual limiting resistor which are connected in parallel.

The working principle of SiPM is as follows [19]: a single photon from the scintillator produces an e-h pair in any one of the GM-APD microcells which initiates the avalanche process. The avalanche stops when the discharge of microcell to the breakdown voltage occurs. Then microcell recharges to the bias voltage. This discharge and recharge process produces a signal. All the signals from the array of microcells combine up to a multiple of the individual cell signal. The final signal from the array of GM-APDs of the SiPM is, thus, a function the incident photon intensity.

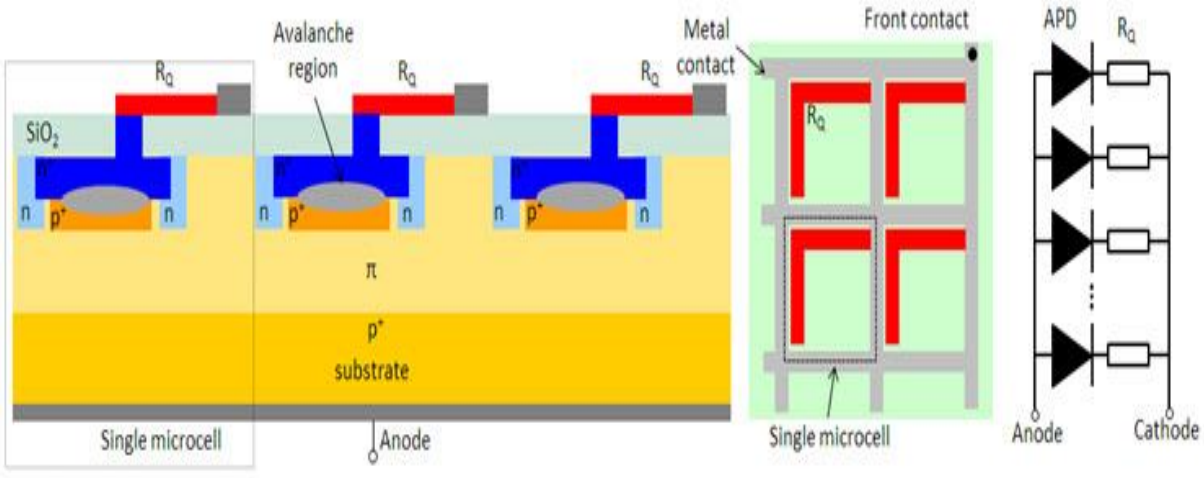

Figure 2.13 Schematic diagram of a SiPM by Hamamatsu [21].

The SiPM used in the PSD measurements, discussed in chapter 3, is shown in Figure 2.14.

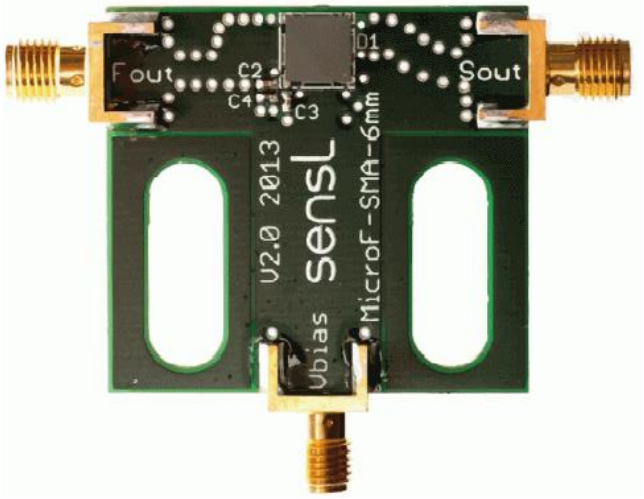

Figure 2.14 SiPM by sensL.

2.7 Scintillation detection

The grown large size GGAG:Ce,B crystal was cut to make a cylinder having dimension of 45 mm diameter and 50 mm length. The crystal was mounted on a 5 inch diameter PMT and covered with a reflecting spectralon hemisphere for initial scintillation characterizations. The crystal was coupled to an indigenously developed portable USB powered gamma spectrometer to characterize the high energy gamma radiation from an Am-Be source. The effect of Pb, borated rubber and Cd shields on the pulse height spectrum was also studied [7].

Figure 2.15 (a) shows the pulse height spectrum of the GGAG:Ce scintillator measured with ^{137}Cs source. The energy resolution is found to be about 14% which is very poor compared to the reported value of about 7% in literature [7]. This is due to the presence of some cracks. Figure 2.15 (b) shows the pulse height spectrum recorded with Am-Be radioactive source. The alpha emission from Am-241 interacts with ^{9}Be and produces ^{12}C in its first excited state. The ^{12}C emits 4.4 MeV gamma during its de-excitation. The photo-peak due to this high energy gamma can be observed in the spectrum given in Figure 2.15 (b) [7]. The grown crystals could detect 4.4 MeV gamma radiations from Am-Be source. However, due to the poor resolution the escape peak could not be resolved. The poor energy resolution even at such a high energy is mainly due to Doppler broadening arising from the fast de-excitation of carbon [22].

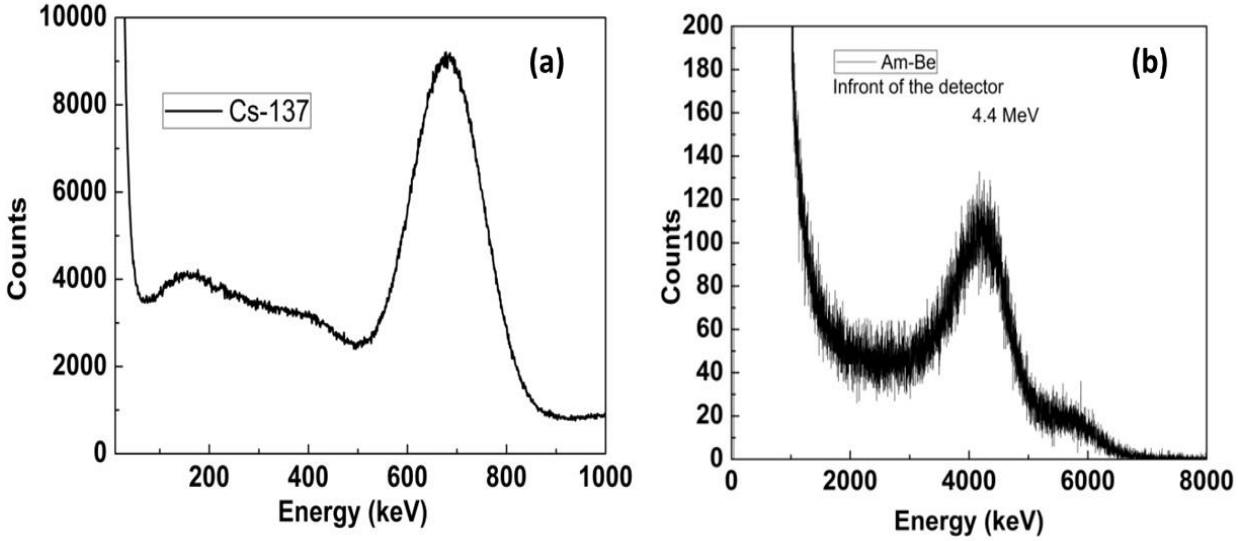

Figure 2.15 Pulse height spectrum measured with **(a)** Cs-137 source emitting 662 keV gamma, **(b)** With Am-Be source having 4.4 MeV gamma [7].

2.7.1 Decay time measurements

Fig. 2.16 shows a typical fitted decay time plot from an oscilloscope when an anode signal from the PMT is fed to it. A decay curve of scintillator consisting of two components usually is fitted using the following equation [23]:

$$I(t) = A_0 + A_1 \exp\left(-t/\tau_1\right) + A_2 exp\left(-t/\tau_2\right) \quad (2.3)$$

The relative ratio of decay components was calculated from the equation:

$$Q_1 = \frac{A_1\tau_1}{A_1\tau_1 + A_2\tau_2} \quad (2.4)$$

The average decay time was calculated using the equation:

$$\tau = \frac{A_1\tau_1 + A_2\tau_2}{A_1 + A_2} \tag{2.5}$$

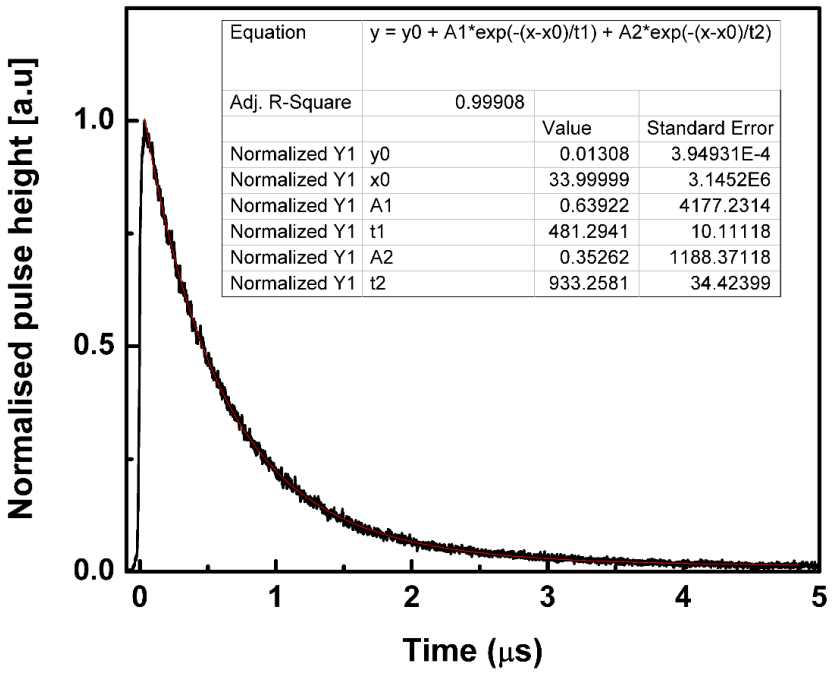

Figure 2.16 A fitted scintillation decay time curve.

The mean decay time was calculated using the equation:

$$\tau_{mean} = \frac{A_1\tau_1^2 + A_2\tau_2^2}{A_1\tau_1 + A_2\tau_2} \tag{2.6}$$

where, τ_1 and τ_2 denote the fast and slow decay time components respectively and A_1, A_2 denote their relative contributions in the total pulse intensity.

2.8 PSD techniques

In the mixed radiation field, different kinds of nuclear radiation are usually discriminated by two methods; pulse-height discrimination (PHD) or pulse-shape discrimination (PSD). The variations in the light yield for different kinds of radiation generate different pulse-heights in PHD method. On the other hand, some materials have more than one component of the scintillation decay whose ratio depends on the type of radiation. Therefore, these materials have the ability to discriminate different radiations based on the PSD method.

The figure of merit (FOM) describing the degree of discrimination between alpha and gamma pulses was calculated using the equation [24]:

$$FOM = \frac{\Delta T}{\tau_\alpha + \tau_\gamma} \tag{2.7}$$

where, ΔT is the separation between the centroids of two peaks in the TAC output spectrum (see Figure 2.17) or PSD values from the digitizer, while τ_α and τ_γ are the FWHM of time or PSD gaussian distributions.

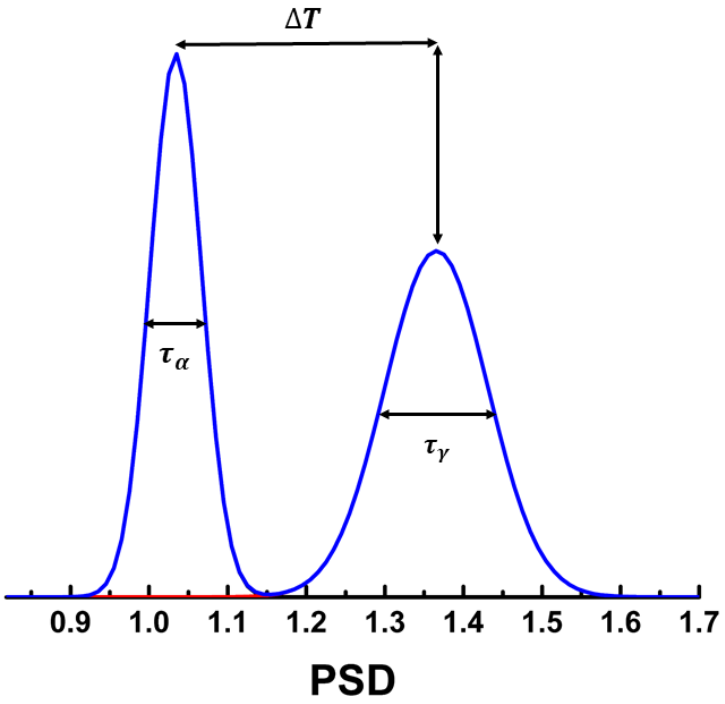

Figure 2.17 A PSD plot featuring FOM.

2.8.1 Charge Integration method

Figure 2.18 shows a typical exponential decay curve having more than one decay components. Short gate integrates charge due to fast component and long gate integrates total charge collected. Charge integration technique utilizes the relative ratio of these decays. Therefore, the integration of charges collected in two different time regions (called gate) can be used to discriminate different kinds of radiation. Different types of radiation can be discriminated by plotting the PSD values at different energies [25].

The discrimination can be represented as a dimensionless parameter $\boldsymbol{PSD_{Digitizer}}$ given by the following equation [24]:

$$PSD_{Digitizer} = 1 - \frac{Q_S}{Q_L} \quad (2.8)$$

where Q_S is the charge collected in the short gate due to prompt light emission while Q_L is the total light collected in the long gate.

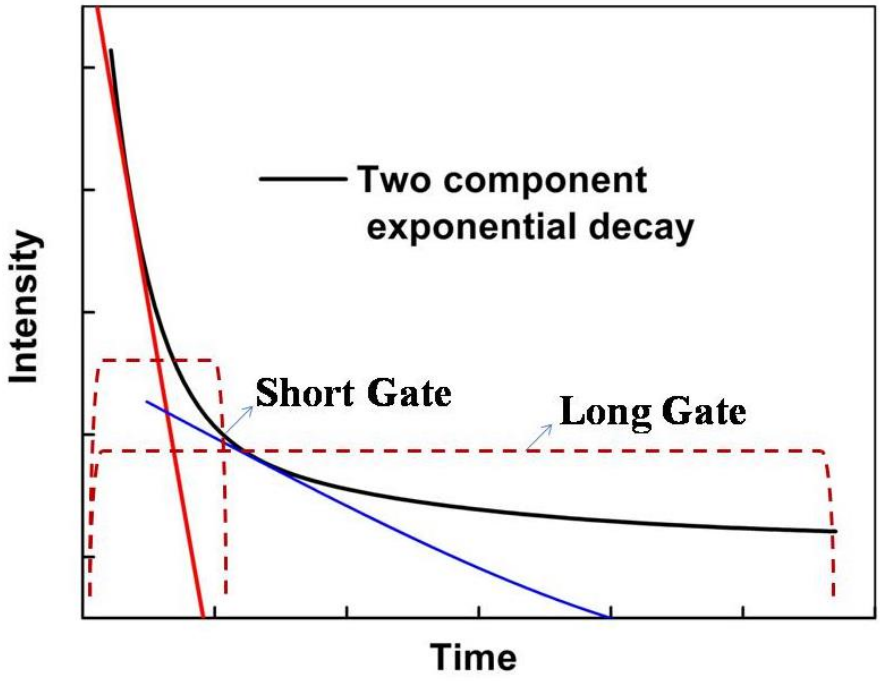

Figure 2.18 The schematics of a typical two exponential decay curve and the concept of PSD by integrating charges in two different time windows [25].

The schematic of PSD measurement setup employing the charge integration method using a digitizer as discussed in chapters 3, 5 and 6 has been shown in the following Figure 2.19.

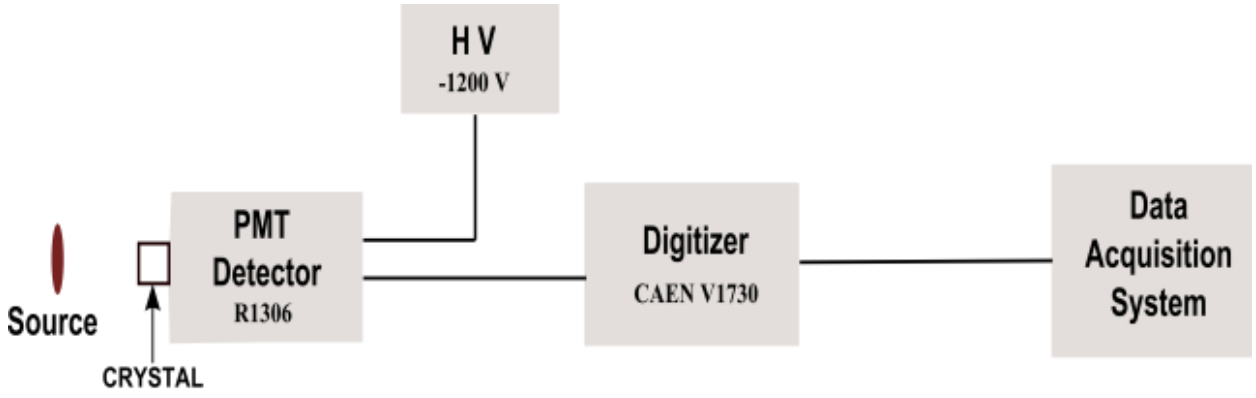

Figure 2.19 A block diagram of PSD measurement setup using digitizer [23].

2.8.2 Zero crossing method

The zero crossing technique is one of the most widely used methods for PSD which extracts the zero crossing time (ZCT) of the double differential bipolar pulses. A typical ZCT bipolar pulse is shown in the Figure 2.20.

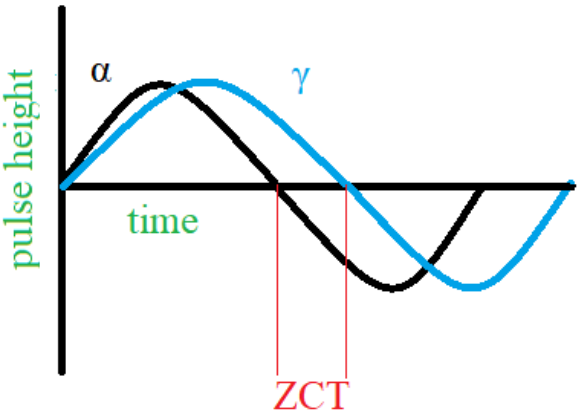

Figure 2.20 Pictorial representation of zero crossing time (ZCT).

Figure 2.21 shows a typical ZCT setup using PMT as photo-sensor. The detector pulses are processed through a spectroscopy amplifier. The unipolar pulses from the amplifier are fed to a CAEN make VME Analog to digital convertor (ADC V785) containing pulse height characteristics. Discrimination was achieved by measuring the ZCT of the amplified, bipolar pulse from the spectroscopy amplifier [23]. To exploit the discrimination in ZCT bipolar pulses, a constant fraction discriminator (CFD) is used. The zero crossing technique has been used in the present thesis work and discussed in chapter-3 for PSD of alpha particles and gamma rays.

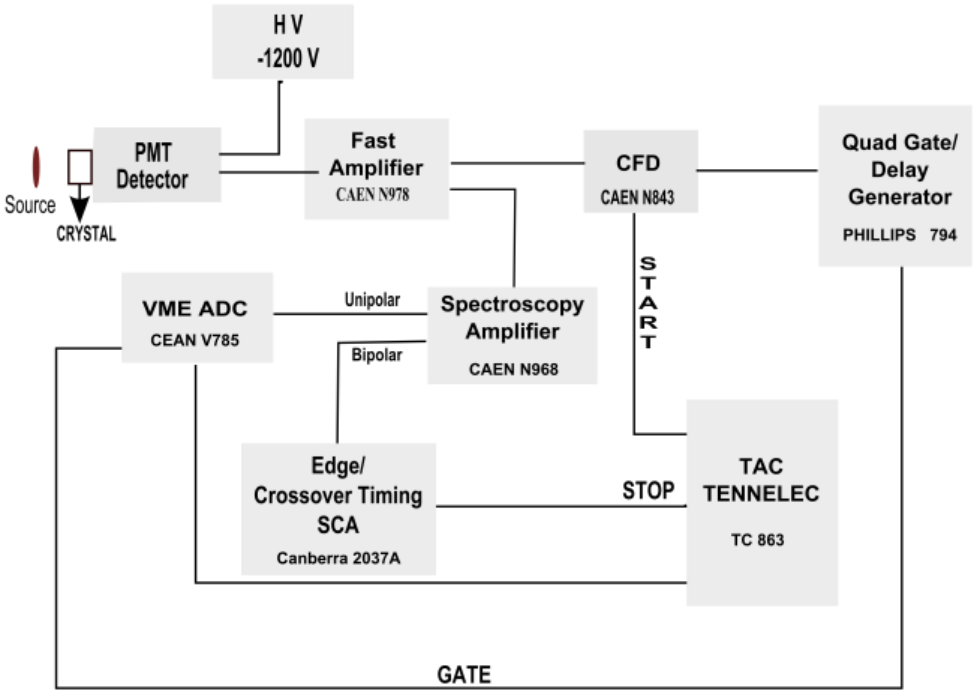

Figure 2.21 A schematic diagram of PSD measurement setup using zero crossing method [23].

2.9 Phoswich detector

In some of the alternate approaches to obtain the incident radiation dependent decay time, a new class of detectors has been proven to be useful for discriminating different kinds of radiation. These detectors are fabricated by employing a sandwich/combination of two or more dissimilar materials having different pulse-shape characteristics and coupled to a common photo-sensor. These are called phoswich detectors that include a combination of scintillating materials like organic, inorganic crystalline, thin films, etc. A typical decay pulse obtained from a phoswich detector in an oscilloscope is shown in Figure 2.22.

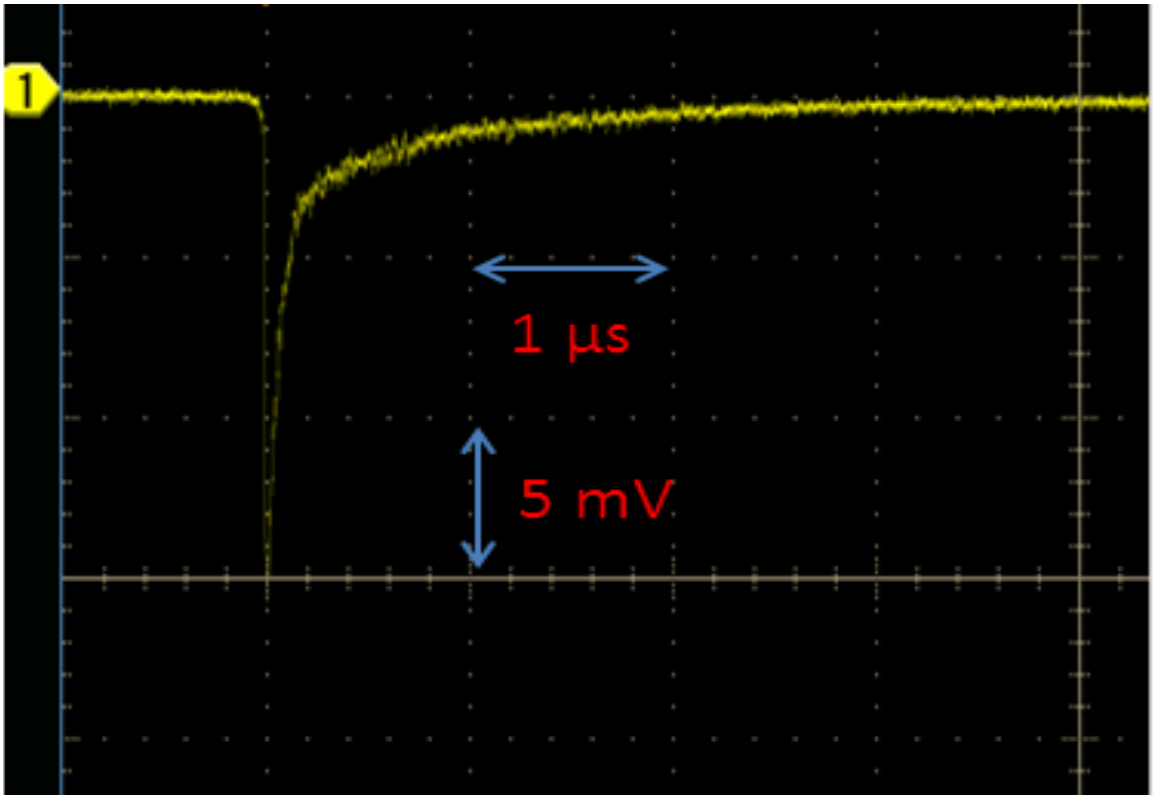

Figure 2.22 The scintillation decay curve for alpha particles and gamma rays measured with a phoswich detector.

These detectors have found various applications in routine as well as in advanced detector systems for particle spectrometry, simultaneous detection of beta and gamma radiations, background suppressed spectroscopy for low energy radiations, etc. Various phoswich detectors have been reported earlier by employing gas detectors, organic plastic scintillators, thin films, polycrystalline materials, and single crystals, etc. in combination with the similar phase material or single crystals [26-28]. However, the detectors fabricated from different phases other than single crystals suffer from with the problem of poor efficiencies especially at higher gamma energies. The single crystals have various advantages over other scintillating materials and therefore the phoswich combination of single crystal scintillators lead to the best results in various applications. However, the difference in refractive indices limits the choice of crystals to be optically coupled together. Additionally, the emission of light from the first crystal needs to be effectively transmitted through the second crystal without significant absorption/excitation.

References of chapter 2

[1] Brice, J. C., Crystal growth processes, Blackie Academic & Professional (an Imprint of Chapman & Hall) 1986.

[2] Bridgman, Percy W., Certain Physical Properties of Single Crystals of Tungsten, Antimony, Bismuth, Tellurium, Cadmium, Zinc, and Tin, *Proc. American Acad. Arts Science* **60**, 305–383 (1925).

[3] Jalalpour, M. H. and Talebnia, P., PPT on Crystal growth, K.N.T University of technology Electronic Department (2014).

[4] Vegad, M., and Bhatt, N. M., *Procedia Technology* **14**, 438 – 446 (2014).

[5] Tyagi, M., Singh, A. K., Singh, S. G., Desai, D. G., Patra, G. D., Sen, S., and Gadkari, S. C., Improvement of the scintillation properties of $Gd_3Ga_3Al_2O_{12}$:Ce,B single crystals having tailored defect structure *Phys. Stat. solidi-Rapid Research Letter* **9,** 530-534 (2015).

[6] Singh, A. K., PhD Thesis, Growth and characterization of $Li_6R(BO_3)_3$:R (R:Rare earth ions): Promising neutron detector (August 2018).

[7] Tyagi, M., Desai, D. G., Rawat, S., Singh, A. K., Sonawane, M., Sarkar, P. S., and Gadkari, S. C., Growth and characterization of large size $Gd_3Ga_3Al_2O_{12}$:Ce,B single crystal for high energy radiation detection, *DAE SSPS*, **H-123** (2017).

[8] Bunaciu, A. A., Udriştioiu, E. G., and Aboul-Enein, H. Y., X-Ray Diffraction: Instrumentation and Applications, *Critical Reviews in Analytical Chemistry* **45**, 289-299 (2015).

[9] Cullity, B. D., Elements of X-ray Diffraction, *3rd Ed.*, Addison Wesley, 2001

[10] Connolly, J. R., Introduction to X-Ray Powder Diffraction, Spring, 2007.

[11] https://www.physi.uni-heidelberg.de/Einrichtungen/FP/anleitungen/F69.pdf

[12] Hollas, J. M., Modern Spectroscopy, *4th Ed.*, John Wiley & Sons, Inc. 2003.

[13] Vij, D. R., Luminescence of Solids, Springer, 1998.

[14] Ronda, C., Luminescence: From Theory to Applications, Wiley, 2007.

[15] http://www.edinst.com/fl920p.htm

[16] https://www.britannica.com/science/radioluminescence

[17] Knoll, G. F., Radiation Detection and Measurement, *4th Ed.*, New York: John Wiley & Sons, 2010.

[18] http://www.vsl.cua.edu/cua_phy/images/6/6a/Presentation.pdf

[19] Kopar, S., Status and perspectives of solid state photon detectors. *Nucl. Instrum. Methods Phys. Res. Sect. A* **529**, 325-328, 2011.

[20] Renker, D., Geiger-mode avalanche photodiodes, history, properties and problems. *Nucl. Instrum. Methods Phys. Res. Sect. A* **567**, 48-56, 2004.

[21] https://hub.hamamatsu.com/jp/en/technical-note/how-sipm-works/index.html

[22] Janout, Z., Pospsil, S., and Vobecky, M., *J. Radio-analytical* **56**, 71-81, 1980.

[23] Rawat, S., Tyagi, M., Netrakanti, P. K., Kashyap, V. K. S., A. Mitra, Singh, A. K., Desai, D. G., Kumar, G. A., and Gadkari, S. C., Pulse shape discrimination properties of $Gd_3Ga_3Al_2O_{12}$:Ce single crystal in comparison with CsI:Tl, *Nucl. Instrum. Meth. Phys. Res. A* **840**, 186-191, 2016.

[24] Stevanato, L., Pulse shape discrimination with fast digitizers, *Nucl. Instrum. Methods Phys. Res. Sect. A* **748**, 33-38, 2014.

[25] Rawat, S., Tyagi, M., Kumar, G. A., and Gadkari, S. C., A novel versatile phoswich detector consisting of two single crystals to discriminate various kinds of radiation, *Review of Scientific Instruments* 2019 [Under review].

[26] Streun, M., Brandenburg, G., Larue, H., Saleh, H., Zimmermann, E., Ziemons, K., and Halling, H., Pulse shape discrimination of LSP and LuYAP scintillators for depth of intereaction detection in PET. *IEEE Trans. Nucl. Sci.* **50**, 344–347, 2003.

[27] Langenbrunner, J. L., Morris, C. L., and Whitton, R. M., Csl-phoswich detector for charged-particle identification. *Nucl. Instrum. Methods Phys. Res. Sect. A* **316**, 450–451, 1992.

[28] Czarnecki, S., Krol, A., Mandal, M., Poliks, M. D., Schmidtlein, C. R., Thompson, M., and Turner, J., Autonomous gamma, X-ray, and particle detector, US patent 9835737.

CHAPTER 3

Alpha-gamma pulse shape discrimination in Boron co-doped GGAG(Ce) and in CsI(Tl): A comparative study

---

This chapter discusses the comparative study of PSD performances of GGAG:Ce,B and CsI:Tl when coupled to a PMT and a SiPM. The boron co-doped GGAG:Ce was chosen because of its highest light output amongst co-doped GGAG:Ce crystals. The PSD of alpha and gamma radiations was done employing digital charge integration and analog zero crossover techniques. The decay time behavior of alpha and gamma radiations in GGAG:Ce,B and CsI:Tl scintillator was observed and reported to be opposite, for the first time.

3.1 Introduction

The scintillation performance of GGAG:Ce in gamma spectroscopy has been extensively investigated by employing various photo-sensors [1-4]. However, its performance in charged particle spectroscopy is yet to be explored in detail. Moreover, the development of new photo sensors and the state-of-the-art electronics has led to an investigation of crystal's performance in charged particle identification in order to explore the possibility of using them in the applications requiring compact detector geometry. The pulse shape discrimination (PSD) technique has been utilized in various crystals such as NaI:Tl, CsI:Tl, BaF_2, ZnS:Ag, $LaBr_3$, $LaCl_3$, YAG:Ce, LuAG:Ce and GGAG:Ce [5-12] for the explicit identification of charged particles, gammas and neutrons. The scintillation decay curve for these crystals consists of more than one exponential component. The relative ratio of these components depends on the nature of the exciting radiation due to the difference in ionization density caused by different energy loss mechanisms. Subsequently, the shape of the decay pulse can be used to distinguish the exciting radiations. The PSD techniques have been extensively used in the neutron spectroscopy for discriminating the gamma background [13]. Also, the fission events generating heavy charged particles can also be identified by using these techniques [14].

It is well known that CsI(Tl) scintillator crystals have been widely used for the detection of charged particles owing to their excellent light output of about 66,000 ph/MeV, two decay times of 680 and 3000 ns, emission at 550 nm and the cost effectiveness [15]. Due to the green-yellow emission, GGAG:Ce crystals can also be used with silicon based photo-sensors to fabricate the compact detectors in this regard [16]. The GGAG:Ce has an edge over CsI:Tl in being non-hygroscopic, denser and has a faster decay time. It has been reported that with boron co-doping, the self-absorption of scintillation light output (LO) in GGAG:Ce crystal decreases resulting in the improvement of energy resolution from 9% to 7.8% [3]. However, the PSD in boron co-doped GGAG:Ce has not been studied so far.

In this chapter, we report our studies on PSD characteristics of CsI:Tl and GGAG:Ce,B scintillators for charged particles and gamma rays. These studies were carried out using charge integration method and zero-crossing timing method. In addition to the conventional photomultiplier tube, the PSD capabilities of SiPM based CsI:Tl and GGAG:Ce, B detectors were also evaluated. After the detailed exploration of GGAG:Ce,B scintillator's PSD ability for charged particles and gamma rays, we have extended our work to measure its PSD ability for heavy ions and gamma rays by performing an in-beam experiment.

3.2 Experimental Details

Single crystals of GGAG:Ce,B were grown using the Czochralski. The initial concentration of dopant is 0.2 atomic percent and of codopant is also 0.2 atomic percent. These concentrations are with respect to Gd. The co-doping with boron was used based on recently reported work on the improvement of scintillation performance [2]. The CsI:Tl crystals were grown using the Bridgman technique. The initial concentration of thallium in the crystal is 0.15 atomic percent. The growth processes for these crystals in detail have been discussed in the recent publication [17]. Two samples of CsI:Tl and GGAG:Ce,B having similar dimensions of $18 \times 18 \times 10$ mm^3 were cut from the grown crystals. The surface which was used to couple photo-sensors optically was polished while the other surfaces were untouched. The samples were coupled to 2" Hamamatsu R1306 PMT using optical grease for efficient light collection.

In another set of experiments, the samples were coupled to SiPM (SenSL C type) having 6×6 mm^2 active area using an optical guide. The SiPM mounted on a PCB board having dual mode readout of fast and standard outputs was used in the zero-crossing method to get both timing and energy information from each pulse. It is operated at an overvoltage of 5 V which makes its photon detection efficiency 42%. The temperature of lab was controlled and maintained at 25°C with the help of air conditioner. The working of SiPM has been discussed in detail in chapter-2. The SiPM has two outputs signals : fast output (Fout) and slow output (Sout) signal The PSD was measured with Am-Pu alpha source that emits alpha particles of two energies 5.15 and 5.48 MeV while ^{60}Co was used as a gamma source. Alpha source is mounted on the crystal's non-polished surface with an aluminum collimator of thickness 25 μm. It has been found that the loss in the energy of alpha particles in aluminum is negligible. The assembly is then tightly wrapped with Teflon tapes leaving minimum air gap possible in between. The gamma source is kept at a distance of 5 cm in front of the detector. PSD measurements are carried out by deploying charge integration and zero-crossing methods. A CAEN make 14 bit, 16 channels digitizer (V1730) with DPP-PSD firmware and a sampling rate of 500 MS/s was used to integrate the pulse and obtain the charges for the different short and long time gates associated with alpha particles and gamma rays. The integrated charge in short and long gates is computed by the digitizer due to different pulse shapes of alpha and gamma decay. The discrimination parameter (PSD) of digitizer is given by Eq. (2.8). Various gate settings were used to observe the effect of charge collection on the discrimination and were subsequently optimized. Other parameters such as charge sensitivity, threshold, trigger hold-off, CFD fraction, pre-gate were also optimized to obtain the best possible discrimination. The corresponding optimum

values are 2, 100, 300, 25 and 132 respectively. These values are same for both the detector setups. The schematic setup given in Figure 2.19 was used for PSD measurements of alpha and gamma sources involving the digitizer.

In order to support the results obtained from the digitizer setup, a PSD technique for measuring zero-crossing time (ZCT) difference for gamma rays and alpha particles was used employing the schematic setup of ZCT given in Figure 2.20. An inverter was additionally used for SiPM based detectors. The detector pulses were then processed through a spectroscopy amplifier. However, a lower threshold cut-off was introduced to remove 59 keV gamma originating from the Am-Pu alpha source to obtain better FOM.

For in-beam experiment through ^{13}C(75 MeV) + ^{232}Th reaction, the GGAG:Ce,B scintillator coupled to 1" PMT is used. This detector was chosen as it demonstrated the highest PSD ability for alpha particles and gamma rays. The in-beam experiment was performed at 14 MV BARC-TIFR Pelletron facility, Mumbai. The experiment was performed using a ^{13}C beam of energy 75 MeV and a self-supporting metallic foil of ^{232}Th (1.6 mg/cm^2) was used as a target. A 5 mm collimator was used in front of the detector. The PSD was achieved using ZCT technique as discussed in chapter 2. The TAC range was kept at 2 μs. The energy signal (from PMT anode) and timing signal (from PMT dynode) were processed through spectroscopic and timing filter amplifiers, respectively.

3.3 Results and discussion

The CsI:Tl and GGAG:Ce,B crystals grown by Bridgeman and Czochralski techniques were found to be free from any visible cracks and inclusions. The processed samples of CsI:Tl and GGAG:Ce,B crystals having dimension of 18×18×10 mm^3 are shown in Figure 3.1. The samples were directly coupled to the PMT. However, a uniquely designed light-guide (shown in Figure 3.1 (c)) played a crucial role in coupling them with the SiPM for the maximum light collection. The light guide did not introduce significant variation in the pulse height of the decay spectrum which makes it suitable for our experiments. This was verified by recording the spectrum of ^{137}Cs using 5×5×5 mm^3 crystals of GGAG:Ce,B directly coupled to the SiPM. The measured energy resolution of light guide coupled scintillator at 662 keV was within the experimental error.

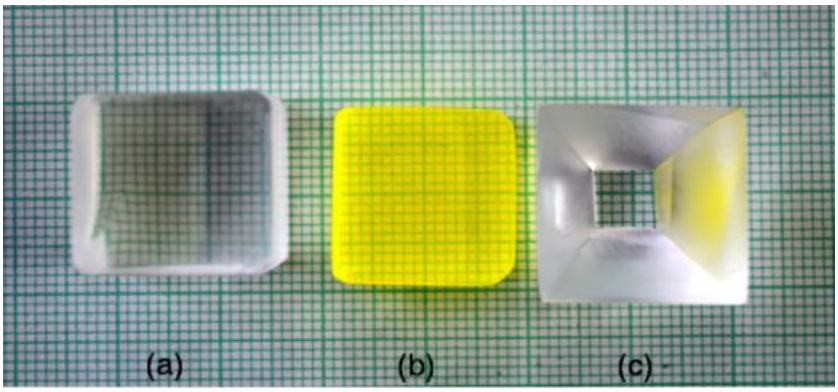

Figure 3.1 Single crystal of **(a)** CsI:Tl, **(b)** GGAG:Ce,B and **(c)** a light guide for coupling crystals with SiPM.

Figure 3.2 shows the normalized scintillation decay plots of CsI:Tl and GGAG:Ce,B crystals measured directly from the anode of a PMT using a fast digital oscilloscope

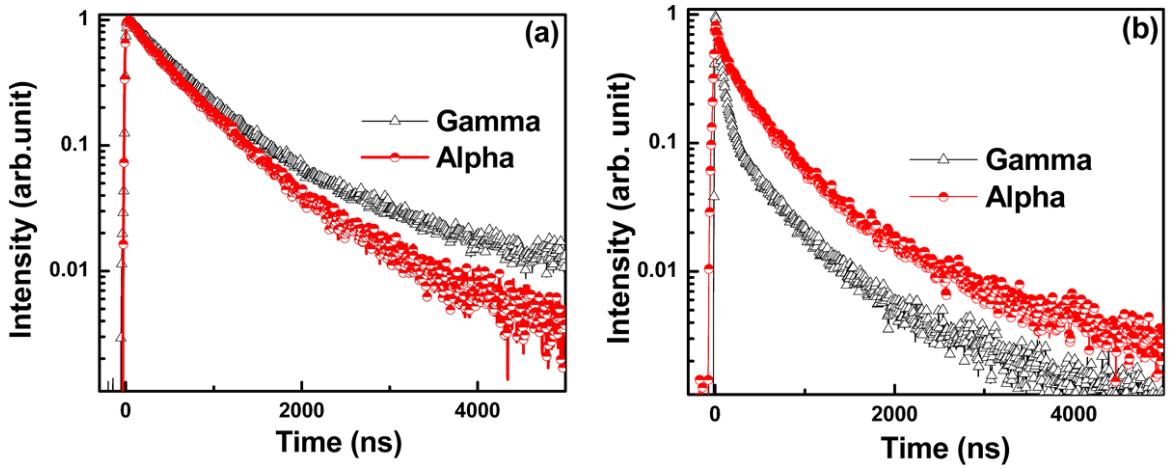

Figure 3.2 Normalized scintillation decay curves measured with alpha and gamma sources for **(a)** CsI:Tl and **(b)** GGAG:Ce,B crystals coupled to PMT.

. The decay curves for alpha and gamma radiations were exponentially fitted using Eq. (2.3). Relative ratio of decay components and average decay times for alpha and gamma radiations was calculated using Eq. (2.4) and Eq. (2.5). The decay time components of CsI:Tl detector for alpha excitation were measured to be 300 ns and 700 ns with relative intensities of 25% and 75% respectively. The corresponding average life time (amplitude weighted) was calculated to be about 600 ns. The decay times for gamma excitation were 700 ns and 3500 ns with relative contribution of 57% and 43% respectively and gamma average decay time of 1200 ns. These values are in good agreement with those reported earlier [18]. The acceleration of decay time due to alpha in comparison with gamma excitation may be attributed to the emission from some non-radiative

quenching processes of $(Tl^{+})^{*}$. These processes take place due to excited Tl+ state interaction with excited atoms created by the excitation of high ionization density alpha particles [19, 20]. However, the excitation in GGAG:Ce,B does not seem to follow the similar relaxation mechanism. In these crystals, the faster decay component at 61 ns and the slower one at 488 ns were found to have relative contributions of 77% and 23% respectively for gamma excitation. The average life time of gamma excitation is 108 ns. In contrast to CsI:Tl, alpha radiation slows down the decay time having components of 104 ns and 501 ns with relative intensities of 20% and 80% respectively that led to the average time of about 284 ns [22]. The fast component is due to the transition from 5d-4f state in Ce^{3+} while the slow component arises due to defect centres in GGAG:Ce,B crystal [3]. A similar mechanism has also been observed in an iso-structural YAG:Ce crystal [10]. Despite having a higher ionization density, there is an increase in the decay time for alpha excitation, which indicates the role of defect centres in the scintillation kinetics of these crystals. In order to understand the role of defects in relaxation mechanism of various excitation radiations, more experiments are in progress. After observing the dependence of decay time on ionization density, PSD studies of alpha particles and gamma rays were carried out by employing digitizer and zero-crossing setup. The PSD measurements, by using digitizer, are based on the charge collection in long (Q_L) and short gate (Q_S). The value of PSD, as given in Eq. (2.8), indicates the dependence of discrimination capability on Q_S / Q_L ratio. Therefore, to obtain the best PSD value, the corresponding gates are needed to be optimized for an effective capture of the fastest and the slowest components of light yield in short and long gates respectively. The figure of merit (FOM) describing the degree of discrimination between alpha and gamma pulses was calculated using Eq. (2.7). The effect of long gate selection on FOM, as shown in Figure 3.3, indicates the importance of the relationship between charge collection through different gates and PSD. The optimization of short gate and long gate were carried out in many runs of PSD measurements. Figure 3.4 (a) and (b) helped us to select the optimum SG and LG for the CsI:Tl scintillator.

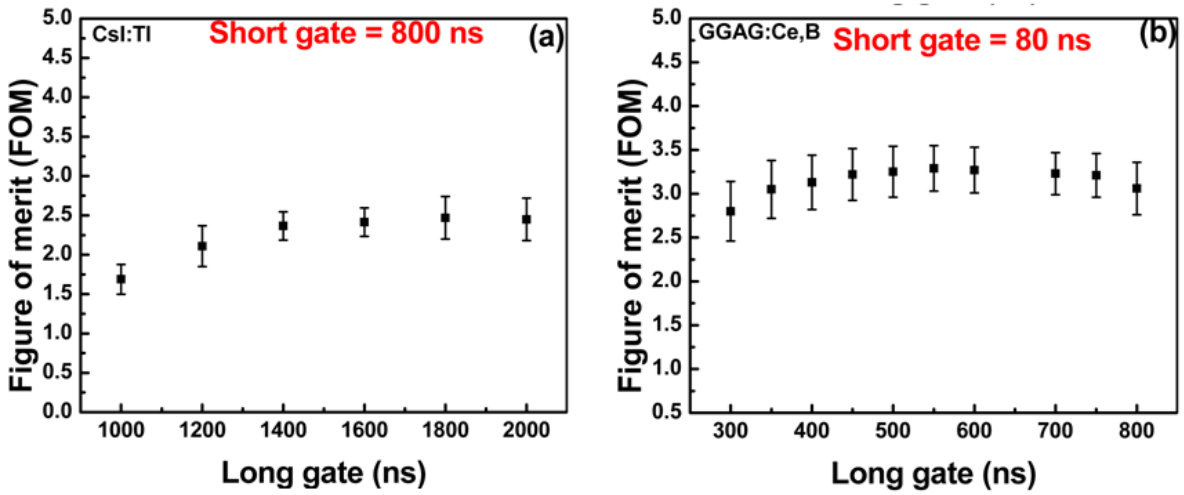

Figure 3.3 The effect of long gate settings on figure of merit (FOM) measured for **(a)** CsI:Tl and **(b)** GGAG:Ce, B crystals coupled to PMT.

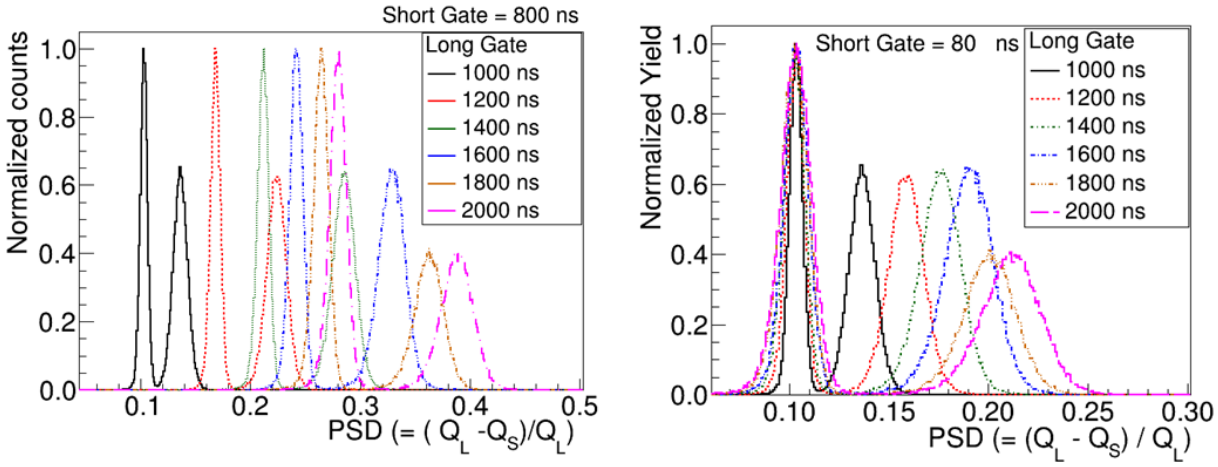

Figure 3.4 Optimum LG and SG FOM measured for **(a)** CsI:Tl and **(b)** GGAG:Ce, B crystals coupled to PMT.

Similar process was carried out to select SG and LG for GGAG:Ce,B scintillator. The short gate was optimized and fixed at 800 ns for CsI:Tl and 80 ns for GGAG:Ce,B. Initially, both graphs in Figure 3.3 depicted a trend of FOM getting better on increasing long gate, however once a maximum is attained, discrimination tends to either saturate or decrease. After measuring the FOM for various gate combinations, the short and long gates were optimized to 800 ns and 1600 ns respectively for CsI:Tl.

Similarly, the values for short and long gates were optimized to 80 ns and 550 ns for GGAG:Ce,B respectively. Figure 3.5 (a) and (b) show the scattered plots of PSD as a function of integrated charge for CsI:Tl and GGAG:Ce,B respectively. Its Y-axis represents the PSD values

between 0 and 1, as calculated from Eq. (2.8), while the pulse height (energy) of alpha and gamma is plotted along X-axis. Figure 3.5 (c) and (d) are the projections of PSD for the entire energy range of alpha and gamma. PSD scattered plot along Y-axis quantitatively demonstrates the degree of separation between alphas and gammas in terms of FOM. The value of FOM depends on the separation and FWHM gaussian peaks corresponding to alpha and gamma. The α/γ light yield ratio can be measured from the projection of the scattered graph along the X-axis. For CsI:Tl and GGAG:Ce,B crystals, the ratios were found to be 0.50 and 0.17 respectively. These values are reasonably in good agreement with the reported values [20, 12]. Keeping in mind the resolution of the crystals, the mean energy of 5.14 and 5.48 MeV alpha particles was considered for the measurements.

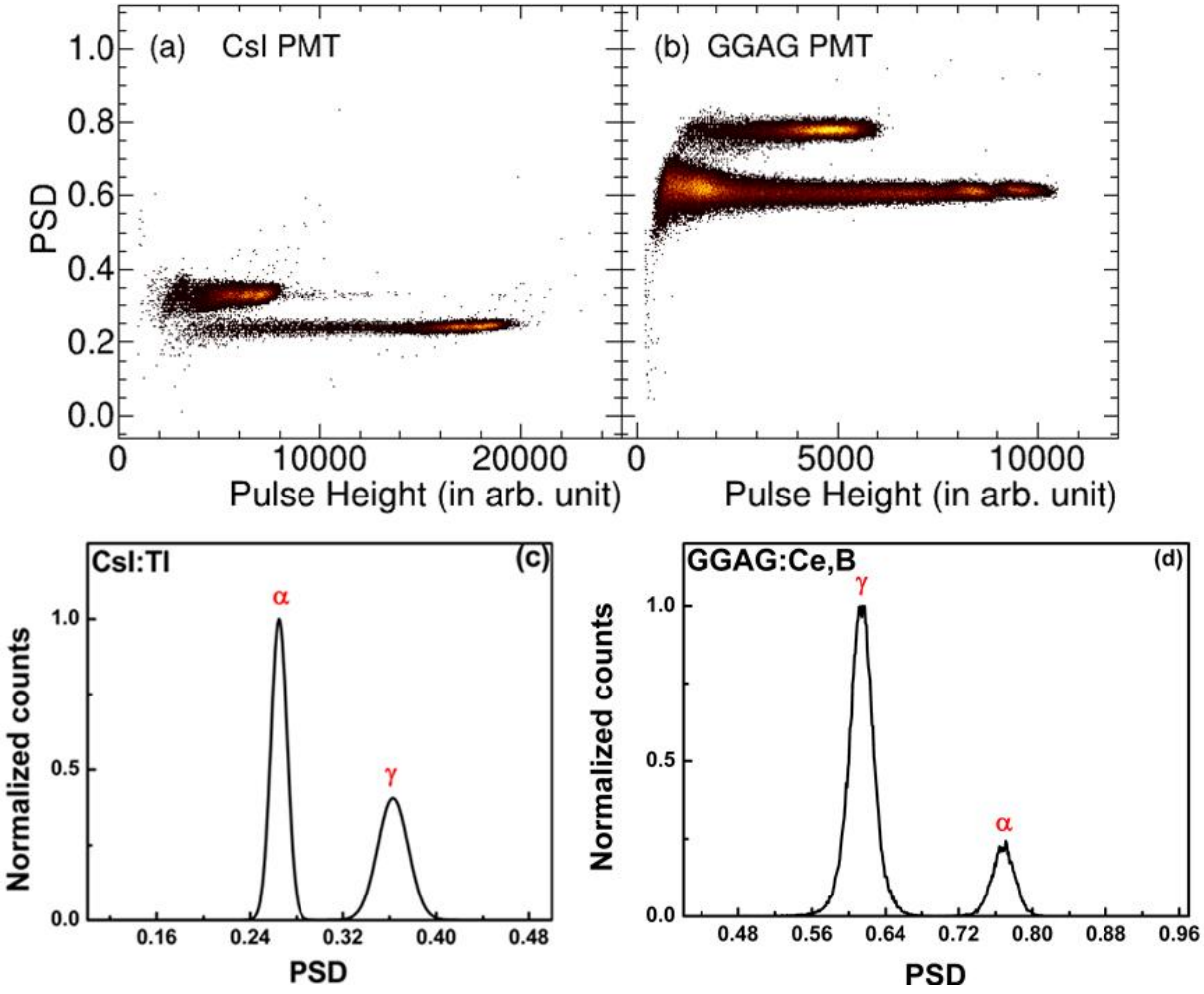

Figure 3.5 Results of PSD measurement using digitizer for alpha and gamma rays of **(a)** CsI:Tl and **(b)** GGAG:Ce,B crystals coupled to PMT. The projection along X-axis is shown for **(c)** CsI:Tl and **(d)** GGAG:Ce,B.

The opposite dependence of decay for alpha particles and gamma rays in CsI:Tl and GGAG:Ce,B can also be seen in Figure 3.5. In CsI:Tl (see Figure 3.5 (a)), the alpha excitation results in faster decay time as represented by lower blotch which appears at higher energies on X-axis owing to a relatively higher α/γ ratio. In GGAG:Ce,B (see Figure 3.5 (b)), the dependence is opposite where the spread on Y-axis represents alpha due to a longer decay time. The small α/γ ratio leads to the pulse height at lower channel numbers on X-axis. Although lower α/γ ratio for GGAG:Ce,B indicates stronger quenching due to high ionization density but it increases the decay time unlike CsI:Tl. The results point out the role of defect centres which release the trapped charges after some time and therefore increase in the decay time. The role of defect centres in scintillation kinetics has been explained by Tyagi *et al.*, in [3]. In spite of having poor α/γ ratio, there is a marked difference in Y projection due to the pulse shape difference caused by alpha and gamma excitations in both the detectors. The FOM values for CsI:Tl and GGAG:Ce,B were calculated to be 2.41 and 3.42 respectively which illustrates the PSD capabilities of these detectors. Even though α/γ ratio of CsI:Tl (0.50) is better than that of GGAG:Ce,B (0.17), FOM values suggest GGAG:Ce,B to be a better choice for charged particle identification based on PSD. It may be noted that the results presented are for the energies greater than 122 keV.

Moreover, in order to corroborate the digitizer firmware results, zero-crossing time difference of both the detectors was also measured using the conventional zero-crossing method as shown in Figure 3.6.

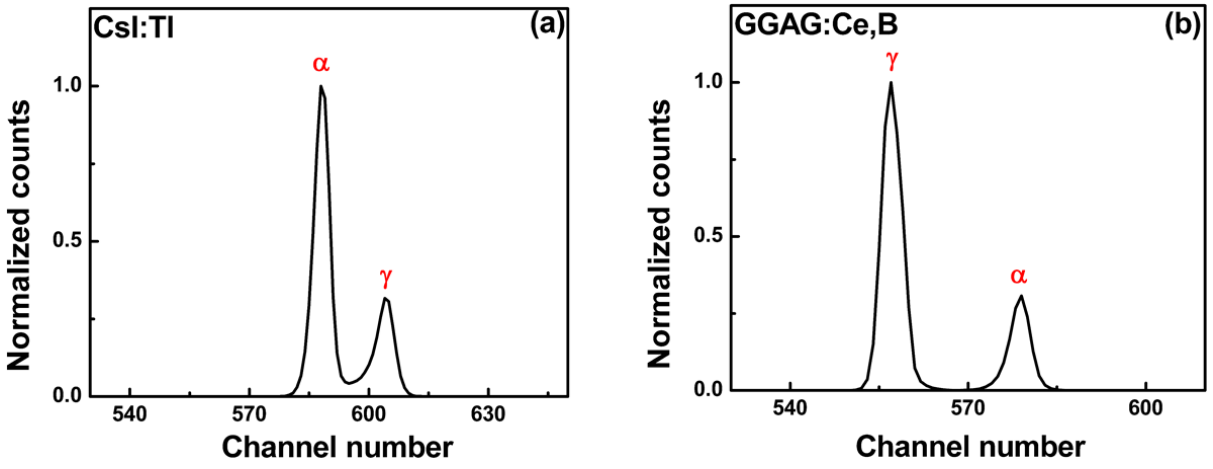

Figure 3.6 PSD for alpha and gamma rays in **(a)** CsI:Tl and **(b)** GGAG:Ce,B crystals coupled to PMT from zero-crossing setup.

The zero-crossing time difference of 89 ns and 60 ns for GGAG:Ce,B and CsI:Tl respectively was sensed by a timing single channel analyzer (TSCA). The greater value of FOM for GGAG:Ce,B crystal supports the measured results obtained using the digitizer. Exponential decay curves of both the crystals mounted on SiPM through light guide have also shown a similar dependence on alpha and gamma excitations as that measured with a PMT. The PSD comparison measured with the digitizer is shown in Figure 3.7.

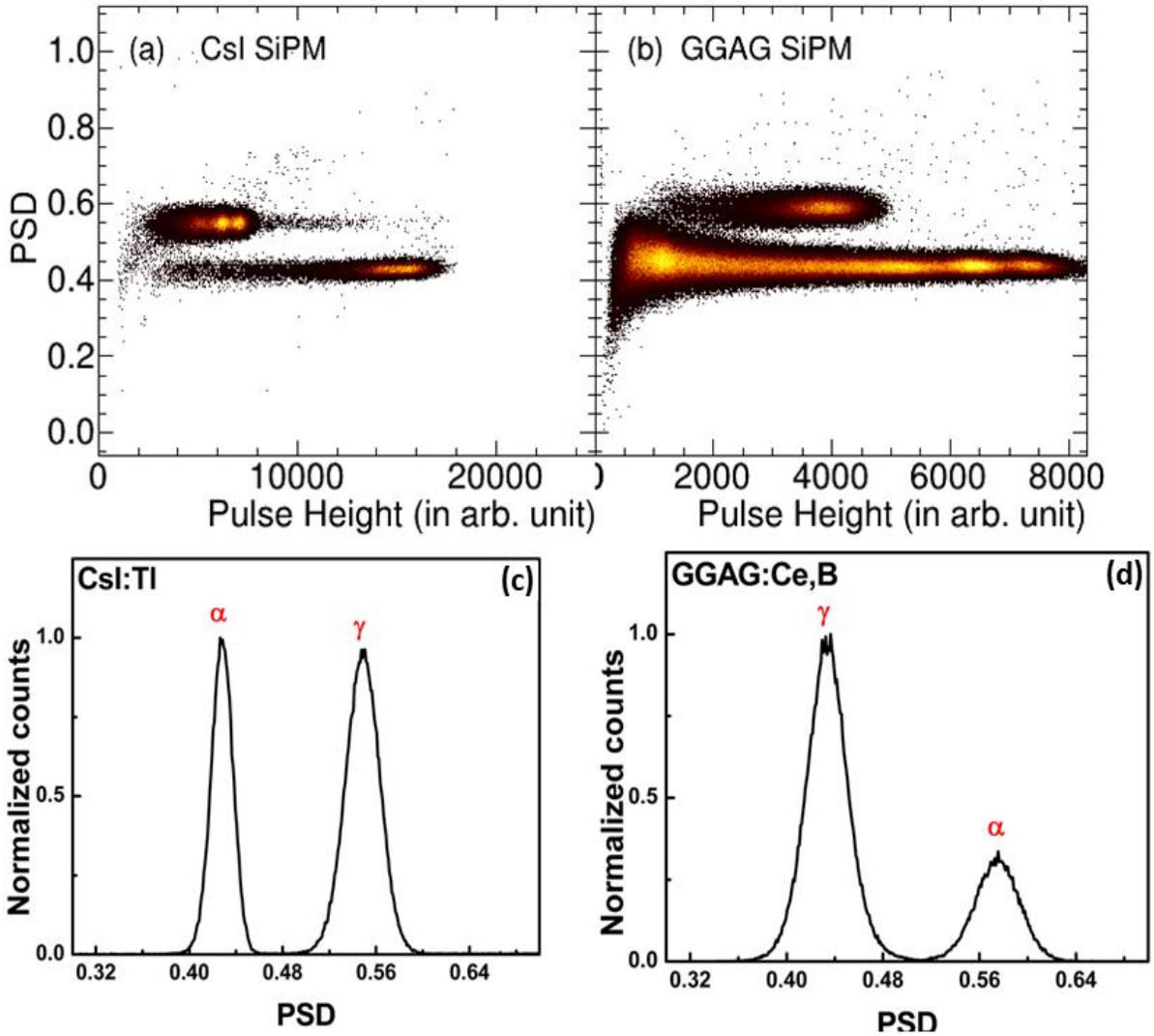

Figure 3.7 PSD plots for alpha and gamma rays of **(a)** CsI:Tl and **(b)** GGAG:Ce,B crystals coupled to SiPM from digitizer.

The PSD of CsI:Tl-SiPM detector is more than that of GGAG:Ce,B-SiPM detector. The separation between alpha and gamma is quite apparent in both the detectors in a compact geometry employing SiPM. The measured zero-crossing time difference of 114.7 ns for a GGAG:Ce,B-SiPM detector was found to be better than 102.0 ns measured for CsI:Tl-SiPM detector. These results

support the results obtained by employing PMT. In SiPM based detectors, a higher PSD from the zero-crossing method suggests better discrimination compared to PMT based detectors. This can be credited to better photon detection efficiency and good matching between emission wavelength of crystal and spectral sensitivity of SiPM (550 nm). Better compatibility of GGAG:Ce scintillators with SiPM has already been reported by Tyagi *et al.* [16] in which they have demonstrated that the timing properties strongly depend on the digital processing system.

Figure 3.8 indicates the PSD of CsI:Tl and GGAG:Ce,B using ZCT. However, the FOM for GGAG:Ce,B (1.54) is slightly less than that of CsI:Tl (1.71) which can be assigned to the energy spread especially at lower energies. It may be noted that the SiPM have higher noise contribution due to their single photon sensitivity, crosstalk and after-pulsing. An improvement in the back-end electronics and data acquisition may result in better FOM for SiPM detectors in support of higher zero-crossing time.

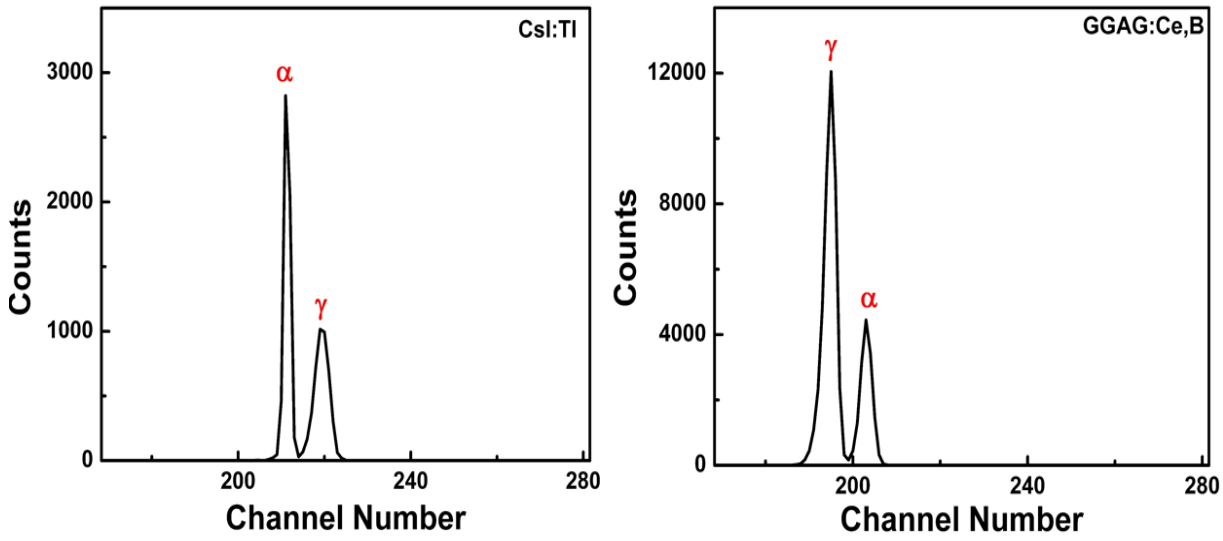

Figure 3.8 PSD plots for alpha and gamma rays of **(a)** CsI:Tl and **(b)** GGAG:Ce,B crystals coupled to SiPM from ZCT.

Table 3.1 shows the comparison of FOM values for alpha and gamma PSD of CsI:Tl and GGAG:Ce,B crystals coupled to PMT and SiPM using digitizer and analog PSD methods. It further lists the ZCT and FOM values of CsI:Tl and GGAG:Ce,B crystals coupled to SiPM obtained using the fast output (Fout) and slow output (Sout) signal combination and the individual splitting of Sout signal of SiPM employing zero-crossing technique. The improvement in FOM values from Fout + Sout signals than from Sout signal of SiPM has been observed in both the crystals. This higher value of FOM from Fout + Sout signal of SiPM is due to better frequency and decay time matching of the

crystals with the Fout + Sout signal of SiPM. The poor FOM value and ZCT of GGAG:Ce,B scintillator is due to high noise contribution as mentioned before.

Table 3.1 FOM and ZCT values of alpha and gamma PSD using CsI:Tl and GGAG:Ce,B crystals coupled to PMT and SiPM employing digitizer and analog technique.

Crystal Specification	**Photomultiplier Tube**		**Silicon Photomultiplier**	
	Digitizer	**Zero Crossing**	**Digitizer**	**Zero Crossing**
CsI:Tl (18 mm)	2.41 (SG:800 LG:1600)	60.53 ns	2.80	104.00 ns (Fout + Sout)
				102.45 ns (Sout)
GGAG:Ce,B (18 mm)	3.42 (SG:80 LG:550)	87.06 ns	1.7	114.7 ns (Fout + Sout)
				83.53 ns (Sout)

PSD of GGAG:Ce,B scintillator carried out using known alpha and gamma sources has shown that it is capable of distinguishing charged particles. To test its PSD capability for charged particles other than alpha particles, GGAG:Ce,B detector coupled to PMT was tested in an in-beam experiment. Particles of different Z= 2, 3, 4 and 6 were produced in ^{13}C (75 MeV) + ^{232}Th reaction [24]. The light (Z = 2 and 3) and heavy (Z = 4 and 6) charged particles were detected by GGAG:Ce,B detector. Experiment resulted in a typical two-dimensional plot of the ZCT versus energy as shown in Figure 3.9 for a detector angle of 81° with respect to the beam direction. Particle identification from this plot can be grouped into two bands corresponding to gamma rays and charged particles. Gamma rays appear with a long tail along energy axis due to the small thickness (1 mm) of the GGAG:Ce,B scintillator. As can be seen in the figure, two bands are merging into each other at low energies. With increase in the energy of radiation, the separation between the bands becomes more prominent. The separation between lighter and heavier charged particle could be observed at higher energies only. Although GGAG:Ce,B crystals were reported to have better alpha gamma discrimination, the separation of charged particles was found to be weaker in comparison to that of measured with CsI:Tl scintillators [25]. A strange feature of ZCT turn around at high energies was observed. An interesting trend of the turn-around was also noted. The turn-around energy increases for gamma rays to lighter charged particles to heavier ^{13}C particles having energy of around 65 MeV.

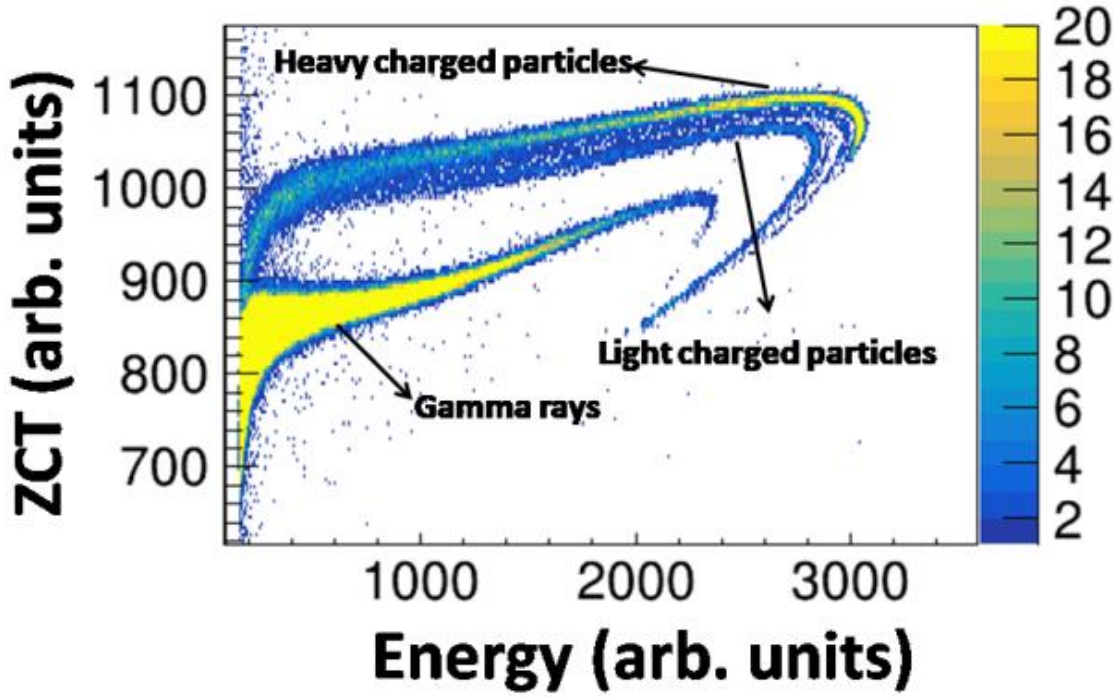

Figure 3.9 Two dimensional plot of ZCT versus energy.

3.4 Summary

In spite of a stronger quenching of emission, alpha excitation slows down the scintillation decay time in GGAG:Ce,B crystals unlike other halide scintillators where higher ionization density excitation makes scintillation decay faster. The PSD is observed to be better in GGAG:Ce,B crystals in comparison to CsI:Tl [22]. The FOM was calculated to be 3.42 in GGAG:Ce,B crystals which is higher compared to 2.41 in CsI:Tl crystals. The highest zero-crossing time difference of 114.7 ns was also obtained when GGAG:Ce,B scintillator was coupled with SiPM. However, lower FOM values from SiPM based detectors are expected to improve with better parameter optimization and electronics. More experiments are in progress to understand the PSD performance of GGAG:Ce,B detector for lighter and heavier charged particles along with gamma rays for large range of energies.

References of chapter 3

[1] Iwanowska, J., Swiderski, L., Szczesniak, T., Sibczynski, P., Moszynski, M., Grodzicka, M., Kamada, K., Tsutsumi, K., Tsutsumi, Y., Yanagida, T., et al., Performance of cerium-doped $Gd_3Ga_3Al_2O_{12}$ (GAGG:Ce) scintillator in gamma-ray spectrometry, *Nucl. Instrum. Methods Phys. Res. Sect. A* **712**, 34 (2013).

[2] Tyagi, M., Singh, A. K., Singh, S. G., Desai, D. G., Patra, G. D., Sen, S., and Gadkari, S. C., Improvement of the scintillation properties of $Gd_3Ga_3Al_2O_{12}$:Ce,B single crystals having tailored defect structure *Phys. Stat. solidi-Rapid Research Letter* **9,** 530-534 (2015).

[3] Tyagi, M., Meng, F., Koschan, M., Donnald, S. B., Rothfuss, H., and Melcher, C. L., Effect of codoping on scintillation and optical properties of a Ce-doped $Gd_3Ga_3Al_2O_{12}$:Ce scintillator. *J. Phys. D* **46**, 475302 (2013).

[4] Tamagawa, Y., Inukai, Y., Ogawa, I., and Kobayashi, M., Alpha–gamma pulse-shape discrimination in $Gd_3Al_2Ga_3O_{12}$ (GAGG):Ce^{3+} crystal scintillator using shape indicator, *Nucl. Instrum. Methods Phys. Res. Sect. A* **795**, 192 (2015).

[5] Bartle, C. M., 1975. A study of (n,p) and (n,α) reactions in NaI(Tl) using a pulse-shape-discrimination method, *Nucl. Instrum. Methods* **124**, 547 (1975).

[6] Winyard, R. A., Lutkin, J. E., and McBeth, G. H., Pulse shape discrimination in inorganic and organic scintillators, *Nucl. Instrum. Methods* **95**, 141 (1971).

[7] Dafni, E., 1987. A note on the application of BaF_2 scintillators to γ-ray and charged particle detection, *Nucl. Instrum. Methods* **254**, 54 (1987).

[8] White, T. L., and Miller, W. H., A triple-crystal phoswich detector with digital pulse shape discrimination for alpha/beta/gamma spectroscopy, *Nucl. Instrum. Methods Phys. Res. Sect. A* **422**, 144 (1999).

[9] Crespi, C. L., Camera, F., Blasi, N., Bracco, A., Brambilla, S., Million, B., Nicolini, R., Pellegri, L., Riboldi, S., Sassi, M., et al., Alpha–gamma discrimination by pulse shape in $LaBr_3$:Ce and $LaCl_3$:Ce, *Nucl. Instrum. Methods Phys. Res. Sect. A* **602**, 520 (2009).

[10] Ludziejewski, T., Moszynski, M., Kapusta, M., Wolski, D., Klamra, W., and Moszynska, K., Investigation of some scintillation properties of YAG:Ce crystals, *Nucl. Instrum. Methods Phys. Res. Sect. A* **398**, 287 (1997).

[11] Kamada, K., Yanagida, T., Endo, T., Tsutumi, K., Usuki, Y., Nikl, M., Fujimoto, Y., Fukabori, A., and Yoshikawa, A., 2 inch diameter single crystal growth and scintillation properties of Ce:$Gd_3Al_2Ga_3O_{12}$, *J. Cryst. Growth* **352**, 88–90 (2012).

[12] Kobayashi, M., Tamagawa, Y., Tomita, S., Yamamoto, A., Ogawa, I., and Usuki, Y., Significantly different pulse shapes for γ- and α-rays in $Gd_3Al_2Ga_3O_{12}:Ce^{3+}$ scintillating crystals, *Nucl. Instrum. Methods Phys. Res. Sect. A* **694**, 91 (2012).

[13] Alderighi, M., Anzalone, A., Basssini, R., Berceanu, I., Blicharska, J., Boiano, C., Borderie, B., Bougault, R., Bruno, M., Cali, C., Particle identification method in the CsI(Tl) scintillator used for the CHIMERA 4π detector, *Nucl. Instrum. Methods Phys. Res. Sect. A* **489**, 257 (2002).

[14] D.L. Horrocks, 1974. Applications of liquid scintillation counting, Academic Press Inc. Ltd. London.

[15] Wagner, A., Tan, W. P., Chalut, K., Charity, R. J., Davin, B., Larochelle, Y., Lennek, M. D., Liu, T. X., Liu, X. D., Lynch, W. G., et al., Energy resolution and energy–light response of CsI(Tl) scintillators for charged particle detection, *Nucl. Instrum. Methods Phys. Res. Sect. A* **456**, 290 (2001).

[16] Tyagi, M., Desai, V. V., Singh, A. K., Singh, S. G., Sen, S., Nayak, B. K., and Gadkari, S. C., Timing characteristics of Ce doped $Gd_3Ga_3Al_2O_{12}$ single crystals in comparison with CsI(Tl) scintillators, *Physica Status Solidi (a)* **212**, 2213 (2015).

[17] Singh, S. G., Desai, D. G., Singh, A. K., Tyagi, M., Sen, S., Sinha, A. K., Gadkari, S. C., and Gupta, S. K., Growth of CsI:Tl crystals in carbon coated silica crucibles by the gradient freeze technique, *Journal of Crystal Growth* **351**, 88 (2012).

[18] Valentine, J. D., Moses, W.W., Derenzo, S. E., Wehe, D. K., and Knoll, G. F., Temperature dependence of CsI(Tl) gamma-ray excited scintillation characteristics, *Nucl. Instrum. Methods* **325**, 147 (1993).

[19] Kudin, A. M., Sysoeva, E. P., Sysoeva, E. V., Trefilova, L. N., and Zosim, D. I., Factors which define the α/γ ratio in CsI:Tl crystals, *Nucl. Instrum. Methods Phys. Res. Sect. A* **537**, 105 (2005).

[20] Dinca, L. E., Dorenbos, P., de Haas, J. T. M., Bom, V. R., and Van Eijik, C. W. E., Alpha–gamma pulse shape discrimination in CsI:Tl, CsI:Na and BaF_2 scintillators, *Nucl. Instrum. Methods Phys. Res. Sect. A* **486**, 141-145 (2002).

[21] Stracener, D. W., Sarantites, D. G., Sobotka, L. G., Elson, J., Hood, J. T., Majka, Z., Abenante, V., Chbihi, A., and Hensley, D. C., Dwarf Ball and Dwarf Wall: Design, instrumentation, and

response characteristics of a 4π CsI(Tl) plastic phoswich multidetector system for light charged particle and intermediate mass fragment spectrometry, *Nucl. Instrum. Methods Phys. Res. Sect. A* **294**, 485-503 (1990).

[22] Rawat, S., Tyagi, M., Netrakanti, P. K., Kashyap, V. K. S., Singh, A. K., Desai, D. G., Mitra, A., Kumar, G. A., and Gadkari, S. C., Pulse shape discrimination properties of $Gd_3Ga_3Al_2O_{12}$:Ce single crystal in comparison with CsI:Tl, *Nucl. Instrum. Methods Phys. Res. A* **840**, 18 (2016).

[23] Preziosi, E., Pani, R., Trigila, C., Polito, C., Bettiol, M., Borrazzo, C., Cinti, M. N., Fabbri, A., Pellegrinie, R., and Panig, R., A crystal identification method for monolithic phoswich detectors based on scintillation light distribution, *J. Inst.* **11**, P12009 (2016).

[24] Gupta Y. K., Chettri, S., Biswas, D. C., Prajapati, G. K., Joshi, B. N., Dubey, S., Danu, L. S., Mukhopadhyay, S., Kumar, N., Vind, R. P., et al., Transfer angular distributions in $^{12,13}C$ + ^{232}Th and ^{13}C + $^{207,208}Pb$ reactions at E_{Beam} =75 MeV, Proceedings of the DAE Symp. on Nucl. Phys. **62**, 620 (2017).

[25] Benrachi F., Chambon, B., Cheynis, B., Drain, D., Pastor, C., Seghier, D., Zaid, K., Giorni, A., Heuer, D., Lleres, A., et al., 1981. Investigation of the performance of CsI(Tl) for charged particle identification by pulse-shape analysis, *Nucl. Instrum. Methods Phys. Res. Sect. A* **281**, 137-142.

CHAPTER 4

Efficiency studies of GGAG:Ce scintillators

This chapter discusses detailed realistic Monte Carlo simulations of absolute efficiencies (both total detection and photo-peak) of GGAG:Ce scintillator for gamma rays up to energy of 5 MeV and for different values of source-to-detector separation. Simulations were also made with different scintillators ($LaBr_3$:Ce, NaI:Tl, CsI:Tl, BaF_2 and SrI_2:Eu) for comparison. Owing to its high Z_{eff} and high density, GGAG:Ce clearly outshines these detectors in terms of efficiency. The simulated and measured efficiencies of GGAG:Ce scintillator for 662 keV gamma energy for source-to-detector separation upto 10 cm, has been reported for the first time.

4.1 Introduction

With humans trying to explore each and every aspect of their universe, the scintillators used for the radiation spectroscopy have evolved more and more towards an ideal type. In general, an ideal scintillator must have high detection efficiency, high light yield, good energy and timing resolutions, transparent to visible light, high stability in light output with change in temperature, robust and high radiation hardness. Inorganic scintillators tend to fulfil most of the above stated criteria, in comparison to organic scintillators, to some extent. The properties and standards of an ideal scintillator are difficult to attain in reality and there is usually a trade-off among some of the properties according to the required application. Gamma spectroscopy is one of the applications which require detectors with high Z_{eff} and high density [1]. For activity measurements, the knowledge of absolute efficiency of the detector is important. Therefore, high detection efficiency (both total detection and photo-peak) constantly lures researchers to look for scintillators with high density and large atomic number. The detection efficiency is a measure of the percentage of radiation that a given detector detects from the overall yield emitted by the radioactive source [2]. The measured efficiency depends on source-detector geometry, energy of incident radiation, absorption cross-section in the material and attenuation layers in front of the detector [3].

Among the recently discovered oxide scintillators, GGAG:Ce (gadolinium gallium aluminium garnet) is found to possess density (6.7 g/cm^3) and Z_{eff} (55) similar to that of high efficient BGO (7.13 g/cm^3 and 73 [19]) and $CdWO_4$ (7.9 g/cm^3 and 74 [20]) scintillators for gamma rays. Efficiency studies of GGAG:Ce are therefore of primary interest when the need for high gamma-ray counting efficiency outweighs energy resolution [11]. Several studies on efficiency measurements were made in the past with different types of scintillators. Melcher *et al.,* [12] have reported simulated photo-peak efficiency of BGO and $CdWO_4$ relative to NaI:Tl as 3.3 and 3.2 respectively. Kumar *et al.,* [13] have carried out detailed studies on energy dependent total detection efficiency (TDE) and photo-peak efficiency (PE) of 25.4 mm × 25.4 mm cylindrical $LaBr_3$:Ce both experimentally and using GEANT4 simulation toolkit.

In the present chapter, we have made extensive realistic Monte Carlo simulations of the absolute efficiencies of GGAG:Ce, $LaBr_3$:Ce, NaI:Tl, CsI:Tl, BaF_2 and SrI_2:Eu using GEANT4 simulation toolkit considering ^{137}Cs source [14]. These simulations were carried out for different values of source-to-detector separation ranging from 0 to 10 cm. In order to validate the simulations, we have made measurements of TDE and PE of above mentioned scintillators using a ^{137}Cs source. We could not carry out measurements with SrI_2:Eu due to its unavailability in our lab.

4.2 Simulations

GEANT4 (**Ge**ometry **An**d **T**racking) is a simulation toolkit which can be used to accurately track the passage of the particles through matter [14]. It was developed by CERN for high energy physics experiments. It requires a detailed description of the geometry of the experimental setup and environmental assessment with respect to their dimensions, range cut, and number of events, relevant physics list, materials and shapes, as well as types of radiation particles falling on the detector. Details of detector's active volume and geometry are provided in the detector construction file. General Particle Source (GPS) module has been used as the particle generator. The source-detector setup simulated for the efficiency measurement is given in Figure 4.1. The three dimensional view of GGAG:Ce crystal geometry is shown in Figure 4.1 (a).

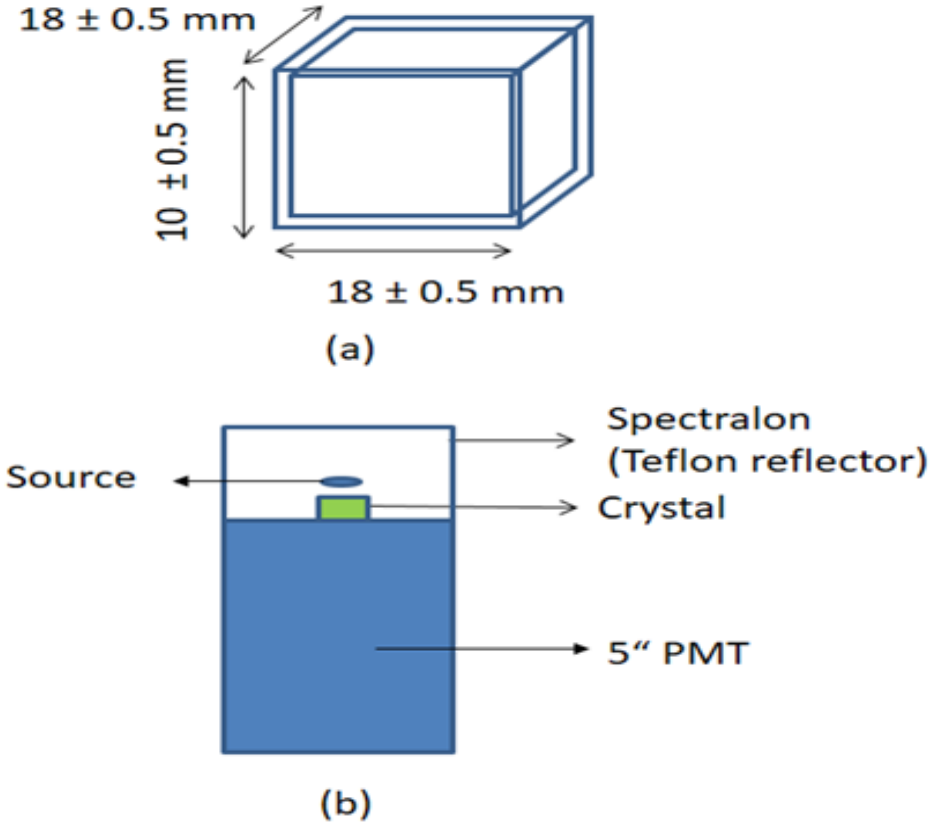

Figure 4.1. (a) GEANT4 simulated three-dimensional view of the GGAG:Ce crystal, **(b)** Schematic of detector setup used in the present work.

Simulations were also carried out with $LaBr_3$:Ce, NaI:Tl, CsI:Tl, BaF_2 and SrI_2:Eu crystals for the comparison. The simulations were done for a large number (10^6) events considering an isotropic point source. The simulations were made taking all possible physics processes into account. Since the simulations have been carried out for a large number of events, the statistical uncertainty is found

to be negligible. The secondary production threshold was set at 2 keV. GEANT4 toolkit has the provision to simulate the decay scheme of a radioactive source by considering all possible transitions. However, in the toolkit we have used a radioactive-decay module which generates all the decay components radiated from specific radioactive gamma source, procuring information from the Evaluated Nuclear Structure Data File [15]. The calculation of efficiencies for mono-energetic gamma sources can be obtained from the total and the photo-peak areas in the generated energy spectra. The TDE and PE can be defined as [11]:

$$\varepsilon_{TDE} = \frac{Total\ no.\ of\ counts\ in\ the\ spectrum}{No.\ of\ gamma\ rays\ emitted\ by\ the\ source} \quad (4.1)$$

$$\varepsilon_{PE} = \frac{No.\ of\ counts\ under\ the\ photopeak}{No.\ of\ gamma\ rays\ emitted\ by\ the\ source} \quad (4.2)$$

The errors in the simulated efficiencies have been calculated using the uncertainty in the components of the geometry and dimension of the detector, as provided by the manufacturer.

4.3 Experimental details

In order to validate the simulated results, the measurements were made with GGAG:Ce, CsI:Tl and BaF_2 crystals. Table 4.1 provides the details of scintillators used in the present work. The single crystal of GGAG:Ce was grown using Czochralski technique while single crystals of CsI:Tl and BaF_2 were grown via Bridgeman method. A 18 mm × 18 mm × 10 mm GGAG:Ce, a 25.4 mm × 10 mm cylindrical CsI:Tl and a 30 mm × 30 mm cylindrical BaF_2 crystals were cut and optically polished for the measurements. One of the polished surface of the crystals was coupled to a 5" Hamamatsu PMT using an optical grease. A 5" hemispherical reflector (spectralon) was mounted on the crystal plus PMT system. Use of hemispherical spectralon for efficiency measurements ensured maximum light collection by the scintillator crystal. The whole setup including preamplifier is placed in a light tight box for accurate efficiency measurements. The detector setup used for efficiency is shown in Figure 4.1(b). We have used four low activity gamma sources, namely, ^{137}Cs (115 kBq), ^{134}Cs (152 kBq), ^{60}Co (104 kBq), ^{22}Na (60 kBq) and ^{57}Co (118 kBq) for the energy calibration. The low activities were chosen to minimize the effects of pileup and dead time in the anode signal. TDE and PE data was obtained by keeping ^{137}Cs source above the detector assembly at various distances for the duration of 1000s.

Table 4.1 Details of scintillators used.

Scintillator	Geometry	Dimensions	Manufacturer
GGAG:Ce	Cuboid	18 mm × 18 mm × 10 mm	Grown by Czochralski method (in our lab)
	Cylindrical	24 mm × 19 mm	
$LaBr_3$:Ce	Cylindrical	25.4 mm × 25.4 mm	Saint Gobain
NaI:Tl	Cylindrical	50.8 mm × 50.8 mm	Canberra
CsI:Tl	Cylindrical	24.5 mm × 10 mm	Grown by Bridgman method (in our lab)
BaF_2	Cylindrical	30 mm × 30 mm	

A CAEN made voltage sensitive preamplifier and a CANBERRA made spectroscopy amplifier were used for pulse processing. A Tukan 8k MCA has been used to obtain and analyze the energy spectra. Efficiency analysis has been carried out by subtracting the background spectrum and correcting it for dead time. Following simple equation is used for experimental calculation of absolute detection efficiency using ^{137}Cs source [16]:

$$\varepsilon_{TDE} = \frac{N_{det}}{Atp}\, C_d \tag{4.3}$$

where N_{det} is the total number of gamma-rays detected, A is the activity of the gamma source, t is the acquisition time, p is transition probability corresponding to the 662 keV gamma emission and C_d is the correction factor due to dead time. The absolute photo-peak efficiency is given by:

$$\boldsymbol{\varepsilon_{PE} = \frac{N_{peak}}{Atp}\, C_d} \tag{4.4}$$

where N_{peak} denotes the total number of counts under the photo-peak.

Similarly, measurements were carried out with a cylindrical CsI:Tl detector of size 25.4 mm × 10 mm and a cylindrical BaF_2 detector of size 30 mm × 30 mm for 662 keV considering the source-to-detector separations in the range of 0 to 10 cm.

4.4 Results and discussion

Table 4.2 shows the simulated energy dependent TDE and PE curves for different scintillators having similar dimensions (18 mm × 18 mm × 10 mm) and for gamma energy of 662 keV when the source is placed 0.5 mm away from the crystal [17]. Clearly, GGAG:Ce possesses highest TDE and PE and NaI:Tl possesses lowest TDE and PE. The percentage difference in TDE of GGAG:Ce and NaI:Tl for 662 keV is 40%. Whereas, the percentage difference in PE of GGAG:Ce and NaI:Tl for 662 keV is 61% [17].

Table 4.2 Simulated TDE and PE of different scintillators having dimensions 18 mm × 18 mm × 10 mm for gamma energy of 662 keV when source-to-detector separation is 0.5 mm.

Scintillator	**TDE (in %)**	**PPE (in %)**
GGAG:Ce	19.18	7.18
$LaBr_3$:Ce	14.54	3.42
BaF_2	14.49	4.34
CsI:Tl	13.56	4.33
SrI_2:Eu	13.54	3.73
NaI:Tl	11.36	2.77

Figure 4.2 shows simulated TDE and PE curves for different scintillators in comparison with GGAG:Ce for two geometries (cuboid and cylindrical) and for different values of source-to-detector separation for 662 keV gamma energy. With increase in source-to-detector distance, a decrease in solid angle takes place and all scintillators tend to follow same trend of decrease in TDE and PE values. Again, GGAG:Ce possess highest TDE and PE and NaI:Tl possess lowest TDE and PE in the entire range of source-to-detector separations. For example, for a source-to detector separation of 1.0 cm, the percentage difference in TDE of GGAG:Ce and NaI:Tl is 39.5%. Whereas, the corresponding percentage difference in PE of GGAG:Ce and NaI:Tl is 60.5% .

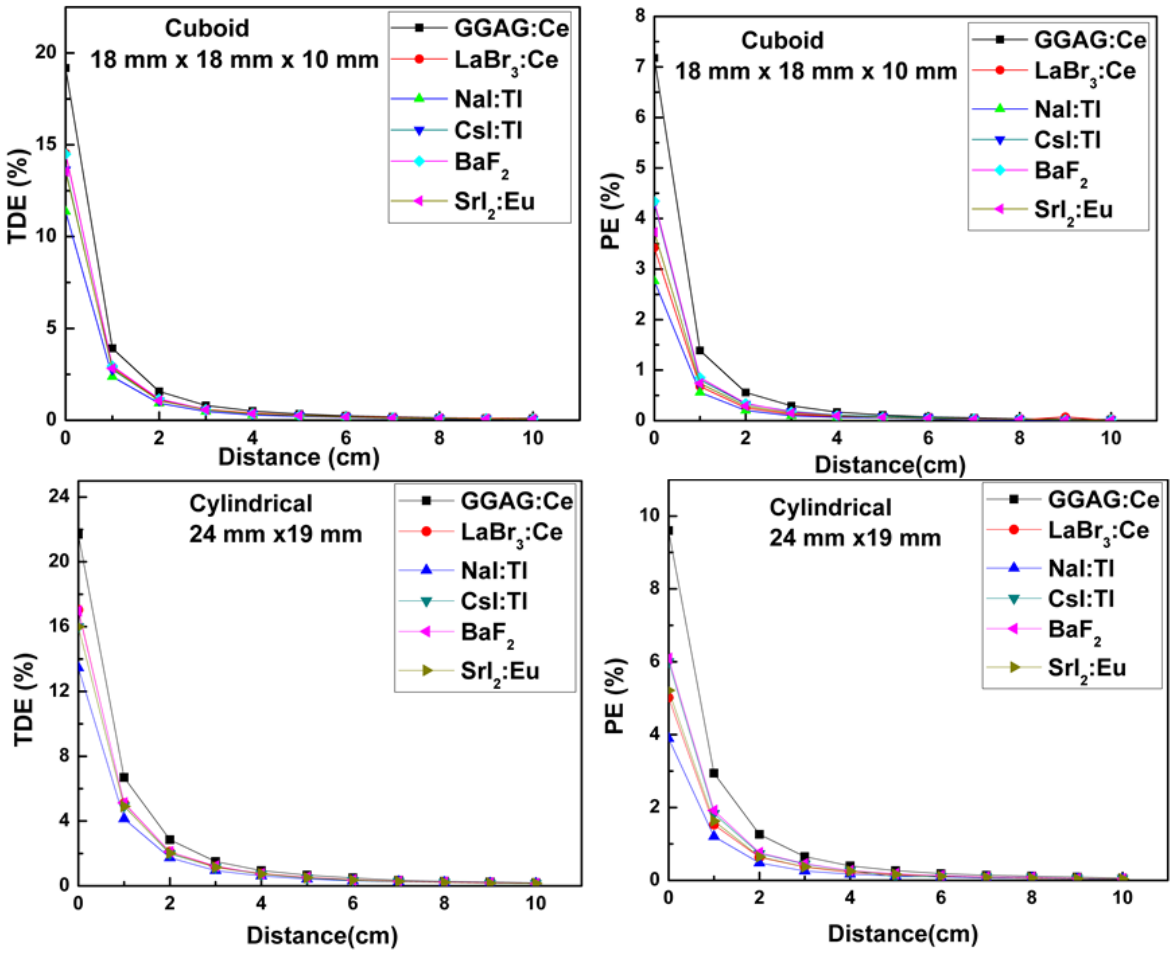

Figure 4.2 TDE and PE curves of different scintillators of dimensions 18 mm × 18 mm × 10 mm (cuboid) and 24 mm × 19 mm (cylindrical) for different source-to-detector separations for 662 keV gamma energy.

Table 4.3 demonstrates the simulated TDE and PE values for cuboid and cylindrical geometries of GGAG:Ce, $LaBr_3$:Ce, CsI:Tl, BaF_2 and SrI_2:Eu [17]. These values are taken relative to NaI:Tl scintillator. PE of GGAG:Ce is about 2.5 times that of NaI:Tl scintillator. It can also be seen that GGAG:Ce has PE nearly 2 times that of CsI:Tl. Overall, highest absolute efficiency has been observed for GGAG:Ce scintillator. The errors associated with simulated efficiencies are within data points.

Table 4.3 Simulated TDE and PE (relative to NaI:Tl) of different scintillators having dimensions 18 mm × 18 × 10 mm (cuboid) and 24 mm × 19 mm (cylindrical) for gamma energy of 662 keV when source is placed 1 mm away.

Scintillator	Cuboid 18mm × 18mm × 10mm		Cylindrical 24 mm × 19 mm	
	TDE	PE	TDE	PE
GGAG:Ce	1.65	2.48	1.61	2.47
$LaBr_3$:Ce	1.23	1.21	1.26	1.29
NaI:Tl	1.00	1.00	1.00	1.00
CsI:Tl	1.16	1.45	1.19	1.54
BaF_2	1.24	1.54	1.26	1.56
SrI_2:Eu	1.19	1.32	1.19	1.34

After carrying out the simulations of absolute efficiency of GGAG:Ce and of different scintillators which have been already studied and reported, experiments were done with the available scintillators in the laboratory. The energy calibration plot of GGAG:Ce is shown in Figure 4.3. A good linearity can be seen for the energy range of 122 keV to 1332 keV.

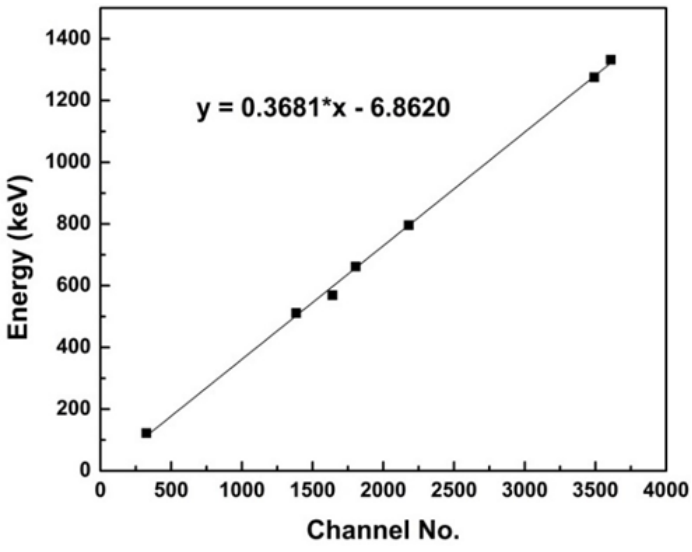

Figure 4.3 Energy calibration plot of GGAG:Ce detector.

Figure 4.4 shows the simulated and measured data for $LaBr_3$:Ce, NaI:Tl, CsI:Tl and BaF_2 scintillators of different geometries for 662 keV gamma energy and for source-to-detector separations up to 10 cm. A very good agreement has been found between simulated and measured

results. For example, measured TDE and PE of a 25.4 mm × 25.4 mm cylindrical $LaBr_3$:Ce scintillator is in excellent agreement with the values reported by Kumar *et al.* [13].

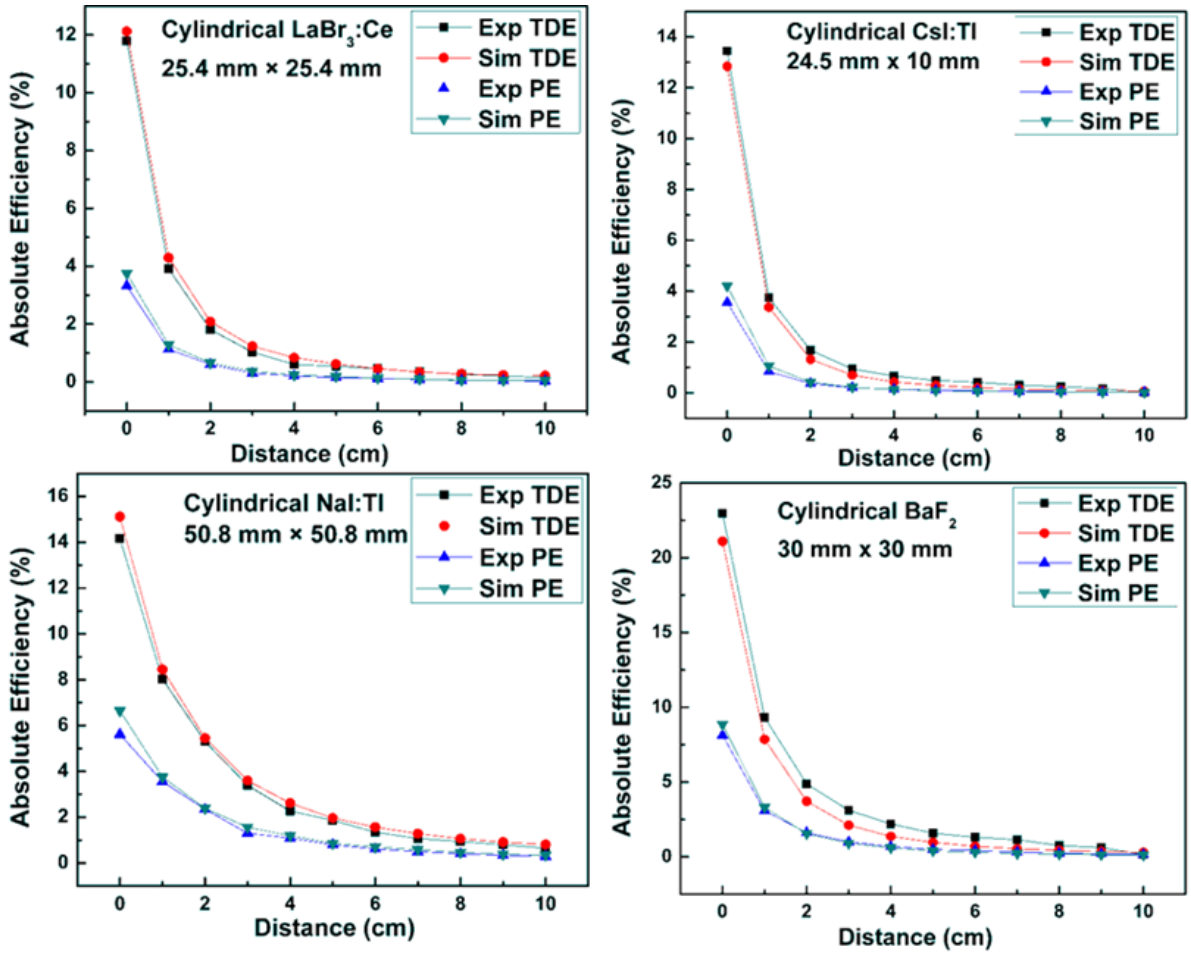

Figure 4.4 Simulated and measured TDE and PE curves of $LaBr_3$:Ce, NaI:Tl, CsI:Tl and BaF_2 scintillators for different source-to-detector separations for 662 keV gamma energy.

Figure 4.5 shows the measured and experimental TDE and PE values of cuboid and cylindrical GGAG:Ce scintillators grown in our lab. The errors associated with measured and simulated efficiencies are within data points. Again, our simulation results match fairly well with the measured efficiency values for both scintillator geometries. For GGAG:Ce scintillator of dimensions 18 mm × 18 mm × 10 mm, TDE and PE are found to be (9.22±0.01)% and (3.77±0.01)% respectively [17]. Similarly, for a cylindrical GGAG:Ce scintillator of dimensions 24 mm × 19 mm, the TDE and PE are found to be (19.79±0.01)% and (8.08±0.01)% respectively [17].

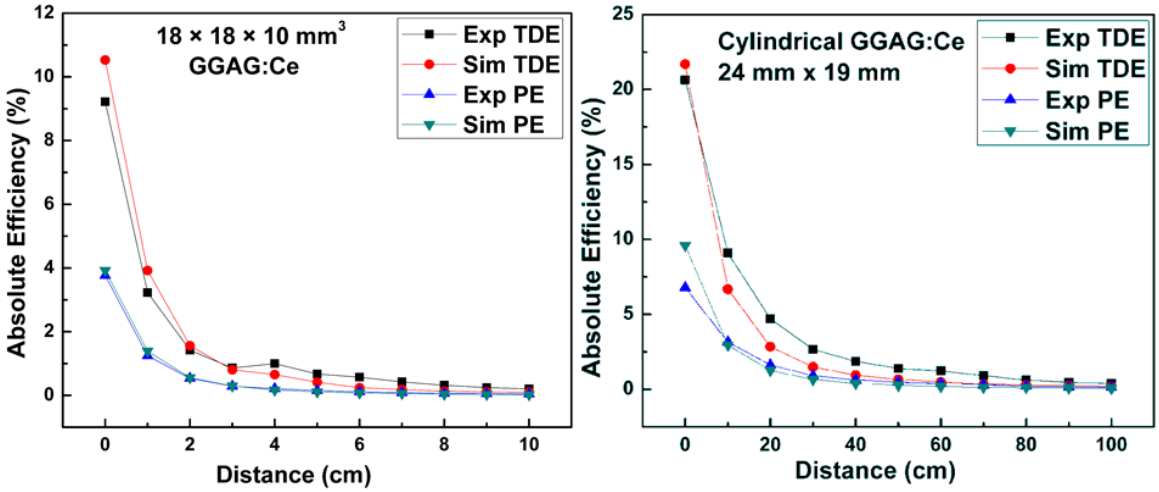

Figure 4.5 Simulated and measured TDE and PE of GGAG:Ce scintillator for two different geometries for different source-to-detector separations for 662 keV gamma energy.

4.5 Summary

Our detailed realistic GEANT4 simulations have clearly shown that GGAG:Ce has an absolute total detection and absolute photopeak efficiency better than that of $LaBr_3$:Ce, NaI:Tl, CsI:Tl, BaF_2 and SrI_2:Eu scintillators due to its high Z_{eff} and high density. When the performance of GGAG:Ce and CsI:Tl scintillators with similar dimensions are compared, GGAG:Ce found to be possess photo peak efficiency twice that of CsI:Tl. Thus, apart from having FOM higher than that of CsI:Tl in pulse shape discrimination (PSD) of alpha gamma radiations [18], the higher absolute efficiency of GGAG:Ce can further diversify its applicability in high efficiency detectors and detectors based on compact SiPMs. Future work include the growth of large volume of GGAG:Ce crystals and to determine energy dependent efficiency curves for gamma rays up to the energy of 20 MeV.

References of chapter 4

[1] Wang, Y. J., Patt, B. E., and Iwanczyk, J. S., High Efficiency CsI(TI)/HgI_2 Gamma Ray Spectrometers, *IEEE Trans. Nucl. Sci.* **42**, 601-605 (1995).

[2] Debertin, K., and Helmer, R. G., Gamma and X-ray spectrometry with semiconductor detectors, Elsevier Science, North Holland, Amsterdam (1988).

[3] Abbas, M. I., Analytical formulae for well-type NaI(Tl) and HPGe detectors efficiency computation, *Applied Radiation and Isotopes* **55**, 245–252 (2001).

[4] Tyagi, M., Meng, F., Koschan, M., Donnald, S. B., Rothfuss, H., and Melcher, C. L., Effect of codoping on scintillation and optical properties of a Ce-doped $Gd_3Ga_3Al_2O_{12}$:Ce scintillator. *J. Phys. D* **46**, 475302–475313 (2013).

[5] Iwanowska, J., Swiderski, L., Szczesniak, T., Sibczynski, P., Moszynski, M., Grodzicka, M., Kamada, K., Tsutsumi, K., Tsutsumi, Y., Yanagida, T., et al., Performance of cerium-doped $Gd_3Ga_3Al_2O_{12}$ (GAGG:Ce) scintillator in gamma-ray spectrometry, *Nucl. Instrum. Methods Phys. Res. Sect. A* **712**, 34 (2013).

[6] Kamada, K., Endo, T., Tsutumi, K., Yanagida, T., Fujimoto, Y., Fukabori, A., Yoshikawa, A., Pejchal, J., and Nikl, M., Composition engineering in cerium-doped $(Lu,Gd)_3(Ga,Al)_5O_{12}$ single-crystal scintillators, *Crystal Growth & Design* **11**, 4484–4490 (2011).

[7] Kamada, K., Yanagida, T., and Pejchal, J., Scintillator-oriented combinatorial search in Ce-doped $(Y,Gd)_3(Ga,Al)_5O_{12}$ multicomponent garnet compounds, *J. Phys. D: App. Phys.* **44**, 505104 (2011).

[8] Kamada, K., Yanagida, T., Endo, T., Tsutumi, K., Usuki, Y., Nikl, M., Fujimoto, Y., Fukabori, A., and Yoshikawa, A., 2 inch diameter single crystal growth and scintillation properties of Ce:$Gd_3Al_2Ga_3O_{12}$, *J. Cryst. Growth* **352**, 88–90 (2012).

[9] Tamagawa, Y., Inukai, Y., Ogawa, I., and Kobayashi, M., Alpha–gamma pulse-shape discrimination in $Gd_3Al_2Ga_3O_{12}$ (GAGG):Ce^{3+} crystal scintillator using shape indicator, *Nucl. Instrum. Methods Phys. Res. Sect. A* **795**, 192 (2015).

[10] Meng, F., Koschan, M., Melcher, C. L., and Cohen, P., Sintered pellets: a simple and cost effective method to predict the performance of GGAG:Ce single crystals, *Mat. Science Eng. B* 193, 2026 (2015).

[11] Knoll, G. F., Radiation Detection and Measurement, 4th Ed., John Wiley & Sons, New York, 243, 2010.

[12] Melcher, C. L., Manente, R. A., and Schweitzer, J. S., Applicability of barium fluoride and cadmium tungstate scintillators for well logging, *IEEE Trans. Nucl. Sci.* **36**, 1188-1192 (1989).

[13] Kumar, G. A., Mazumdar, I., and Gothe, D. A., Efficiency calibration and simulation of a $LaBr_3$(Ce) detector in close-geometry, *Nucl. Instrum. Methods Phys. Res. Sect. A* 610, 522–529 (2009).

[14] GEANT4 webpage: http://cern.ch/geant4.

[15] Tuli, J., Brookhaven National Lab Report, BNL-NCS-51655-02-Rev (2001).

[16] Hurtado, S., Garcia-Leon, M., and Garcia-Tenorio, R., GEANT4 code for simulation of a germanium gamma-ray detector and its application to efficiency calibration, *Nucl. Instrum. Methods Phys. Res. Sect. A* **518**, 764-774 (2004).

[17] Rawat, S., Tyagi, M., Kumar, G. A., and Gadkari, S. C., Efficiency studies on $Gd_3Ga_3Al_2O_{12}$:Ce scintillators: Simulations and measurements, *IEEE Trans. Nucl. Sci.* **65**, 2109-2113 (2018).

[18] Rawat, S., Tyagi, M., Netrakanti, P. K., Kashyap, V. K. S., Singh, A. K., Desai, D. G., Mitra, A., Kumar, G. A., and Gadkari, S. C. Pulse shape discrimination properties of $Gd_3Ga_3Al_2O_{12}$:Ce single crystal in comparison with CsI:Tl. *Nucl. Instrum. Methods Phys. Res., Sect. A* **840**, 186–191 (2016).

CHAPTER 5

Studies on effect of co-doping on PSD properties of GGAG:Ce scintillators

---

This chapter discusses the effect of co-doping on discrimination of alpha and gamma radiations in GGAG:Ce scintillator. The boron and calcium as co-dopants were chosen because of the maximum impact observed on the scintillation and timing properties of co-doped GGAG:Ce crystals. An approach to explain the PSD properties of GGAG:Ce scintillator with the help of optically stimulated luminescence (OSL) using infrared (IRSL), green (GSL) and blue (BSL) light emission, has been used for the first time.

5.1 Introduction

In addition to various applications, recently the GGAG:Ce scintillator has shown a huge potential in distinguishing alpha particles and gamma rays, with a high figure of merit (FOM) of about 3.42 among oxide scintillators as discussed in chapter-3 [1]. With promising scintillation properties discussed in chapter-1, GGAG:Ce is a good candidate for the charged particle identification [2]. The PSD properties depend on the quantification of the difference in pulse-shapes resulting from different scintillation decay kinetics of the excitation radiation inside the crystal [3]. Thus, in order to study the scintillation decay mechanism it is important to understand the electronic as well as defect structure of the crystal [4].

The reported work on PSD properties of GGAG:Ce single crystals in comparison with the conventionally used CsI:Tl scintillator has indicated that their scintillation decay times for alpha and gamma radiations have significantly different and opposite characteristics [1]. The average scintillation decay time of GGAG:Ce is 284 ns for alpha excitation as compared to the faster decay time of 108 ns for gamma rays. While in CsI:Tl crystals, the alpha excitation results in a faster average decay time of 600 ns compared to the slower decay of 1200 ns for gamma rays [1]. Accordingly, the oxide single crystal scintillators having a garnet structure such as YAG:Ce, LuAG:Ce and GGAG:Ce exhibit an opposite scintillation decay behavior compared to the halide scintillators such as NaI:Tl, CsI:Tl and $LaBr_3$:Ce when alpha and gamma radiations interact with them [5-12]. Studies on scintillation kinetics in halide scintillators have shown that the decay time of alpha particles is faster than that of gamma rays as it depends on activator concentration and indicates the presence of quenching due to their higher ionization density [13,14]. However, to the best of our knowledge, no detailed studies on ionization density dependent scintillation kinetics in garnet oxide scintillators are available so far. In addition, the role of co-doping on the PSD properties has been reported scarcely [4, 15] though the effect of co-doping on the scintillation properties have been studied extensively.

In this chapter, the effect of co-doping on discrimination of alpha and gamma radiations in GGAG:Ce scintillator has been investigated in detail. The boron and calcium as co-dopants were chosen because of the maximum impact observed on the scintillation and timing properties of co-doped GGAG:Ce crystals [4]. An approach to explain the PSD properties of GGAG:Ce scintillator with the help of optically stimulated luminescence (OSL) using infrared (IRSL), green (GSL) and blue (BSL) light emission, has been used for the first time.

5.2 Experimental details

GGAG:Ce single crystals used in the present work were grown using the Czochralski technique. The crystals were also grown incorporating co-doping of boron and calcium. The growth processes of these crystals have been discussed in detail in chapter-2. All three samples i.e, GGAG:Ce, GGAG:Ce,Ca and GGAG:Ce,B single crystals of dimensions 5×5×5 mm^3 were cut and polished from the grown single crystals. The samples were then coupled to a 1" Hamamatsu make PMT using optical grease. The decay time and PSD measurements were carried out with Am-Pu alpha and ^{137}Cs gamma sources. Decay curves for all the samples were obtained by taking the output from the anode of PMT using a 1 GHz Tektronics digital storage oscilloscope. PSD of alpha and gamma excitations in three samples was carried out by employing charge integration method in a CAEN (DT5790M) make dual channel, 12 bit desktop digitizer having a sampling rate of 250 MS/s. The collimated alpha source was directly mounted on the crystal to minimize the energy loss. A negative HV of 970 V was provided to the detector setup from the SHV connector of the digitizer. The integrated charges in short and long gates are processed by the digitizer with DPP-PSD firmware and different pulse-shapes of alpha and gamma radiations enable them to get discriminated. The time width of short gate (Q_S) and long gate (Q_L) were optimized by observing the effect of charge collection on the discrimination. Other parameters such as charge sensitivity, threshold, trigger hold-off, CFD fraction, pre-gate were also optimized to obtain the best possible discrimination.

In order to study the effect of co-doping on defect structure of GGAG:Ce samples, their thermo-luminescence (TL) and optically stimulated luminescence (OSL) using infrared laser and blue and green LEDs were studied. The samples were loaded on the Lexsyg research imaging TL-OSL-RF system, the most advanced TL/OSL reader system. A program routine to carry out TL and OSL of each sample was created. This routine incorporates pre-heating upto 350°C at 5°C/s and cooling is done upto 50°C. The samples were then irradiated by beta radiation (^{90}Sr) unit which provides a homogeneous irradiation field at a dose rate of about 0.1 Gy/s for 20 sec. Subsequently, TL was performed and the samples were heated upto 260°C at a rate of 5°C/s. The Lexsyg system facilitates a Hamamatsu PMT with standard bi-alkaline cathode having peak sensitivity at 420 nm for detection and light output measurements. After TL, preheating with instructions mentioned earlier was executed to get rid of filled trapped centres for IRSL and OSL measurements. A continuous mode 850 nm IRSL laser stimulation followed by preheating is done for each sample. Then, blue (458 nm) and green (525 nm) light LEDs stimulation for OSL excitation passing through a filter of 365

nm is performed. TL, IRSL and OSL data are acquired using LexStudio 2.0 data acquisition software.

5.3 Results and discussion

The dependence of scintillation kinetic mechanism of GGAG:Ce scintillator under different excitation densities cannot be solely credited to the non-radiative quenching of the emission as explained in halide scintillators [13,14]. The slow nature of alpha excitation decay time in GGAG:Ce scintillators indicate the presence of another factor which overpowers the higher ionization density quenching nature of alpha excitations [1]. The effect of co-doping on PSD properties adds some important results to understand this unresolved mechanism.

The scintillation decay curves measured with alpha and gamma radiations for GGAG:Ce, GGAG:Ce,Ca and GGAG:Ce,B single crystals have been plotted in Figure 5.1. Clearly, the difference in pulse shapes of alpha and gamma decay curves is maximum for B co-doped GGAG:Ce.

Figure 5.1 Alpha and gamma scintillation decay curves of boron and calcium co-doped GGAG:Ce samples having dimensions of 5×5×5 mm^3 with the crystal pictures in the inset.

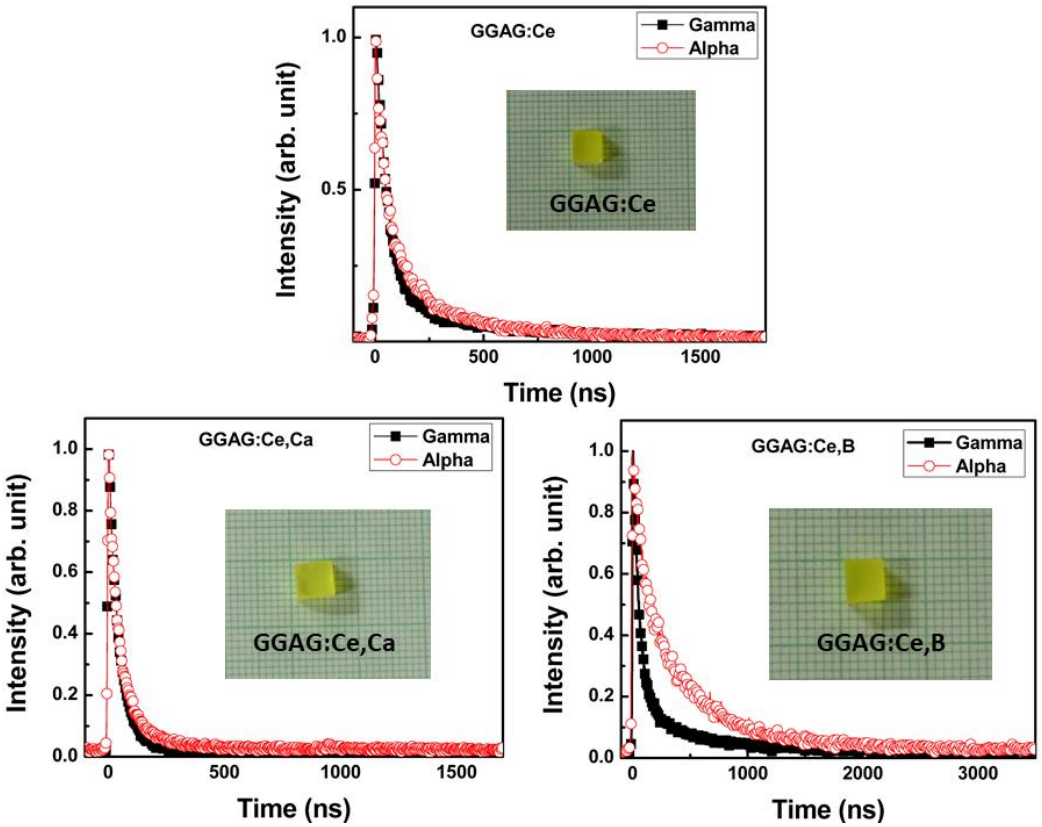

Table 5.1 illustrates the values of decay time calculated using Eq. (2.3), (2.4) and (2.5) by fitting the decay curves shown in Figure 5.1. The Ca co-doped crystal showed relatively fast average decay

time of about 120 ns for alpha excitation and 89 ns for the gamma excitation. The ratios of average decay times measured for alpha and gamma excitations were also calculated to have a rough estimate of the ability of GGAG:Ce, GGAG:Ce,Ca and GGAG:Ce,B single crystals in discrimination of these radiations. The ratio of average decay times of alpha and gamma gives an insight into the PSD ability of the crystal. The maximum difference in average decay times of alpha and gamma excitations was observed in B co-doped crystals. The α⁄γ ratio was calculated by measuring the photo-peak positions in the pulse-height spectrum with alpha and gamma sources and taking the ratio after dividing those with their relative energies 5486 keV and 662 keV respectively.

Table 5.1 Scintillation decay components for alpha and gamma excitations in GGAG:Ce, GGAG:Ce,Ca and GGAG:Ce,B single crystals and α⁄γ ratio for the light yield.

Sample	**Alpha**			**Gamma**				
	τ_1 **(ns)**	τ_2 **(ns)**	τ_{α_avg} **(ns)**	τ_1 **(ns)**	τ_2 **(ns)**	τ_{γ_avg} **(ns)**	$\frac{\tau_{\alpha\_avg}}{\tau_{\gamma\_avg}}$	α/γ **ratio**
GGAG:Ce	278 (58%)	47 (42%)	178	314 (28%)	53 (72%)	127	1.40	0.11
GGAG:Ce,Ca	219 (45%)	37 (55%)	120	245 (24%)	40 (76%)	89	1.35	0.10
GGAG:Ce,B	501 (70%)	98 (30%)	378	388 (25%)	61 (75%)	143	2.63	0.17

This ratio determines the quenching of emission due to higher ionization density by the charged particles and contributes as the major factor for making the decay time faster in halide crystals. This α⁄γ ratio was found to be the lowest in Ca co-doped crystals in spite of having the small difference in decay times. On the other hand, it was found to be highest in B co-doped crystals having the large difference in decay times. A correlation of α⁄γ ratio with non-proportionality and energy resolutions of the oxide scintillators has been reported recently [16]. However, we observe here that the poor α⁄γ ratio due to more quenching doesn't ensure to have better PSD ability. These results motivate us to understand the mechanism causing the PSD in garnet crystals which is different from that of reported in halide crystals [1].

The decay time measurements of B co-doped samples showed the largest difference for alpha and gamma radiations which led to its best PSD ability as shown in Figure 5.2 which is plotted by

calculating PSD using Eq. (2.8). But despite having the fastest decay time, Ca co-doped GGAG:Ce crystal exhibited poor PSD due to less difference in pulse-shapes generated by alpha and gamma excitations. This difference in pulse shapes of radiations is dependent on the scintillation kinetics of GGAG:Ce single crystal under different excitation densities. The major effect of co-doping has been observed on the defect structure of the crystal and the presence of "Ce" in higher valence state (Ce^{4+}) [4]. These results indicate that the ionization density induced quenching mechanism as reported in the case of alkali halides is not sufficient to explain the PSD properties of GGAG:Ce scintillator.

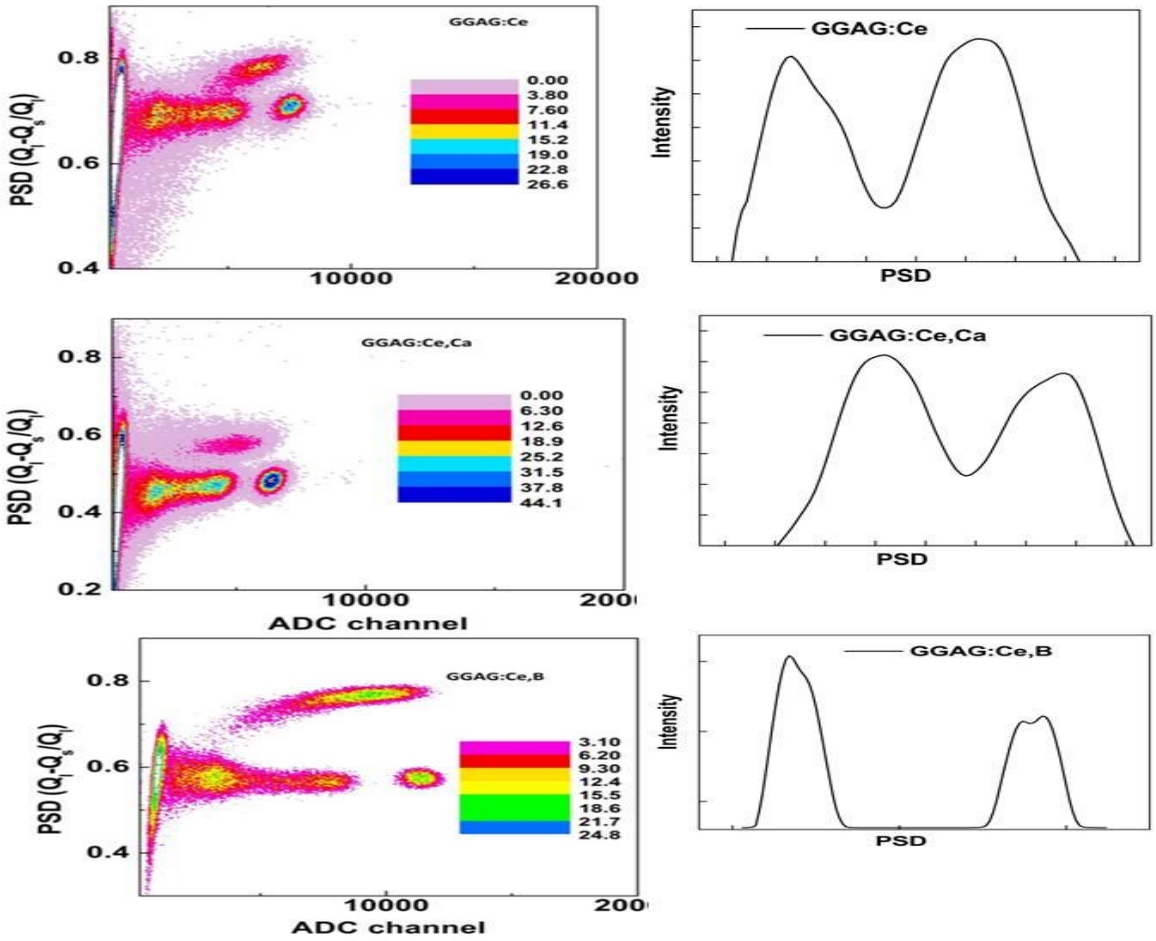

Figure 5.2 Effect of co-doping on alpha and gamma discrimination abilities of GGAG:Ce samples along with a 2-D cut along the PSD axis.

The defect centres also trap some of the excited charge carriers generated by alpha or gamma excitations to affect the emission from Ce^{3+} ions. These trapped carriers may be released either thermally or optically. Since the PSD properties have been measured at room temperature, the defect centres releasing charge carriers having energy equivalent to room temperature with such a decay rate that have significant contribution on the decay time should play the major role. The thermal

stimulated luminescence of the samples measured upto 260°C is shown in Figure 5.3(a) which clearly shows that Ca co-doping is more effective in reducing the shallow defect centres when compared to B co-doping.

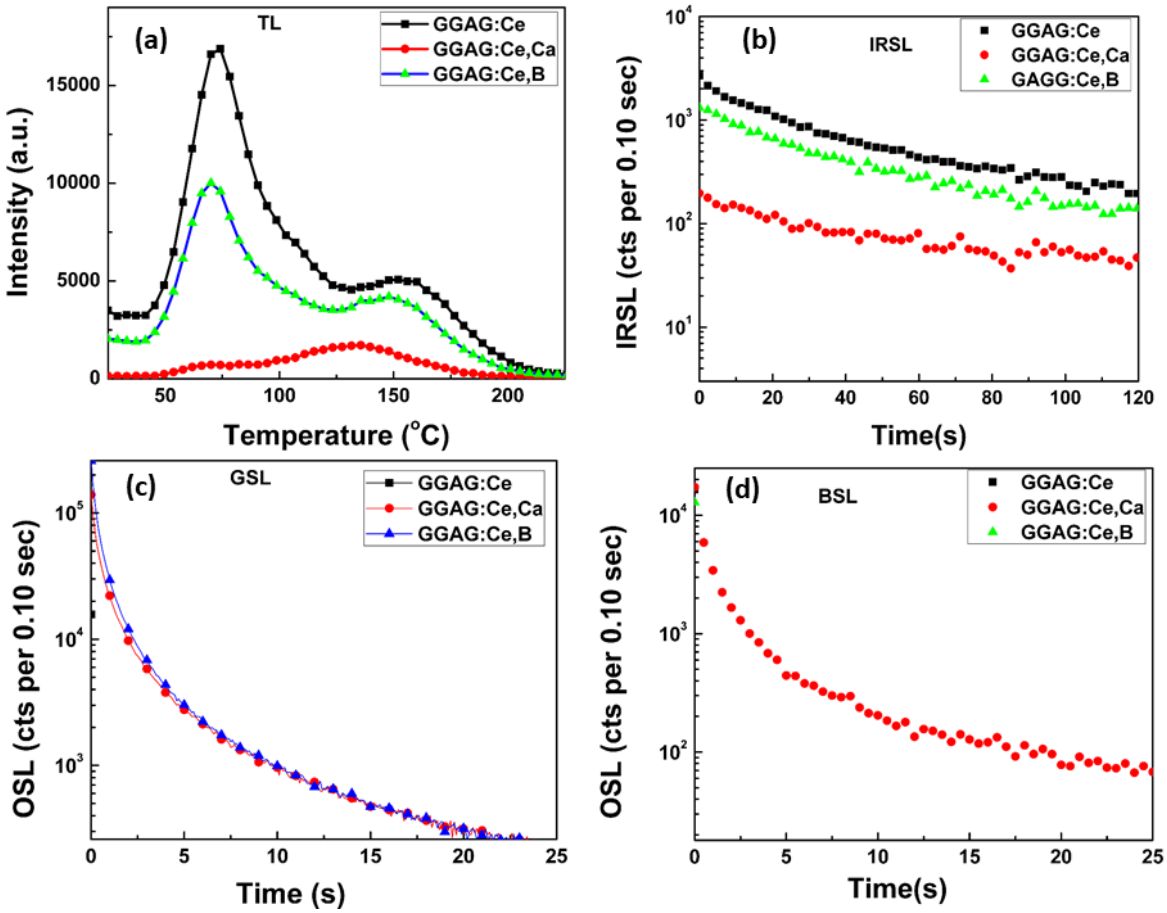

Figure 5.3 The luminescence intensity from the trap centres of GGAG:Ce, GGAG:Ce,Ca and GGAG:Ce,B scintillators measured from **(a)** Thermally stimulated **(b)** Infra-red light stimulated (IRSL), **(c)** Green light stimulated (GSL) and **(d)** Blue light stimulated (BSL).

More detailed investigations on TL properties related to scintillation kinetics in these crystals have been reported earlier [4]. However, these results do not explain why Ca co-doped crystals have poor discrimination ability in spite of having fast scintillation decay. The contribution from thermal noise makes it difficult to stimulate deeper trap centres. Therefore, to further understand the role of deeper defect centres in PSD properties of GGAG:Ce single crystal, we have used optical stimulation to release the deeper trapped centres. To measure the optically stimulated luminescence (OSL), the samples were first stimulated with low energy infrared laser pulse and the obtained emission has been plotted in Figure 5.3(b). The intensity of emitted light is maximum in GGAG:Ce

while it is least in Ca co-doped due to the presence of shallow defect centres as indicated by TL studies. When stimulated by green light LED, the emission was observed only in GGAG:Ce,Ca and GGAG:Ce,B crystals as shown in Figure 5.3(c). No emission of light is observed in GGAG:Ce indicating absence of deeper trap centres in the crystal. GSL highlights the presence of deep defect centres along with shallow centres in co-doped GGAG:Ce samples. Figure 5.3(d) shows the plot obtained using higher energy blue LED. Clearly, BSL provides better information about the presence of deeper trap centres where electrons are getting trapped in the forbidden band gap of GGAG:Ce single crystal. Only Ca co-doped crystals shows the luminescence when stimulated by blue LED. It confirms the presence of deeper trap centres in the vicinity of Ce^{3+} excited states in the forbidden band gap. These trap centres may immobilize the excited charge carriers and due to the presence of Ca^{2+} and Gd^{3+}, energy levels may lead to the non-radiative relaxation of the excitation to quench the emission [17]. Additionally, the presence of Ce in higher valence state i.e. Ce^{4+} in place of Ce^{3+} has been also observed to be in higher concentration in Ca co-doped crystals [14]. It leads to the Ca co-doped crystals to have lesser light yield and faster decay times. The contribution of defect centres in slower decay time component due to delayed recombination has been observed in GGAG:Ce [18] and can be used in future to explain the thermal ionization effect on the luminescence in B and Ca co-doped GGAG:Ce materials also.

However, the presence of defect centres should have more influence on the scintillation kinetics when irradiated with gamma in comparison to alpha excitation having lesser penetration length. The role of higher excitation density on the contribution from the trap centres is not possible to explain with the available knowledge and experimental results. These results on the effect of co-doping on PSD abilities indicate that unlike halide crystals, the defect centres also play an important role in affecting the scintillation decay kinetics when excited by alpha radiation having higher ionization density of excited charge carriers in comparison with the gamma radiations. The contribution from trap centres to the decay times may compete with other processes like energy transfer from the host and ionization density quenching in order to determine the PSD abilities of these scintillators. It is also observed that the higher concentration of shallow trap centres in GGAG:Ce crystals and higher concentration of deep trap centres in GGAG:Ce,Ca crystals lead to the poor α/γ ratio along with the poor discrimination ability while GGAG:Ce,B crystals were found to have the best discrimination abilities.

The “B” co-doping also improves the energy non-proportionality and self-absorption in addition to increase the activator Ce concentration in trivalent (Ce^{3+}) valence state [19]. Therefore

the slower decay time with alpha irradiation and effect of co-doping on PSD properties of garnet crystals can be assigned to a cumulative effect. These results on the effect of co-doping on PSD properties are valuable addition to explain the mechanism and more experiments on the growth conditions and different co-dopants are in progress for further understanding which may be applied to other garnet based scintillators as well. This understanding may help in a systematic designing of the materials according to the application requirements.

5.4 Summary

The pulse-shape discrimination capabilities were observed to depend on the presence of co-doping in GGAG:Ce scintillators. B co-doping in GGAG:Ce single crystal was found to have better PSD properties in comparison to Ca co-doped crystals while α/γ ratio indicates the maximum quenching in Ca co-doped crystals. The effect of co-doping has been found to be an effective tool in order to understand the scintillation decay mechanism and role of defect centres [20]. The optically luminescence stimulated by different energies was used to understand the role of deeper trap centres on the light yield and scintillation kinetics. The IRSL, GSL and BSL emissions confirm the presence of deeper trap centres in Ca co-doped crystals while Ce only doped crystals have more shallow traps. Unlike halide scintillators, the alpha and gamma excitations in GGAG:Ce cannot be solely attributed to the ionization density induced quenching to explain the opposite trend of scintillation kinetics for the charged particles.

References of chapter 5

[1] Rawat, S., Tyagi, M., Netrakanti, P. K., Kashyap, V. K. S., Singh, A. K., Desai, D. G., Mitra, A., Kumar, G. A., and Gadkari, S. C., Pulse shape discrimination properties of $Gd_3Ga_3Al_2O_{12}$:Ce single crystal in comparison with CsI:Tl. *Nucl. Instrum. Methods Phys. Res., Sect. A* **840**, 186–191 (2016).

[2] Tyagi, M., Singh, A. K., Singh, S. G., Desai, D. G., Patra, G. D., Sen, S., and Gadkari, S. C., Improvement of the scintillation properties of $Gd_3Ga_3Al_2O_{12}$:Ce,B single crystals having tailored defect structure *Phys. Stat. solidi-Rapid Research Letter* **9,** 530-534 (2015).

[3] G. F. Knoll, Radiation Detection and Measurement, John Wiley & Sons, New York, *4th Ed.,* 2010.

[4] Tyagi, M., Meng, F., Koschan, M., Donnald, S. B., Rothfuss, H., and Melcher, C. L., Effect of codoping on scintillation and optical properties of a Ce-doped $Gd_3Ga_3Al_2O_{12}$:Ce scintillator. *J. Phys. D* **46**, 475302 (2013).

[5] Kamada, K., Yanagida, T., and Pejchal, J., Scintillator-oriented combinatorial search in Ce-doped $(Y,Gd)_3(Ga,Al)_5O_{12}$ multicomponent garnet compounds, *J. Phys. D: App. Phys.* **44**, 505104 (2011).

[6] Wu, Y. T., Luo, J. L., Nikl, M., and Ren, G. H., Origin of improved scintillation efficiency in $(Lu,Gd)_3(Ga,Al)_5O_{12}$:Ce multicomponent garnets: An X-ray absorption near edge spectroscopy study, *Appl. Phys. Lett. Mater.* **2**, 012101 (2014).

[7] Kamada, K., Endo, T., Tsutumi, K., Yanagida, T., Fujimoto, Y., Fukabori, A., Yoshikawa, A., Pejchal, J., and Nikl, M., 2011. Composition engineering in cerium-doped $(Lu,Gd)_3(Ga,Al)_5O_{12}$ single-crystal scintillators, *Crystal Growth & Design* **11**, 4484.

[8] Bartle, C. M., A study of (n,p) and (n,α) reactions in NaI(Tl) using a pulse-shape-discrimination method, *Nucl. Instrum. Methods* **124**, 547 (1975).

[9] Winyard, R. A., Lutkin, J., and McBeth, G. W., Pulse shape discrimination in inorganic and organic scintillators, *Nucl. Instrum. Methods* **95**, 141-153 (1971).

[10] Crespi, C. L., Camera, F., Blasi, N., Bracco, A., Brambilla, S., Million, B., Nicolini, R., Pellegri, L., Riboldi, S., Sassi, M., et al., Alpha–gamma discrimination by pulse shape in $LaBr_3$:Ce and $LaCl_3$:Ce, *Nucl. Instrum. Methods Phys. Res. Sect. A* **602**, 520 (2009).

[11] Auffray, E., Augulis, R., Fedorov, A., Dosovitskiy, G., Grigorjeva, L., Gulbinas, V., Koschan, M., Lucchini, M., Melcher, C. L., Nargelas, S., et al., Excitation transfer engineering in Ce-doped oxide crystalline scintillators by codoping with alkali-earth ions, *Phys. Status Solidi A*

215, 1700798 (2018).

[12] Sidletskiy, O., Arhipov, P., Tkachenko, S., Zelenskaya, O., Vasyukov, S., Moretti, F., Dujardin, C., Drastic scintillation yield enhancement of YAG:Ce with carbon doping, *Phys. Status Solidi A* **215**, 1800122 (2018).

[13] Kudin, A. M., Sysoeva, E. P., Sysoeva, E. V., Trefilova, L. N., and Zosim, D. I., Factors which define the α/γ ratio in CsI:Tl, *Nucl. Instrum. Methods Phys. Res. Sect. A* **537**, 105 (2005).

[14] Dinca, L. E., Dorenbos, P., de Haas, J. T. M., Bom, V. R., and Van Eijik, C. W. E., Alpha–gamma pulse shape discrimination in CsI:Tl, CsI:Na and BaF_2 scintillators, *Nucl. Instrum. Methods Phys. Res. Sect. A* **486**, 141-145 (2002).

[15] Barta, J., Cuba, V., Jary, V., Beitlerova, A., Panek, D., Parkman, T. and Nikl, M., Photoinduced preparation of bandgap-engineered garnet powders, *IEEE Trans on Nucl Science* **65**, 2184-2190 (2018).

[16] Wolszczak, W., and Dorenbos, P., Nonproportional response of scintillators to alpha particle excitation. *IEEE Trans on Nucl Science* **64**, 1580 (2017).

[17] Tyagi, M., Rothfuss, H. E., Donnald, S. B., Koschan, M., and Melcher, C. L., Effect of co-doping on the radiation hardness of $Gd_3Ga_3Al_2O_{12}$: Ce scintillators, *IEEE Trans on Nucl Science* **61**, 297-300 (2014).

[18] Mihokova, E., Jary, V., Schulman, L. S., and Nikl, M., Low temperature delayed recombination decay in complex oxide scintillating crystals, *IEEE Trans Nucl. Science* **61**, 257 (2014).

[19] Donnald, S. B., Tyagi, M., Rothfuss, H., Meng, F., Hayward, J. P., Koschan, M., and Melcher, C. L., The effect of B^{3+} and Ca^{2+} co-doping on factors which affect the energy resolution of $Gd_3Ga_3Al_2O_{12}$:Ce, *IEEE Trans. Nucl. Sci.* **60**, 4002 (2013).

[20] Rawat, S., Tyagi, M., G. Anil Kumar, Gadkari, S. C. and Kim, H. J., Comprehending the role of defect structures in pulse-shape discrimination and scintillation kinetics for $Gd_3Ga_3Al_2O_{12}$:Ce single crystals (2019) [To be submitted].

CHAPTER 6

A novel versatile phoswich detector consisting of two single crystals to discriminate various kinds of radiation

---

A phoswich detector having a novel combination of GGAG:Ce and CsI:Tl single crystals, both non-hygroscopic, is proposed for detecting charged particles, neutrons and gamma rays in a mixed field of radiation. This combination is chosen because of their opposite behavior in decay times of alpha and gamma radiations. A high FOM for alpha and gamma radiations for any individual scintillator has been observed by this phoswich detector.

6.1 Introduction

Scintillation detectors are being used as a vital component for various current and advanced technology developments. The single crystal scintillators have been proven to be advantageous over other forms of materials in various applications including academics as well as industries like medical, security, nuclear, etc [1,2]. The demand for new scintillating materials with improved performance characteristics are continuously increasing with the applications in various fields [3,4]. The finding of new materials is also associated with advancement of photo-sensors and data acquisition systems. No single material has required properties to be used in all applications. An appropriate material is selected for a particular application based on the types of incident radiation, intensity of radiation, requirement of size and the desired output, etc. For different kinds of radiation like α, β, γ, heavy charged particles, neutrons, etc., different scintillating materials are usually deployed based on the type of interaction and conversion into a measurable signal [5]. Neutral particles like neutrons require special materials consisting of atoms with significant values of the capture cross-section. Alpha and heavy charged particles require thin scintillators while gamma radiations need larger size with higher stopping efficiency [6]. However, various applications in general involve mixed field of different kinds of radiation. For example, neutron emission is generally associated with gamma radiation [7].

For detecting a specific kind of radiation in a fixed field of radiation, PSD and PHD methods are employed as discussed in chapter-2. PSD method makes use of the slow component dependence on the incident radiation type. PSD can be achieved by many scintillators discussed in chapter-3. In some of the alternate approaches to obtain the incident radiation dependent decay time, a new class of detectors has been proven to be useful for discriminating different kinds of radiation. These detectors are fabricated by employing a sandwich/combination of two or more dissimilar materials having different pulse-shape characteristics and coupled to a common photo-sensor. These are called phoswich detectors that include a combination of scintillating materials like organic, inorganic crystalline, thin films, etc. These detectors have found various applications in routine as well as in advanced detector systems for particle spectrometry, simultaneous detection of beta and gamma radiations, background suppressed spectroscopy for low energy radiations, etc. A different response of the combination of scintillating materials for a same type of radiation also has an ability to provide a depth of interaction (DOI) information which has added an additional dimension in the medical imaging applications. Therefore, the advanced imaging systems are also being developed based on the phoswich scintillators. Various phoswich detectors have been reported earlier by employing gas

detectors, organic plastic scintillators, thin films, polycrystalline materials, and single crystals, etc. in combination with the similar phase material or single crystals [8-20]. However, the detectors fabricated from different phases other than single crystals suffer from with the problem of poor efficiencies especially at higher gamma energies. The single crystals have various advantages over other scintillating materials and therefore the phoswich combination of single crystal scintillators lead to the best results in various applications. However, the difference in refractive indices limits the choice of crystals to be optically coupled together. Additionally, the emission of light from the first crystal needs to be effectively transmitted through the second crystal without significant absorption/excitation. Some of the promising combinations have single crystals which are hygroscopic in nature and need to be encapsulated which limits their applications. Moreover, the detection of thermal neutrons requires the presence of atoms like Li, B and Gd, etc. that have a high thermal neutron capture cross-section that further limits the choice of using single crystals phoswich detectors to discriminate neutrons in addition to charged particles and gamma radiations.

In this chapter, we set up a novel phoswich design comprising of CsI:Tl and GGAG:Ce,B single crystal scintillators and employing a digitizer for the individual detection of alpha, beta, gamma and neutron radiation.

6.2 Experimental details

The single crystals of $Gd_3Ga_3Al_2O_{12}$ doped with Ce and co-doped with B were grown by the Czchrolaski technique. A disc of about 20 mm diameter and 1 mm thickness was cut and optically polished. It was kept in contact with a commercially available CsI:Tl scintillator of ~20 mm^3 having good PSD properties. An aluminized Mylar of about 6 micron thickness was used to cover the front of GGAG:Ce,B scintillator. This combination was mounted on a Hamamatsu PMT using optical grease. The schematic of the phoswich design is shown in Figure 6.1 (a). An Am-Pu alpha source was directly coupled to an aluminized mylar covered GGAG:Ce,B disc and was collimated using Al foil such that all radiation falls only on the disc. A ^{137}Cs (662 keV) gamma source was kept in front of the phoswich detector such that it deposits its energy in both scintillators depending on their nature and stopping powers. For scintillation decay measurements, the anode signals from PMT were recorded in a 1 GHz Tektronics digital storage oscilloscope. PSD studies were carried out by using a CAEN make desktop digitizer having a 250 MHz sampling rate employing charge integration technique.

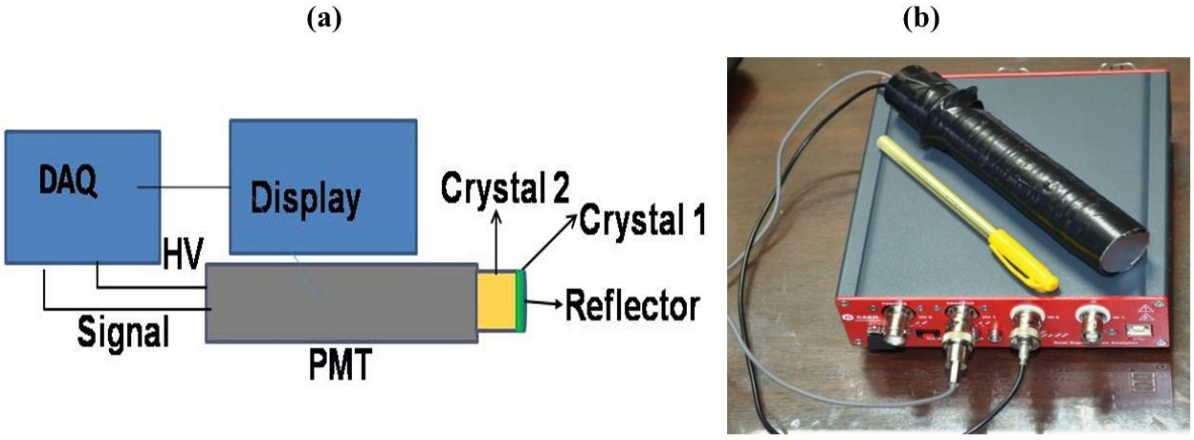

Figure 6.1 (a) The schematic of a phoswich detector and **(b)** Actual setup of a versatile phoswich detector consisting of a combination of GGAG:Ce,B and CsI:Tl single crystals.

Here the HV for PMT was also provided by the digitizer. Various short and long gate settings were used to study the effect of charge collection on the discrimination and were subsequently optimized. The developed portable setup used for PSD studies employing phoswich and digitizer is shown in Figure 6.1 (b). All these measurements have been carried out with the identical setup under the optimized conditions for a better comparison. However the performance can be further improved with more advance techniques.

6.2.1 Setup of a versatile phoswich detector

A novel combination of two single crystal scintillators having different pulse-shape characteristics of discriminating alpha, beta, gamma and neutron was setup. The main properties of $Gd_3Ga_3Al_2O_{12}$:Ce,B and CsI:Tl single crystals have been listed in Table 6.1. The GGAG:Ce scintillators were co-doped with B due to the significant improvement of the scintillation characteristics including light yield, self-absorption of scintillation light output (LO), radiation hardness and improvement of energy resolution as reported by Tyagi *et al* [21]. From now onwards, in this chapter these two scintillators will be referred as GGAG and CsI respectively. The emission of light from the front GGAG crystal peaking at around 550 nm lies in the transmission region of the CsI crystal coupled to the PMT. The difference in the refractive indices is also not significant. A typical photograph of the complete setup is shown in Figure 6.1 (b). This combination also scores over the existing combinations methods by using a Gd based garnet single crystal that makes it possible to efficiently detect neutrons in presence of other radiation. The high capture cross-section

of ^{155}Gd and ^{157}Gd isotopes ensures very high stopping efficiencies of thermal neutrons even in a thin disc of the GGAG crystal.

Table 6.1 The important properties of both crystals used to build the phoswich detector.

First crystal/Second Crystal	**GGAG(Ce)/CsI(Tl)**
Decay times (ns)	55/1000 ns
Peak Emission	550/550 nm
Light Yield	55000/55000 ph/MeV
Refractive index	1.89/1.8
Physical property	Non-hygroscopic / Slightly hygroscopic Encapsulation not required

6.3 Results and discussion

Figure 6.2 show the difference in the scintillation decay times measured with alpha and gamma radiations incident on CsI:Tl and GGAG:Ce,B single crystals respectively.

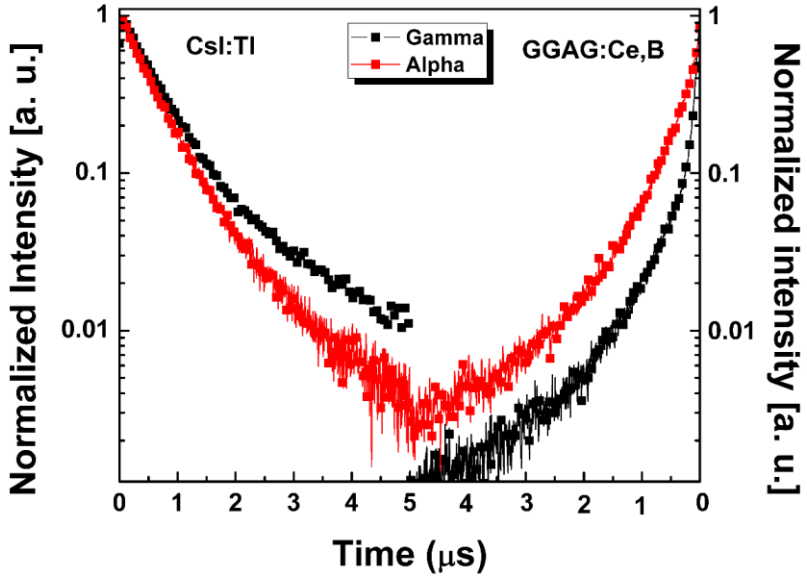

Figure 6.2 Scintillation decay curves measured with alpha and gamma irradiations on **(a)** CsI:Tl and **(b)** GGAG:Ce,B single crystals.

The scintillation decay measured for single crystals of CsI:Tl and GGAG:Ce,B have more than one exponential components. The ratio of these components gets significantly affected by the mode

of excitation. The charged particles like alpha generate higher ionization excitation density that consequently affects the decay kinetics of the relaxation. This higher ionization density usually quenches the emission and makes the decay time faster in comparison with that measured with gamma radiation as observed in CsI:Tl single crystals. However, the effect was found to be opposite in GGAG crystals where alpha radiation slows down the scintillation decay in comparison to gamma radiation as seen in the Figure 6.2 (b) and also reported by Rawat *et al* [22]. This opposite manner of the decay time dependence on mode of excitation in addition to the large difference of the mean time observed for both the crystals, can have a significant effect on the scintillation mechanism of the phoswich combination. Therefore, the phoswich combination was fabricated by coupling the fast GGAG scintillator in front followed by the CsI crystal having relatively slower decay time at the back end. The alpha radiation has been effectively stopped in the front crystal even with a thickness as small as less than 1 mm. The light emitted in the front crystal peaking at around 550 nm passes through the second crystal effectively without significant attenuation. Figure 6.3 represents the scintillation decay curve measured with the GGAG:Ce,B/CsI:Tl phoswich irradiated with the alpha and gamma sources.

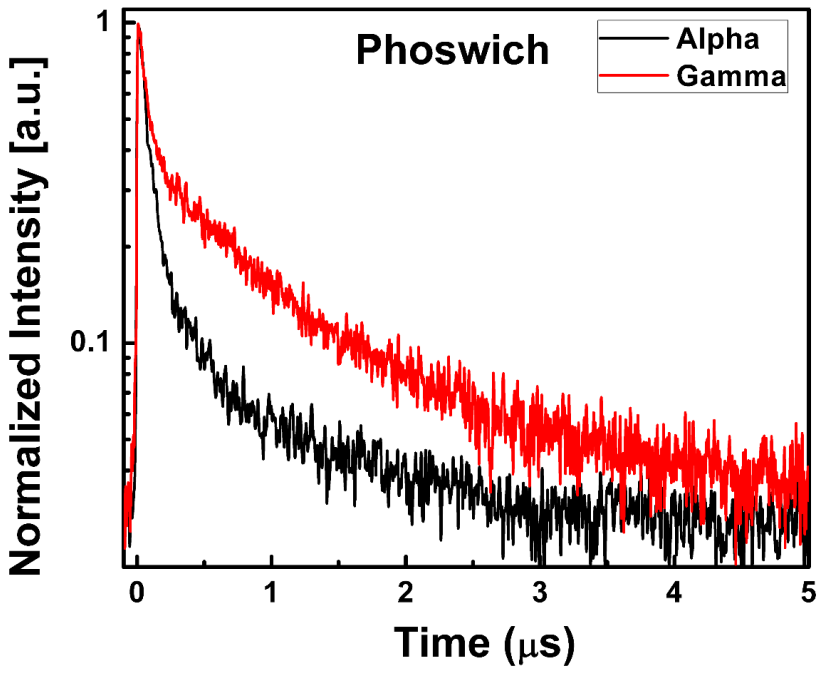

Figure 6.3 The scintillation decay curves measured with alpha and gamma radiations falling on GGAG:Ce,B/CsI:Tl phoswich detector.

The change in the relative ratio of the fast and slow component of the decay curve with the types of radiation cause the difference in the decay curves for different types of radiation. The

difference of decay times was observed to have significantly improved in comparison with that measured with single scintillator of GGAG or CsI. The fitted decay components (τ) along with their relative amplitude ratio (A) for alpha and gamma along with the mean decay time of the individual scintillator and GGAG:Ce,B/CsI:Tl phoswich are presented in Table 6.2. The mean decay times has been calculated using Eq. (2.6). The difference in mean life times of alpha and gamma radiations gives us a general idea on the PSD capability of the scintillator.

The decay from the front crystal has the contributions from alpha and gamma irradiations while the CsI crystal mainly has decay time contribution due to gamma irradiations only. The combination generates a combined effect on the decay times and improves the difference of the mean decay times measured with different kinds of irradiation. This dependence can be utilized in various pulse-shape discrimination techniques to distinguish different kinds of incident radiation.

Table 6.2 The scintillation decay times and relative ratio for alpha and gamma irradiations on individual single crystals and phoswich.

		Decay components					**Mean Decay time (ns)**	
		Alpha		**Gamma**			**Alpha**	**Gamma**
GGAG:Ce,B	τ (ns)	104	501	61	488		422	275
	A	0.58	0.48	1.1	0.14			
CsI:Tl	τ (ns)	320	762	778	3506		650	1966
	A	0.35	0.44	0.67	0.12			
Phoswich	τ (ns)	73	776	46	712	2982	469	1719
	A	0.007	0.0009	0.004	0.003	0.0007		

We have made a portable setup by employing a desktop digitizer which is based on the charge integration method where the charges are collected and integrated in short and long gates based on the decay times. A photograph of the actual setup is shown in Figure 6.1 (b). Figure 6.4 (a) and (b) represents the discrimination of alpha and gamma radiations by employing GGAG and CsI crystals respectively. The PSD parameter as defined in Eq. (2.8) and measured by integrating the charges in short and long gates is plotted on X-axis and Y-axis represents the ADC channel numbers which can be calibrated for the energies. The alpha irradiations on GGAG crystals give higher values of

PSD due to the slower decay in comparison with that observed for gamma irradiations. However, in case of CsI crystals the lower band represents the alpha irradiations.

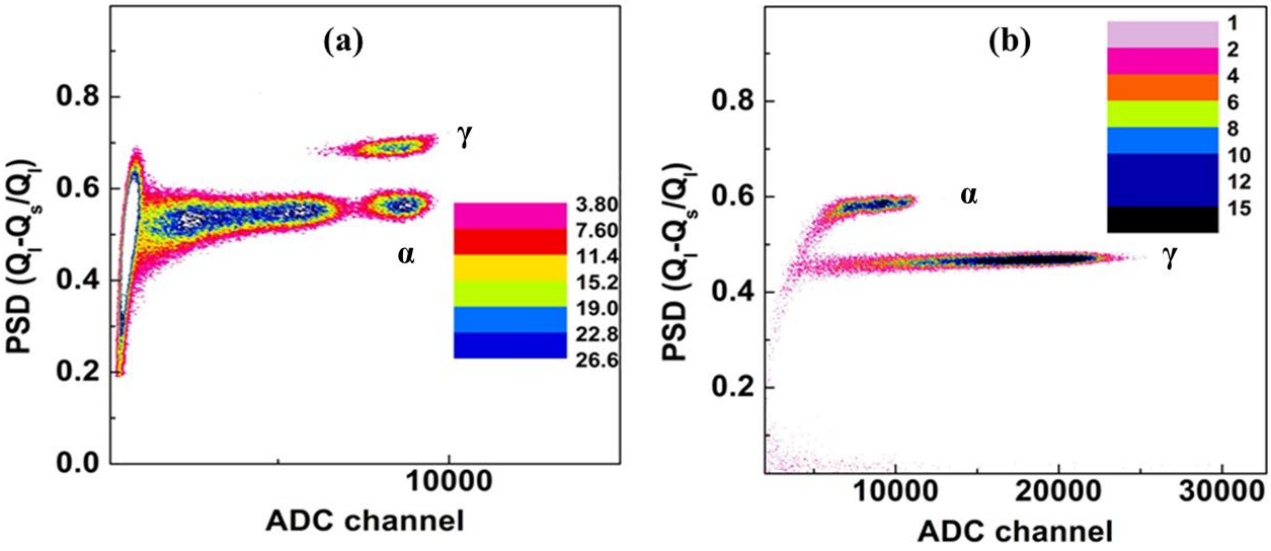

Figure 6.4 PSD parameters measured for alpha and gamma irradiations on **(a)** GGAG and **(b)** CsI single crystals.

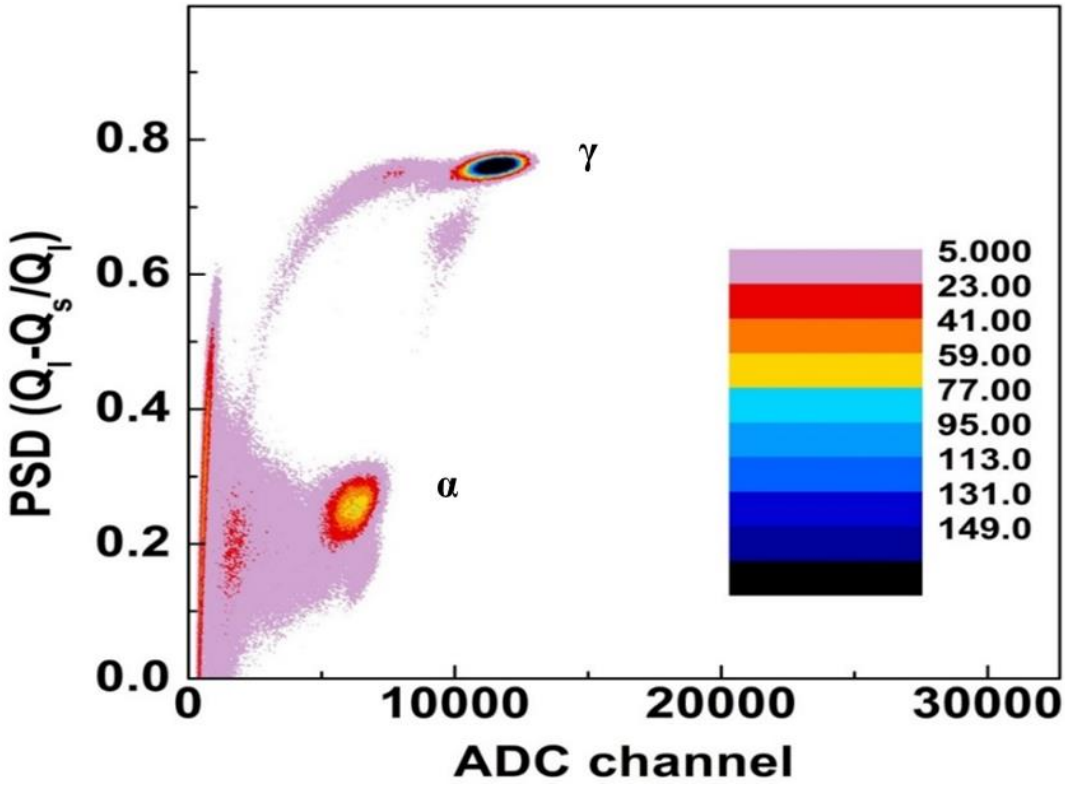

Figure 6.5 Alpha and gamma discrimination ability of the GGAG/CsI phoswich combination presented by measuring the PSD ratio method.

Figure 6.5 presents the discrimination ability of our phoswich combination. It can be observed from the figure that the difference between alpha and gamma bands has become more than double than what is measured with individual single scintillators. The selection of short and long gates plays a vital role in the increment of PSD power of phoswich detector. Short gate is adjusted such that alpha radiations gets completely absorbed in the GGAG single crystal with less contribution from gamma radiations. Hence, in Figure 6.5 the lower PSD value in Y axis is mainly due to alpha radiation contribution in the decay time of GGAG scintillator. While the long gate contains the contribution due to gamma irradiation in CsI scintillator resulting in the higher PSD value in Y-axis. Therefore, this opposite behaviour in decay times of alpha and gamma radiations in GGAG and CsI crystals observed in Figure 6.2 has stemmed into the overall improvement of PSD ability of this GGAG/CsI phoswich detector. It may also be noted that these measurements were carried out with the simultaneous irradiation from alpha and gamma sources and data were recorded online. Further data processing and use of more advanced techniques may further improve the discrimination.

Figure 6.6 shows the discrimination ability for gamma radiations falling on the front and back crystals of the phoswich detector by plotting of the PSD parameters and ADC channel numbers.

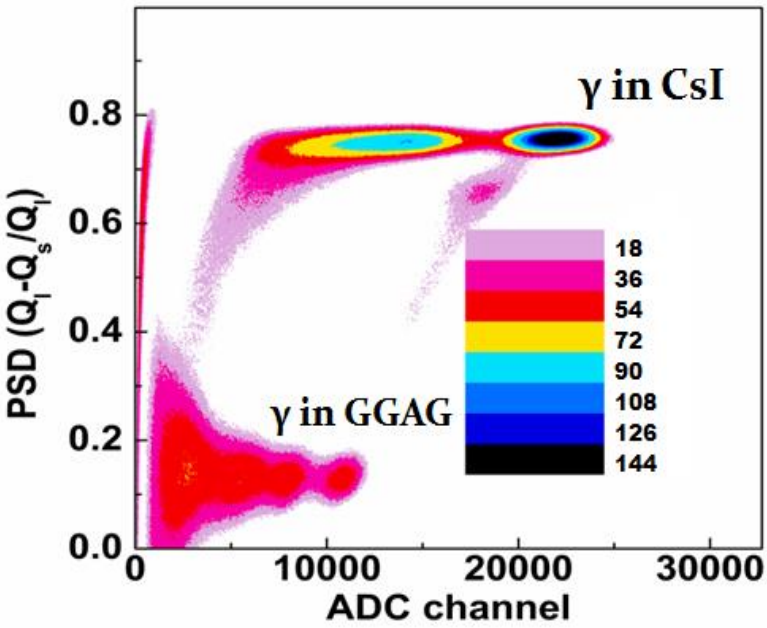

Figure 6.6 The PSD parameter for gamma radiation falling on the phoswich detector. The interaction of gamma in front and back crystals is well discriminated.

A large discrimination for gamma radiations is observed and it can also be attributed to the opposite behavior of alpha and gamma irradiations in GGAG and CsI scintillators. This excellent discrimination of the similar type of radiation (gamma) interacting in the front and back crystals opens a large scope of applications. One of the major applications is the depth of interaction (DOI) information in the imaging applications which would improve the spatial resolution significantly. Therefore, the phoswich combination could also be used for radio-xenon measurements for nuclear applications [23]. The gamma-gamma discrimination also makes it possible to fabricate a Compton suppressed detector to detect low energy gamma radiation in presence of high energies which is otherwise not possible to detect due to merging in the Compton backgrounds. This further increases the application of present versatile phoswich combination. Moreover, the presence of Gd i.e. ^{155}Gd and ^{157}Gd isotopes in GGAG with very high thermal neutron capture cross-section can efficiently stop neutrons in a very thin disk. These isotopes generate low energy conversion electrons, X-rays and continuum gamma through (n, γ) reaction during the de-excitation after the interaction with neutrons. We have recently reported the performance characteristics of GGAG scintillators for thermal neutrons [24].

Due to the excellent discrimination of these neutron induced gamma in GGAG crystals with the background gamma mainly depositing energy in relatively larger back crystals makes it a promising candidate to discriminate neutrons in mixed field radiations. Therefore, this phoswich combination numerous applications for simultaneous detection of different kinds of radiation. Figure 6.7 exhibits the 2-D plot of the PSD curves along the X-axis by plotting the PSD values. The *FOM* describes the ability of the detector to discriminate different radiations. Figure 6.7 shows the improvement of FOM by more than twice in phoswich detectors in comparison with that of observed in CsI or GGAG crystals individually.

Table 6.3 gives the FOM values of individual as well as of phoswich detector calculated from the Eq. (2.7). It may be noted that these FOM were measured for both crystals and phoswich combination by using an identical setup (digitizer) and method. There are different methods and setups have been reported for the measurement of FOM. It can be certainly improved further with the help of more optimized electronics and data acquisition systems.

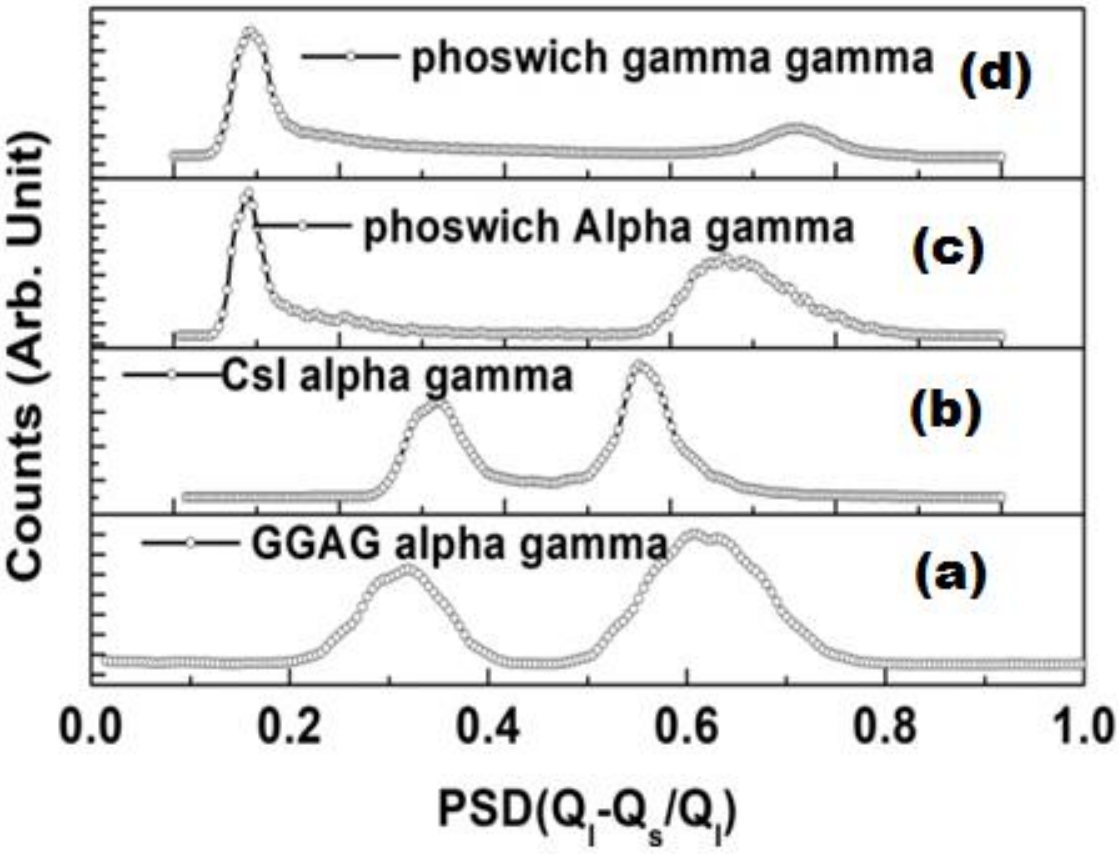

Figure 6.7 The PSD parameters in terms of FOM for the discrimination of **(a)** alpha and gamma on GGAG crystal **(b)** alpha and gamma on CsI crystal **(c)** alpha and gamma on phoswich combination, and **(d)** gamma and gamma falling on phoswich combination.

Table 6.3 The FOM values of GGAG, CsI and phoswich detectors for alpha- gamma and gamma-gamma separation.

Crystal	Alpha-Gamma	Gamma-Gamma
GGAG:Ce,B	1.24	--
CsI:Tl	1.73	--
Phoswich	3.21	5.09

6.4 Summary

A novel phoswich detector having a combination of two non-hygroscopic single crystal scintillators comprising of garnet and halide was developed to detect various kinds of radiation including alpha, gamma neutrons, etc. The large difference and opposite behaviour of decay times of alpha and gamma radiations in GGAG:Ce and CsI:Tl crystals significantly improved the

discrimination ability of the phoswich. Therefore, this novel phoswich combination has an enhanced "figure-of-merit" to discriminate different radiations by more than 100% in comparison to when crystals are used individually. In addition, the gamma radiation interaction in front and back crystals could be well discriminated that enables to measure depth of interaction (DOI) useful in imaging applications. This versatile phoswich detector also makes it possible to discriminate thermal neutrons due to the presence of Gd in the front crystal.

References of chapter 6

[1] Johnson, J. A., Zhuravleva, M., Stand, L., Chakoumakos, B. C., Yuntao Wu, Y., Greely, I., Rutstrom, D., Koschan, M., and Melcher, C. L., Discovery of New Compounds and Scintillators of the A_4BX_6 Family: Crystal Structure, Thermal, Optical, and Scintillation Properties. *Cryst. Growth Des.* **18**, 5220–5230 (2018).

[2] Aupiais, J., Fayolle, C., Gilbert, P., and Dacheux, N., Determination of ^{226}Ra in Mineral Drinking Waters by α Liquid Scintillation with Rejection of α-γ Emitters. *Anal. Chem.* **70**, 2353–2359 (1998).

[3] Wu, Y., Peng, J., Rutstrom, D., Koschan, M., Foster, C., and Melcher, C. L., Unraveling the Critical Role of Site Occupancy of Lithium Codopants in $Lu_2SiO_5:Ce^{3+}$ Single-Crystalline Scintillators, *ACS Appl. Mater. Interfaces* **11**, 8194–8201 (2019).

[4] Prusa, P., Kučera, M., Babin, V., Bruza, P., Parkman, T., Panek, D., Beitlerova, A., Mares, J. A., Hanus, M., Lucenicova, Z., et al., Tailoring and Optimization of LuAG:Ce Epitaxial Film Scintillation Properties by Mg Co-Doping. *Cryst. Growth Des.* **18**, 4998–5007 (2018).

[5] Sen, S., Tyagi, M., Sharma, K., Sarkar, P. S., Sarkar, S., Basak, C. B., Pitale, S., Ghosh, M., and Gadkari, S. C., Organic−Inorganic Composite Films Based on $Gd_3Ga_3Al_2O_{12}$:Ce Scintillator Nanoparticles for X-ray Imaging Applications. *ACS Appl. Mater. Interfaces* **9**, 37310–37320 (2017).

[6] G. F. Knoll, Radiation Detection and Measurement, John Wiley & Sons, New York, *4th Ed.*, 2010.

[7] Ovechkina, L., Riley, K., Miller, S., Bell, Z., and Nagarkar, V., Gadolinium loaded plastic scintillators for high efficiency neutron detection. *Phys. Proc*. **2**,161 (2009).

[8] Globus, M., and Grinyov, B., Scintillation detectors for medical and biology applications: materials, design and light collection conditions. In: Tavernier S., Gektin A., Grinyov B., Moses W.W. (eds) Radiation Detectors for Medical Applications. NATO Security through Science Series. Springer, Dordrecht (2006).

[9] Yamamoto, S., and Ishibashi, H. A., GSO depth of interaction detector for PET. *IEEE Trans. Nucl. Sci.* **45**, 1078–1082 (1998).

[10] Streun, M., Brandenburg, G., Larue, H., Saleh, H., Zimmermann, E., Ziemons, K., and Halling, H., Pulse shape discrimination of LSP and LuYAP scintillators for depth of intereaction detection in PET. *IEEE Trans. Nucl. Sci.* **50**, 344–347 (2003).

[11] Langenbrunner, J. L., Morris, C. L., and Whitton, R. M., Csl-phoswich detector for charged-particle identification. *Nucl. Instrum. Methods Phys. Res., Sect. A* **316**, 450–451 (1992).

[12] Czarnecki, S., Krol, A., Mandal, M., Poliks, M. D., Schmidtlein, C. R., Thompson, M., and Turner, J., Autonomous gamma, X-ray, and particle detector, US patent 9835737.

[13] Persyk, D. E., and Stoub, E. W., Scintillation crystal for a radiation detector, US patent 4656359.

[14] Takahashi, H., Yamaguchi, T., Okayama, M. and Kasahara, M., Comparison of the 1978 Miyagi-oki (M7.4) and 2005 Miyagi-oki (M7.2) earthquakes by strain seismograms observed at 63 Erimo, *Journal of Seismological Society of Japan* **59**, 381–384 (2007).

[15] Preziosi, E., Pani, R., Trigila, C., Polito, C., Bettiol, M., Borrazzo, C., Cinti, M. N., Fabbri, A., Pellegrinie, R., and Panig, R., A crystal identification method for monolithic phoswich detectors based on scintillation light distribution. *J. Inst.* **11**, P12009 (2006).

[16] Kurfess, J. D., Johnson, W. N., and Hulburt, E. O., NaI(Tl) - CsI(Na) Phoswich Detectors for X-Ray Astronomy. *IEEE Trans. Nucl. Sci.* **22**, 626–632 (1975).

[17] Kamae, T., Gunji, S., Hirayama, M., Kubo, H., Miyazaki, S., Saito, Y., Sekimoto, Y., Suzuki, K., Takahashi, T., Tamura, T., et al., H. Well-type phoswich counters for low-flux x-ray/gamma-ray detection. *Proc. SPIE 1734, Gamma-Ray Detectors* **1734** (1992).

[18] Mayhugh, M. R., Lucas, A. C., and Utts, B., Low Background Beta Counting with CaF_2(Eu) in a Phoswich Configuration. *IEEE Trans. Nucl. Sci.* **25***,* 569-571 (1978).

[19] Costa, E., Massaro, E., and Piro, L., 1986. A BGO-CsI(Tl) phoswich: A new detector for X- and γ-ray astronomy. *Nucl. Instrum. Methods Phys. Res., Sect. A* **243**, 572–577.

[20] Lanzanô, G., Pagano, A., Filippo, E. D., Pollacco, E., Barth,R., Berthier, B., Berthoumieux, E., Cassagnou, Y., Cavallaro, Sl., et al., Heavy ions detection by using BaF_2 crystals coupled to thin plastic scintillator", *Nucl. Instrum. Methods Phys. Res., Sect. A* **323**, 694–696 (1992).

[21] Tyagi, M., Meng, F., Koschan, M., Donnald, S. B., Rothfuss, H., and Melcher, C. L., 2013. Effect of codoping on scintillation and optical properties of a Ce-doped $Gd_3Ga_3Al_2O_{12}$:Ce scintillator. *J. Phys. D* **46**, 475302.

[22] Rawat, S., Tyagi, M., Netrakanti, P. K., Kashyap, V. K. S., Singh, A. K., Desai, D. G., Mitra, A., Kumar, G. A., and Gadkari, S. C., 2016. Pulse shape discrimination properties of $Gd_3Ga_3Al_2O_{12}$:Ce single crystal in comparison with CsI:Tl. *Nucl. Instrum. Methods Phys. Res., Sect. A* **840**, 186–191.

[23] Hennig, W., Tan, H., Warburton, W. K., and McIntyre, J. I., 2006. Single-channel beta-gamma coincidence detection of radioactive xenon using digital pulse shape analysis of phoswich detector signal. *IEEE Trans. Nucl. Sci.* **53***,* 620–624.

[24] Tyagi, M., Sarkar, P. S., Singh, A. K., Kalyani, Patel, T., Bishnoi, S., Ray, N. K., Desai, D. G., and Gadkari, S. C., 2019. Development of thermal neutron detector based on $Gd_3Ga_3Al_2O_{12}$:Ce single crystals. *IEEE Trans. Nucl. Sci.* (Accepted).

CHAPTER 7

Summary and Conclusion

This chapter presents the summary of thesis work along with the future scope.

7.1 Summary

The present thesis work involves the extensive studies on PSD and detection efficiency of GGAG:Ce scintillator. In particular, we focussed our attention on PSD ability of this scintillator for alpha particles and gamma rays using a compact digitizer. A comparison of PSD ability of GGAG:Ce with CsI:Tl was made. Their PSD characteristics for gamma rays and alpha radiations were studied by employing digitizer and zero crossover setup. GGAG:Ce,B detector showed better PSD performance as compared to the CsI:Tl crystal coupled to a PMT. FOM values for GGAG:Ce,B and CsI:Tl crystals when coupled to a PMT are 3.42 and 2.41 respectively using digitizer. ZCT of 87.06 ns was demonstrated by GGAG:Ce,B scintillator compared to 60.53 ns by CsI:Tl. When crystals were coupled to a SiPM, CsI:Tl showed FOM value of 2.8 and GGAG:Ce,B has showed 1.7. Due to the mismatching of spectral frequencies between GGAG:Ce,B scintillator and SiPM along with afterpulsing resulted in lower values of FOM.

For the application of GGAG:Ce in gamma spectroscopy, detailed realistic Monte Carlo simulations of absolute efficiencies (both total detection and photo-peak) of GGAG:Ce scintillator for gamma rays up to energy of 5 MeV and for different values of source-to-detector separation were carried out. Simulations were also made with different scintillators ($LaBr_3$:Ce, NaI:Tl, CsI:Tl, BaF_2 and SrI_2:Eu) for comparison. In order to validate these simulations, we have made experimental measurements with GGAG:Ce, CsI:Tl and BaF_2 detectors having dimensions of 18 mm × 18 mm × 10 mm, 25.4 mm ×10 mm and 30 mm × 30 mm respectively and for different values of source-to-detector separation considering ^{137}Cs source. For GGAG:Ce scintillator of dimensions 18 mm × 18 mm × 10 mm, TDE and PE are found to be (9.22±0.01)% and (3.77±0.01)% respectively. Similarly, for a cylindrical GGAG:Ce scintillator of dimensions 24 mm × 19 mm, the TDE and PE are found to be (19.79±0.01)% and (8.08±0.01)% respectively. The simulation and experimental values are in good agreement and the errors associated with them are within the data points.

The PSD capabilities were observed to depend on the presence of co-doping in GGAG:Ce scintillators. B co-doping in GGAG:Ce single crystal was found to have better PSD properties in comparison to Ca co-doped crystals while α/γ ratio indicated the maximum quenching in Ca co-doped crystals. PSD properties are highly dependent on the crystal's scintillation kinetics. In order to understand the PSD behaviour of GGAG:Ce single crystals, it is important to investigate the scintillation kinetics of these crystals. The scintillation mechanism of oxide scintillators including GGAG:Ce is dependent on their defect structure. We use a novel approach of OSL to investigate

the role of defect structure using infrared, green and blue light. The IRSL, GSL and BSL emissions confirm the presence of deeper trap centres in Ca co-doped crystals while Ce only doped crystals have more shallow traps. The OSL studies, thus, throw light on the cumulative contribution of ionization density and defect centres on the scintillation kinetics of GGAG:Ce single crystals. The opposite behaviour and large difference in decay times of alpha and gamma radiations of these crystals significantly improved the discrimination ability of the phoswich. This results in an enhanced FOM which can discriminate different radiations by more than 100% in comparison to when crystals are used individually. A high FOM of 5.9 is measured for the gamma radiation interaction in front and back crystals, thus enabling the accurate measurements of DOI useful in imaging applications. This unique combination is also equipped to detect thermal neutrons along with the charged particles and gamma rays due to the presence of Gd isotope.

7.2 Important points of thesis work

The overall thesis work can be summarized in the following important points:

- For the first time, we have reported that the behaviour of scintillation decay times of alpha particles and gamma radiations in CsI:Tl and GGAG:Ce,B scintillators were opposite to each other.
- GGAG:Ce,B coupled to PMT demonstrated a high FOM of 3.42 and zero-crossing time of 87 ns compared to 2.41 and 60 ns for CsI:Tl coupled to PMT.
- For the first time, we have carried out detailed experimental measurements and Monte Carlo simulations on absolute efficiency of GGAG:Ce scintillator for gamma rays. The results have clearly established beyond any doubt that GGAG:Ce scintillator is more efficient than $LaBr_3$:Ce, NaI:Tl, CsI:Tl, BaF_2 and SrI_2:Eu.
- Effect of co-doping on PSD ability of GGAG:Ce single crystal scintillator has been studied in detail.
- A novel approach of optically stimulated luminescence (OSL) using infrared, blue and green light has been proposed to study the presence of defect centres in GGAG:Ce scintillators.
- For the first time, we have reported measurements with a new phoswich detector consisting of a novel combination of GGAG:Ce,B and CsI:Tl single crystals, both non-hygroscopic, having very high FOM for discriminating alpha and gamma radiations.

7.3 Future scope of thesis work

- Charged particles and gamma radiations decay times trend can be tested and compared in other halide and oxide scintillators for studying the scintillation kinetics.
- Understanding the PSD performance of GGAG:Ce,B detector for lighter and heavier charged particles along with gamma rays for a wide range of energies for high energy physics experiments.
- Energy dependent efficiency studies of large volume GGAG:Ce scintillator for gamma energies up to 20 MeV.
- Extending the OSL approach to further study the scintillation kinetics in other oxide garnets such as YAG, LuAG etc having defect centres.
- Broadening the application field of GGAG:Ce to thermal neutron detection.
- To perform GEANT4 simulations of our phoswich detector design for mixed field detection.
- To test the PSD ability of GGAG:Ce,/CsI:Tl phoswich for the next generation Positron Emission Tomography material owing to its high FOM for gamma interactions.